Characterization and Simulation of the Microstructure of Additively Manufactured Hastelloy X Parts with Columnar Grain Structure

by

Ali Keshavarzkermani

A thesis
presented to the University of Waterloo
in fulfillment of
the thesis requirement for the degree of
Doctor of Philosophy
in
Mechanical and Mechatronics Engineering

Waterloo, Ontario, Canada, 2021

Examining Committee Membership

The following served on the Examining Committee for this thesis. The decision of the Examining Committee is by majority vote

External Examiner	Mohsen Mohammadi, Ph.D.
	Professor, University of New Brunswick
Supervisor	Ehsan Toyserkani, Ph.D.
	Professor, University of Waterloo
Supervisor	Norman Zhou, Ph.D.
	Professor, University of Waterloo
Internal Member	Hamid Jahed, Ph.D.
	Professor, University of Waterloo
Internal Member	Adrian Gerlich, Ph.D.
	Professor, University of Waterloo
Internal-External Member	Irene A. Goldthorpe, Ph.D.
	Associate Professor, University of Waterloo

Authors Declaration

This thesis consists of material all of which I authored or co-authored: see Statement of Contributions included in this thesis.

This is a true copy of the thesis, including any required final revisions.

I understand that my thesis may be made electronically available to the public.

Statement of Contributions

I would like to acknowledge my co-authors who contributed to the research described in this thesis:

- Prof. Ehsan Toyserkani: Supervision of the research, providing the original idea for the current thesis, editing and reviewing papers, providing experimental facilities, providing funding.
- Prof. Norman Zhou: Supervising the research work in the area of material science, metallurgy, editing and reviewing papers, providing experimental facilities.
- Dr. Ali Bonakdar: Guiding the research and providing editorial feedback in the preparation of the individual manuscripts in Chapters 3-6.
- Dr. Usman Ali: Providing editorial feedback in the preparation of the individual manuscripts in Chapters 3 and 5.
- Dr. Yahya Mahmoodkhani: Providing editorial feedback in the preparation of the individual manuscripts in Chapters 3 and 5.
- Dr. Ehsan Marzbanrad: Providing editorial feedback in the preparation of the individual manuscripts in Chapter 3.
- Dr. Hamed Asgari: Providing editorial feedback in the preparation of the individual manuscript in Chapters 6.
- Mr. Reza Esmaeilizadeh: Conducting sample preparation, performing mechanical tests, and providing editorial feedback in the preparation of the individual manuscripts in Chapters 3-6.
- Mr. Pablo D. Enrique: Conducting sample preparation, performing heat-treatment, and providing editorial feedback in the preparation of the individual manuscripts in Chapters 3-5.

Abstract

One of the well-known AM techniques is laser powder-bed fusion (LPBF), which enables engineers to benefit from the concept of "design freedom" while designing complex geometries compared to other conventional methods. This versatile powder-bed process has been used to manufacture parts with adjustable parameters such as laser power, scanning velocity, and layer thickness to be optimized to print defect-free parts. To achieve preferable part quality with no porosity, it is necessary to have consolidated layers made of single lines. Thus, an in-depth understanding of the effect of key process parameters on fast solidification is required to produce condensed layers leading to high-quality parts with low porosity and high strength. Poorly selected parameters result in creating materials with an undesirable mechanical property. In as-manufactured parts, mechanical properties are mostly governed by the formed microstructure. For example, varying grain size, phase formation, crystallographic texture, etc. can all result in changes to the mechanical responses of the material.

All AM processes are extremely expensive in comparison with the subtractive method. However, having less waste material during LPBF, as well as the opportunity to reduce the weight through topology optimization of the target geometry, make an opportunity to compete with traditional methods for expensive materials such as Ni-base superalloys, titanium alloys, and high strength steels. Among these materials, Ni-base alloys offer homologues working temperature resulting in high-temperature strength and low creep rate. Besides, alloying elements such as Cr provide good corrosion resistance even in high temperatures. One of the most important applications of Ni-base superalloy can be observed in the hot section of aircraft engines, where more than fifty percent of this specific section is made of Ni-base superalloys.

In this thesis, the microstructure formation with respect to the mechanical response of the fabricated material during rapid solidification of the LPBF process is studied. Having an estimated microstructure prior to the fabrication step is helpful in terms of saving time, money, and material compared to the tedious trial and error or statistical approach to find the required process parameters. Microstructure estimation can be achievable by utilizing a proper phase-field model which is capable of mimicking the epitaxial grain growth during the LPBF process.

A comprehensive review has been done under the topic of microstructural analysis of Ni-base superalloys from the available literature. The effect of laser power and scanning velocity on the melt pool formation has been studied independently. In addition, the effectiveness of the combined parameter of Linear Energy Density (LED) on the melt pool geometry and microstructure of Hastelloy X single tracks has been investigated. Also, a possible nucleation mechanism is discovered during the single-track study, and its significant effect on the microstructure of the melt pool is investigated. With the knowledge gained during

the single track study, a phase-field model is utilized to simulate the as-built grain structure of the Hastelloy X part. The model focuses on epitaxial grain growth and nucleation, which is observed from the previous chapter. Results reveal that the model is powerful in terms of predicting grains dimension, grains morphology, and columnar structure formation.

Based on the mentioned study, a set of process parameters (including laser power, scanning velocity, layer thickness, and hatch distances) was identified to fabricate almost defect-free parts. In the next step, different solidification patterns with the same mentioned process parameters have been utilized to control the as-built microstructure of LPBF-made parts. The mechanical response was observed to be significantly different from different microstructures in texture and morphology. The gained knowledge can be used to manufacture a functionally graded part produced by the LPBF process in the future.

Lastly, a heat-treatment study is performed on LPBFed samples. It is intended to rebuild most of the as-built microstructure to restore the original soft properties of Hastelloy X. Results show that static recrystallization is possible right after the manufacturing process (LPBF). The effect of the static recrystallization on the grain structure and mechanical response is investigated. Results reveal that the recrystallization process can alleviate the anisotropy in mechanical properties.

Acknowledgments

The realization of this research work would have not been possible without the help and support of several people, to whom I wish to express my gratitude.

First and foremost, I would like to express my deepest gratitude to my supervisors, Prof. Ehsan Toyserkani, and Prof. Norman Zhou for their guidance, caring, and patience through the completion of the work. I am grateful for their friendship and persistent help during my graduate studies at the University of Waterloo.

I hereby acknowledge my thesis examining committee members, Prof. Mohsen Mohammadi from the University of New Brunswick, Prof. Norman Zhou, Prof. Hamid Jahed, Prof. Adrian Gerlich, and Prof. Irene A. Goldthorpe from the University of Waterloo for taking the time to review my thesis and provide their valuable and constructive insights.

I thank my colleges in the Siemens project for their support and advice, Reza, Shahriar, Osezua, Francis, Pouyan, Katayoon, Ken, Dr. Ehsan Marzbanrad, Dr. Yahya Mahmoodkhani, Dr. Usman Ali, and Dr. Ali Bonakdar. It would have not been possible to finish this work without the help of my close friends Reza and Pablo.

I am also very grateful to all my colleagues at MSAM and CAMJ laboratories for their friendship and assistance.

I acknowledge the support from Jerry Ratthapakdee and Karl Rautenberg for helping with the design and printing of LPBF parts.

Furthermore, I would like to acknowledge the support of the Natural Sciences and Engineering Research Council of Canada (NSERC), the Federal Economic Development Agency for Southern Ontario (FedDev Ontario), and Siemens Canada Limited.

Finally, and most importantly, I would like to thank my mother, father, brother, and my dear wife for their endless support and encouragement.

Table of Contents

Table of figures

1 Introduction

1.1 Motivation

During the past several years, additive manufacturing (AM) of metallic parts is being considered in mainstream manufacturing due to its excellent capability of fabricating parts with complex design, which are difficult, expensive, or even impossible to fabricate with the traditional manufacturing process. Current AM technologies are powerful at making complicated geometries by depositing materials in a layer-by-layer fashion. Among all of them, Laser Powder-Bed Fusion (LPBF) is a versatile and well-developed technique in which the powder-bed process has been employed to manufacture parts. The LPBF process has been used for a variety of applications such as medical, automobiles, and aerospace applications. One of the most important advantages of utilizing the LPBF process is to have more design freedom comparing to the other AM techniques [1,2].

To reach the desired functionality from LPBF parts, the microstructural aspects of the fabricated part should be taken into consideration. Some examples of a microstructural aspect of the LPBF part include porosities, morphology and grain size, and crystallographic texture [3–6]. All the mentioned criteria can affect the mechanical response of the final product [3–6]. Therefore, it becomes essential to tune the microstructure, which is usually done by optimization of the process parameter. The microstructure of as-built parts is a result of the melting process followed by rapid solidification of the melt pool area. Melting and solidification are happening during and after laser scanning which can be affected by key process parameters. Keeping that in mind, altering process parameters can change the microstructure of the LPBF part and its corresponding mechanical and physical properties along with enhancement in the functionality of the final product [7].

As mentioned previously, the microstructure can have a profound effect on the primary functionality of the as-fabricated part. Considering that microstructure estimation prior to the fabrication step is helpful in terms of saving time, money, and material compared to the tedious trial and error or statistical approach. However, before that, a deep understanding of rapid solidification under the non-equilibrium condition is essential for microstructure formation during the LPBF process. In this regard, a systematic study is needed for key process parameters to

comprehend changes in microstructure and gain the knowledge to control it in a manner to reach the required properties.

Since metallurgical experiments are time-consuming and expensive, microstructural simulation can be useful for prediction purposes. Also, microstructural simulation can give an insight value to the formation of solidified microstructure during LPBF. For example, it is well known from laser melting processes that epitaxial growth is the most common phenomena which bring elongated grains within a single melt pool area, however, it is yet unclear that how multiple melt pool solidifications (e.g. multi-track or multi-layer deposition) contribute to form the unique LPBF microstructure. A possible solution can be real-time X-ray monitoring during the LPBF solidification which brings valuable information about grain growth but requires considerably expensive facilities followed by process condition limitations or some geometrical limitation [8]. Another feasible solution can be microstructure simulation where the microstructure formation is shown in a computational box by implementing the involved physical phenomena. However, the non-equilibrium solidification of the LPBF process makes the microstructural simulation challenging which requires so much effort to apply the actual physical phenomena to the simulation.

Theoretically, the solidification of the melt pool consists of competitive grain growth from the bottom of the melt pool boundary to the top region. Since heat conduction is strong from the bottom solidified layer, the main solidification direction will be along with the building direction. On the other hand, the anisotropic behavior of solidification of metal introduces easy growth directions that grow faster compared to other crystallographic directions. Considering the fact that each melt-pool is solidified as a polycrystalline material, the interaction between different crystals becomes difficult to predict or control during the growth process. The problem statement becomes more challenging when the fabrication of bulk metal is aimed. Compared to single melt pool solidification, the melt pools' interaction in bulk solidification (like multi-track or multi-layer deposition) results in a higher number of grains to contribute to the built-up microstructure. Also, changing the process condition (such as laser power, laser scanning velocity, and scanning strategy), which is essential for optimization purposes, can change the solidification regime and make it complicated to control the built-up microstructure. Considering the aforementioned facts,

prediction and control of the microstructure during LPBF becomes interesting and beneficial for both industrial and research purposes.

1.2 Thesis Objectives

Microstructure prediction is one of the main objectives of this Ph.D. study. To do so, a deep understanding of the LPBF solidification, which is including nucleation mechanisms, epitaxial grain growth, and columnar grain structure formation, is required to be done. The next step can be solidification simulation which makes a key contribution to microstructure prediction while it also brings value add insight into microstructure formation during the LPBF solidification. Considering all phenomena involved are non-equilibrium rapid solidification during LPBF, it is time-consuming to simulate all aspects of microstructure, grain structure simulation is the number one task for this part as it has a great impact on the mechanical strength of fabricated parts. With an in-depth understanding of microstructure formation from the mentioned objectives, it is designed to control the as-built microstructure to customize the mechanical properties. In this case, it is intended to utilize the obtained knowledge from solidification simulation to vary the grain structure and tensile properties correspondingly. Also, with potential variation in the microstructure, analyzing the anisotropic mechanical behavior is aimed to be investigated. Finally, a post-heat-treatment process is required to decrease the level of anisotropy and restore the soft properties of the material. Since static recrystallization can replace columnar grain structure with equiaxed structure, it is required to investigate the possibility of recrystallization through a direct post-heat-treatment. Besides, any obstacle during the static recrystallization should be investigated to propose some practical methods for a faster recrystallization process. Also, to show the effectiveness of the heat-treatment process, the mechanical strength of as-built parts should be compared to the heat-treated parts in different directions.

To fulfill the aforementioned tasks, the following main objectives are aimed to accomplish in this thesis:

- Investigating the effect of process conditions on the melt pool microstructure and geometry.
- Implementing the fundamental of melt pool solidification into melt pool solidification

simulation to predict the LPBF grain structure followed by a proper experimental validation.

- Customizing the LPBF grain structure by changing the process condition and characterizing the mechanical properties of LPBF parts.
- Restoring the original properties of the Hastelloy X with a proper post-heat-treatment.
- Investigating the possibilities of static recrystallization through a direct high-temperature heat-treatment and its effect on the mechanical properties of LPBF Hastelloy X.

For clarification, Figure 1 shows the graphical abstract of the thesis with key contributions in it.

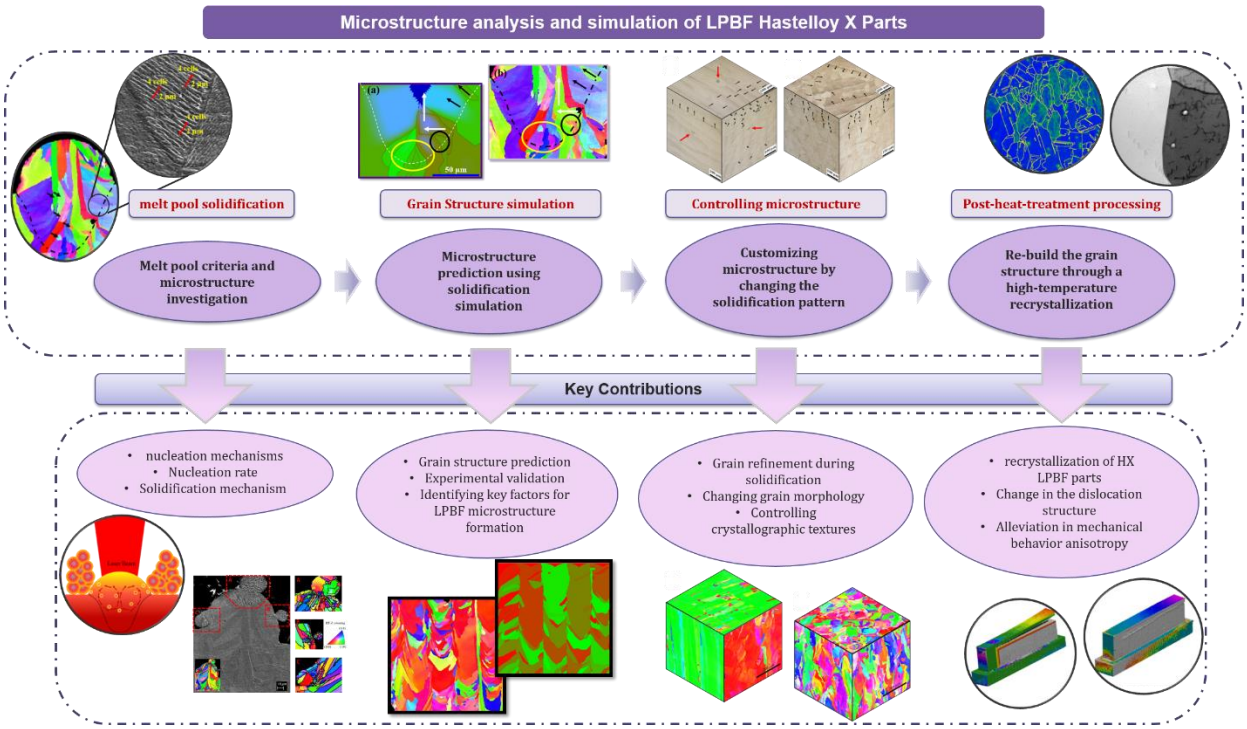

Figure 1. Thesis graphical abstract indicating interconnections between core objectives and their key contributions in the research study.

1.3 Thesis Outline

This thesis contains 7 chapters. Problem definition, motivations, thesis objective, as well as thesis outline of the current research project is discussed in chapter 1. A comprehensive literature review on the microstructure of LPBF parts and related physical phenomena is studied in Chapter 2. The effect of the main process parameters on the geometry, sub-grain structure, and grain structure of the melt pool is investigated in chapter 3. The obtained knowledge from Chapter 3 is applied to a phase-field model to simulate the grain structure during the solidification of the LPBF process (4). The simulation results are compared to the experimental results to show the accuracy of the phase-field model. The simulation results from Chapter 54 brought an insight into the solidification of LPBF microstructure, therefore, the obtained knowledge is used in Chapter 5 to control the microstructure by altering the solidification pattern during the build-up process. The effect of texture, morphology, and grain size of the microstructure on mechanical properties of tensile parts is also investigated in Chapter 5. Since Chapters 5 show a significant anisotropy in microstructure and mechanical properties, Chapter 6 focuses on the post-heat treatment of the LPBF parts to alleviate the anisotropy level by introducing grains recrystallization into the as-built columnar grain structure. Finally, conclusions and future work are discussed in Chapter 7. It should be noted that Chapters 3, 5, and 6 are adapted from published works or submitted manuscripts for publication, and Chapters 4 is ready for patent submission as follows:

Chapter 3:

- A. Keshavarzkermani, E. Marzbanrad, R. Esmaeilizadeh, Y. Mahmoodkhani, U. Ali, P.D. Enrique, N.Y. Zhou, A. Bonakdar, E. Toyserkani, An investigation into the effect of process parameters on melt pool geometry, cell spacing, and grain refinement during laser powder bed fusion, Opt. Laser Technol. 116 (2019) 83–91. doi:10.1016/j.optlastec.2019.03.012.

Chapter 4:

- A. Keshavarzkermani, A. Bonakdar, and E. Toyserkani, Solidification simulation of laser powder-bed fusion: Implementation of a phase-field model coupled to the temperature gradient. (Under review for patent publication).

Chapter 5:

- A. Keshavarzkermani, R. Esmaeilizadeh, U. Ali, P.D. Enrique, Y. Mahmoodkhani, N.Y. Zhou, A. Bonakdar, E. Toyserkani, Controlling mechanical properties of additively manufactured Hastelloy X by altering solidification pattern during laser powder-bed fusion, Mater. Sci. Eng. A. 762 (2019). doi:10.1016/j.msea.2019.138081.

Chapter 6:

- A. Keshavarzkermani, R. Esmaeilizadeh, P. D. Enrique, H. Asgari, N. Y. Zhou, A. Bonakdar, and E. Toyserkani, Static recrystallization impact on grain structure and mechanical properties of heat-treated Hastelloy X produced via laser powder-bed fusion. Submitted to the journal of Materials Characterization (under review).

2 Literature Review

2.1 Additive Manufacturing

During the past few decades, additive manufacturing (AM) of metallic parts has been paid attention, due to its excellent capability of fabricating parts with complex design, which are difficult, expensive, or even impossible to fabricate with the traditional manufacturing process. Current common AM technologies including electron beam melting, laser powder-bed fusion (LPBF), direct energy deposition, and binder jet printing are powerful in making complicated geometries by depositing materials in a layer-by-layer fashion. Additionally, the other advantages of AM processes can be mentioned as enabling united parts for intricate assembly, fast production of primary samples, less waste material, and easier manufacturing process for introducing new products to the market [9]. Among all AM processes, LPBF is a versatile and well-developed technique in which, the powder-bed process has been employed to manufacture parts. However, the goal of AM processes is not just producing parts that look good in appearance, but desired mechanical properties are also needed to be taken into consideration as it is required from the industry. To control the mechanical properties a good understanding of the corresponding microstructure of as-manufactured and post-processed parts is essential.

LPBF is a layer-by-layer AM method in which a laser applies to the spread powder. The available minimum size of geometries that can be produced with this particular method is around 40-200 μm [10]. LPBF is usually used in the manufacturing of lightweight metals, medical (specifically dental) applications, and intricate geometrical components. Under the limitation of the LPBF process, it should be noted that the process has a low build rate as the deposited material is in the shape of a single track with a size of 0.1 mm in width. In this method, hatching stripe shape always uses to both deposit new material and remelt part of the adjacent deposited material. The most important process parameters of the LPBF process are laser power (P), scanning velocity (V), layer thickness, hatch spacing, and scanning strategy. Since the applied laser beam is mainly melting the metallic material, inactive gas like nitrogen or argon flows into the compartment to reduce the amount of oxidation [1].

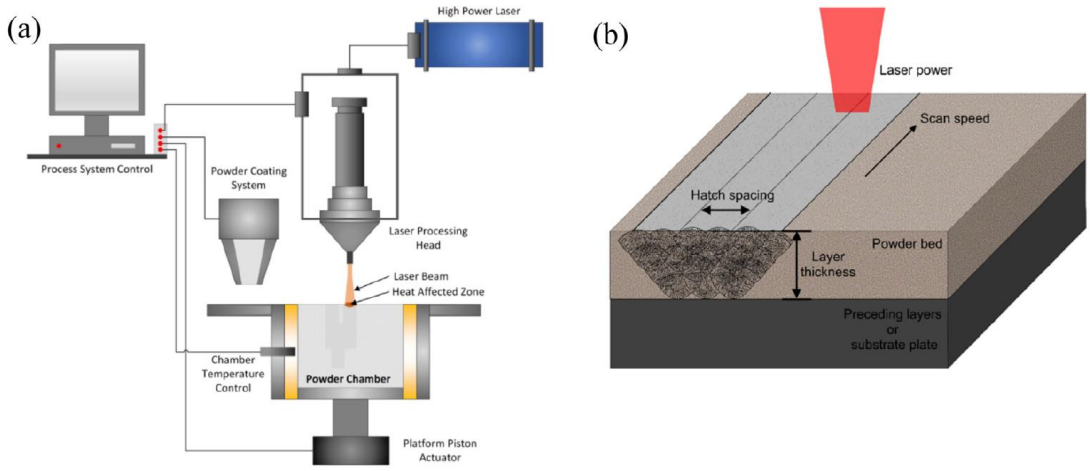

Figure 2. (a) Schematic view from selective laser melting (LPBF) process, (b) close up design for the LPBF process [1].

2.2 Nickel base superalloys

All AM processes are extremely expensive in comparison with subtractive methods. However, having less waste material during LPBF processes makes an opportunity to compete with traditional methods for expensive materials such as nickel-base superalloys, titanium alloys, and high-strength steels. Among these materials, Ni-base alloys have high homologues working temperature which makes high-temperature strength and low creep rates. In addition to this, alloying elements such as Cr will cause to have good corrosion resistance even at high temperatures. One of the most important applications of Ni-base superalloy can be observed in the hot section part of aircraft engines while more than fifty percent of this specific part is made of Ni-base superalloys [11].

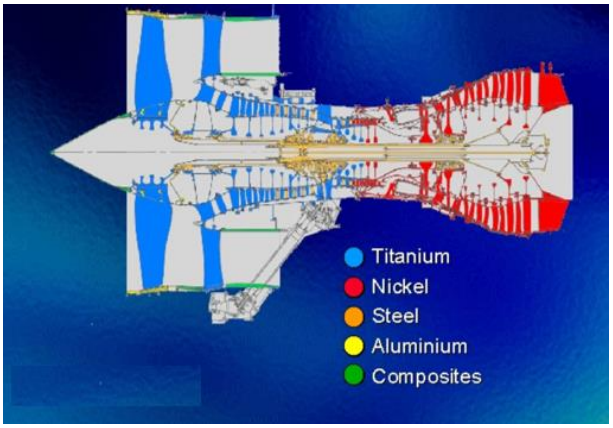

Figure 3. Schematic show of materials used in Trent 800 engine. A high portion of used material is devoted to Ni-base superalloys on the right side of the picture (turbine and combustor part) [11].

Among different nickel base superalloys, solid solution strengthened alloys (like Hastelloy X) might be a good option for the application in which a high elongation and good corrosion resistance is required. However, if it is aimed to get a high mechanical strength, precipitation hardenable alloys (like Inconel 718) will be a better option in which second phases are required to precipitate during a proper heat-treatment.

2.2.1 Physical metallurgy of Ni-base superalloy

In general, the matrix phase of nickel superalloys is γ phase, which is austenitic FCC crystal. There are also a variety of other phases in the microstructure. Gamma prime γ' (an ordered FCC phase $Ni_3(Al, Ti)$), gamma double prime γ" (BCT ordered phase Ni_3Nb), carbides (MC, $M_{23}C_6$, M_6C, M_7C_3), delta δ which is orthorhombic Ni_3Nb, as well as eta (hexagonal ordered Ni_3Ti) can control the mechanical properties of Ni-base superalloys [11–13]. In addition to that, other intermetallic phases are existing in Ni-base superalloy such as $Laves$ (Hexagonal crystal structure of $Fe_2Nb, Fe_2Ti, Fe_2Mo, Co_2Ta, or\ Co_2Ti$), sigma σ (Tetragonal crystal of $FeCr, FeCrMo, CrFeMoNi, CrCo, or\ CrNiMo$), as well as μ with rhombohedral crystal of Co_2W_6 or $(Co, Fe)_7(Mo, W)_6$ [11–13].

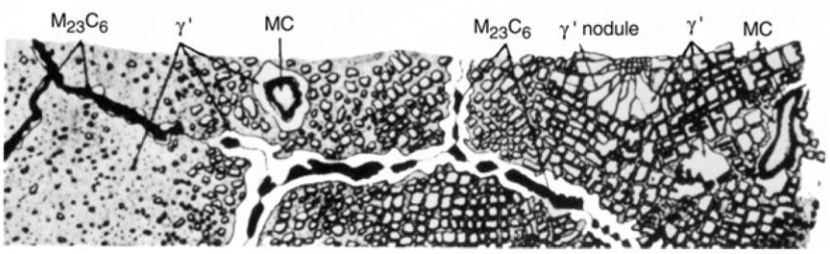

Figure 4. Schematic overview of a variety of phases existing in the microstructure of nickel-base superalloy [13].

From the mentioned phases gamma prime and double prime and eta are known as GCP (which falls into geometrically close-packed phases). Also, $\sigma, Laves, and\ \mu$ phases known as TCP (falls into topologically close-packed) phases. Mainly, GCP phases are really helpful in the case of improving the mechanical properties and TCP phases are detrimental to mechanical properties [11–13]. Gamma prime phase is a coherent phase in the gamma matrix of Ni superalloys because of very close lattice parameters in all three dimensions and form with cuboidal morphology [12]. Sometime γ" is acting as a principal strengthening phase in Ni-base superalloys such as Inconel 718. Strondl et al. [14] showed that the coarse (50-100 nm) ɣ” precipitates appear in the vicinity of ɣ phases (Ni-base FCC crystals) with the low angle boundaries. ɣ” can be distinguished from ɣ’ in the dark-field image of as it is considerably brighter than ɣ’ phase [13]. Besides, the morphology of ɣ” phase is disk-shaped because of very close lattice parameter in two directions with ɣ phase of the matrix.

Elements in Ni-base superalloys are designed to have at least one strengthening mechanism. Several strengthening mechanisms can be named such as solid solution, carbides formation at grain boundaries, and precipitation hardening. Both large and small solute atoms make distortion in the lattice structure of the matrix which makes dislocation movement harder [11–13]. There is a category of Ni superalloy in which is essentially strengthened with solid solution mechanisms such as Hastelloy X and Inconel 625 [13]. Carbides can have a limited effect directly on strength with dispersive hardening and indirectly locking grain boundaries from extreme shear [12,13]. Precipitates in Ni superalloys can imping dislocations to make dislocation movement more difficult [11,13]. If the second phase is coherent (like ɣ'), dislocation cannot cross the second phase without the formation of an anti-phase boundary (known as APB) [11]. Therefore, another dislocation is created and move in pair with the first dislocation to remove the APB and correct the order of ɣ' phase [13](Figure 5).

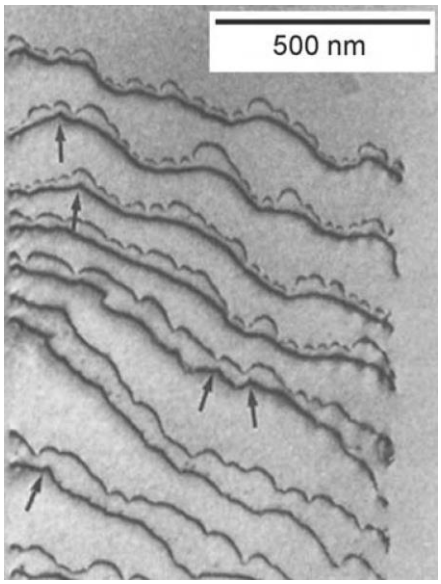

Figure 5. TEM image showing pair dislocation in Nimonic PE16 after crossing ɣ' ordered phase [11].

Hardening can be increased by changing particle size until it reaches a particular value. This is because of changing in dislocation movement mode from cutting mode to bypassing mode with different sizes and distribution of second phases [12]. Large precipitates acts a barrier for dislocation movements and it is extremely unfavorable for a dislocation to bypass them, therefore, dislocations have no choice to cut them if the input energy to the system is enough. Figure 6 showing an example of the correlation between sizes of ɣ' particle and hardness of alloy with a constant volume fraction of ɣ'. Post heat treatments usually control the distribution and particle size of second phases such as ɣ'. As a result, choosing the correct heat treatment may help to reach desirable mechanical properties.

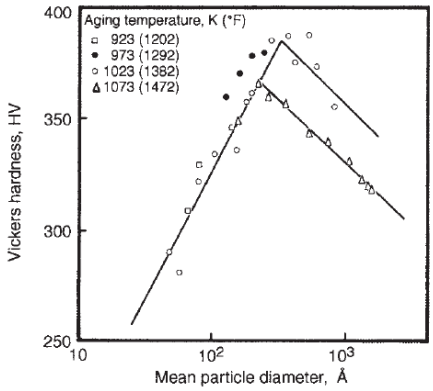

Figure 6. Vickers hardness as a function of the mean diameter of ɣ' particle in a low volume fraction of ɣ' in Ni-base superalloy [12].

2.3 The microstructure of LPBF parts

2.3.1 Solidification

Former deposited solid material on the bottom, powder metal at sides, and argon atmosphere on the top are three main phases which are surrounding molten metal during the LPBF process. Among these three phases, the highest conductivity is related to the solid phase on the bottom. As a result, the main heat flow direction would be along with the building direction of the LPBF process [15]. On the other hand, the fastest growth direction of austenitic FCC crystal of nickel is the group of <100> crystallographic direction as they make the most possible closed-pack plane during solidification (Figure 7) [15]. Based on that, the dendritic of cellular growth of crystals would be mainly along with <100> directions in which matches more with heat flow direction [16].

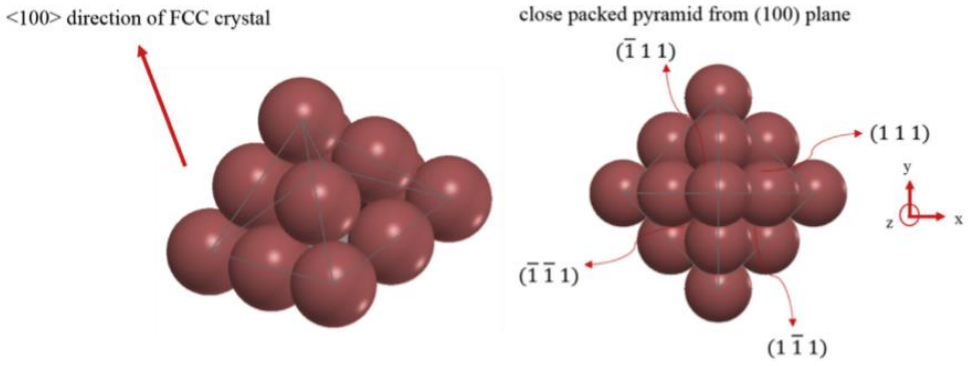

Figure 7. Pyramid which is made of [111] closed-packed planes in FCC crystal making <100> crystallographic direction during solidification [15].

Considering longitudinal cross-section at the middle of a single track, the solidification rate (R) can be simplified by $V_b.\cos(\theta)$ where V_b is the scanning velocity and θ is the corresponding angle between R and

V_b [17]. Since the scanning velocity in the case of the LPBF process is outstandingly high, the θ angle is very close to 90º to form solidification from former deposited layer to the top of melt pool (along with heat flow direction). In another experiment, Darvish *et al.* estimated the θ to be around 80º for LPBF [18]. Therefore, with a scanning velocity of 1(mm/s) the solidification rate can be estimated to 0.173 (m/s). Such fast solidification in LPBF make the solidification rate to be higher than D_i/δ where D_i is the interface diffusion and δ is interface thickness [19]. As a result, a significant solute trapping happens which leads to having a super saturated solid solution. This solute trapping may increase the lattice stress of Ni superalloy which results in strengthen material with a solid solution mechanism [19]. Cracks existing in the micrograph of as-fabricated parts are shown to be more related to residual stresses. There is no elemental segregation within the range of SEM analysis resolution (usually around 1-2 μm) found even around the cracks (Figure 8).

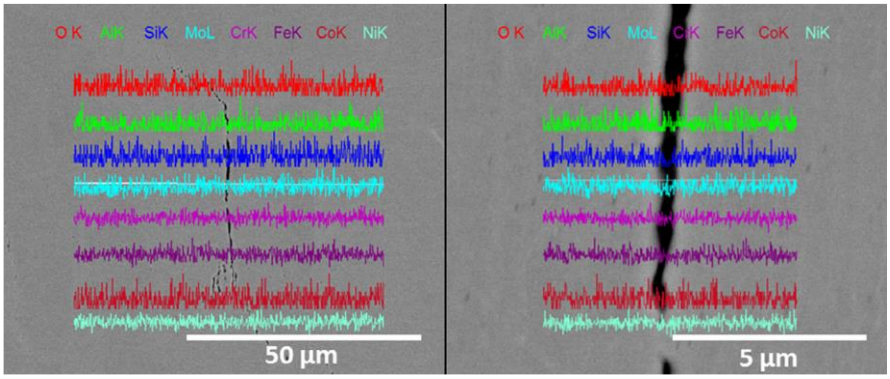

Figure 8. EDS line scanning in low and high magnification not showing any differences in the composition of Hastelloy X even around the crack [19].

2.3.2 Columnar and epitaxial growth

Epitaxial solidification is because of heterogeneous nucleation, where a nucleus or grain growth comes from the interface of solid-liquid metal [20]. The heterogeneous nucleation energy barrier is given by $\Delta G_{Het} = \frac{16\pi}{3}.\frac{\gamma_{SL}^3}{\Delta G_V^3}.S(\emptyset)$, where ΔG_V is the volumetric free energy of solid phase, γ_{SL} is the surface energy between solid and liquid phase, and $S(\emptyset)$ is a function of $\emptyset$ displayed in Figure 9. During the epitaxial growth, the function $S(\emptyset)$ tends to become zero as $\emptyset$ approaches zero as well. As a result, the energy barrier for epitaxial growth becomes very small when it is compared to casting manufacturing processes [20].

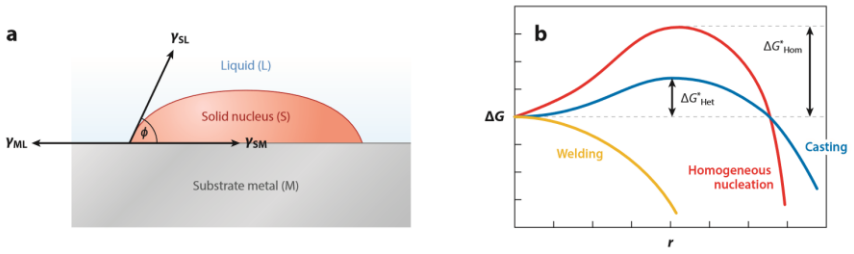

Figure 9. a) Heterogeneous nucleus at the interface of solid-liquid. b) Changing in free energy of heterogeneous nucleation in welding, casting, and homogenous nucleation [20].

Due to rapid solidification and epitaxial growth of grains, a very fine cell structure (less than a micron in diameter) has been observed in the microstructure of as LPBFed parts [21–23]. Grains can be distinguished from a different orientation of cells in the microstructure. It can be observed that grains in the newly deposited layer tend to keep their former orientation in layer-layer boundaries (grain number 1 and 2 in Figure 10. a), but change their growth directions in track-track boundaries (comparing 2 and 3 in Figure 10. a) [21].

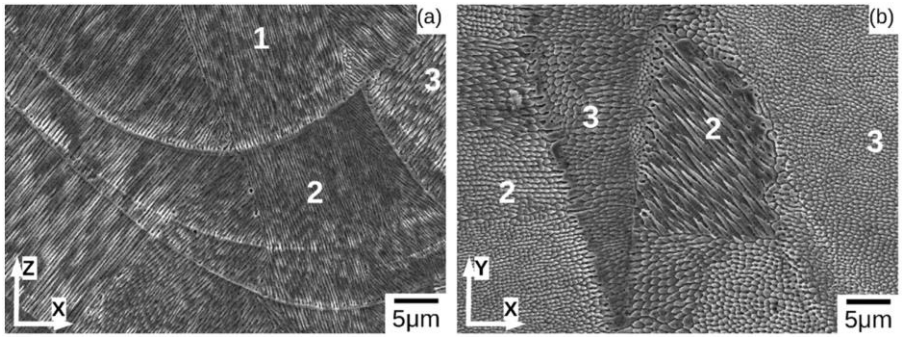

Figure 10. SEM micrograph showing a fine cellular structure in both a) longitudinal and b) perpendicular cross-sections with building direction [21].

Higher cooling rates ($\dot{T} = G \times R$) result in finer morphology of microstructure [19,24]. So many studies estimated the cooling rate of LPBF by measuring the primary spacing of cells or dendrites to be in the order of $10^5(\frac{K}{s}) - 10^6(\frac{K}{s})$ [19,24]. Due to the fact that both G and R values are substantially high during the solidification of LPBF, cells in the microstructure would be really fine correspondingly (less than 1μm). However, both temperature gradient (G) and solidification rate (R) change during the solidification of the melt pool region of LPBF. These changes may cause to have cellular or dendritic growth at the boundary of the melt pool (because of high G/R value) and equiaxed structure in the middle of molten metal as observed in laser welding processes.

Figure 11 showing the microstructure of as-LPBF in the last deposited layer on the top. Firstly, the epitaxial growth of grains seems to be either identical or perpendicular in direction with the former growth direction.

Secondly, it is shown that both at melt pool boundaries and top region of single track the cell structure exist, which means that G/R value to be all within the range of cellular growth [24].

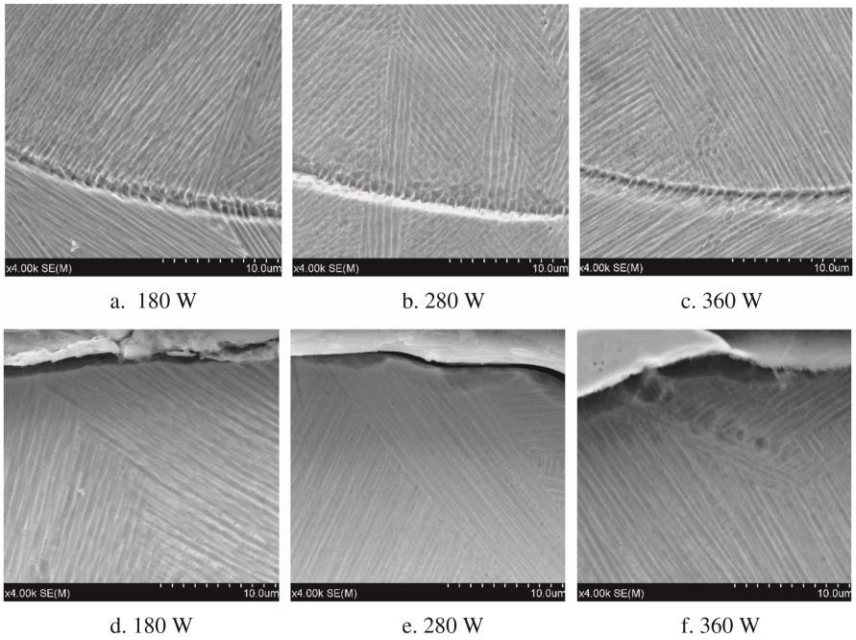

Figure 11. SEM image showing the cellular microstructure of selective laser melted parts: a), b), and c) at melt pool boundary, d), e), and f) at the top center region of tracks with different laser powers [24].

During the competitive growth of grains in solidification, the faster grains block slow grains. Since heat flow direction is along with building direction, grains with <100> crystallographic orientation which are more along with building direction will block the others. These phenomena can be observed clearly from EBSD pictures in which each grain has been assigned to color related to its crystallographic orientation.

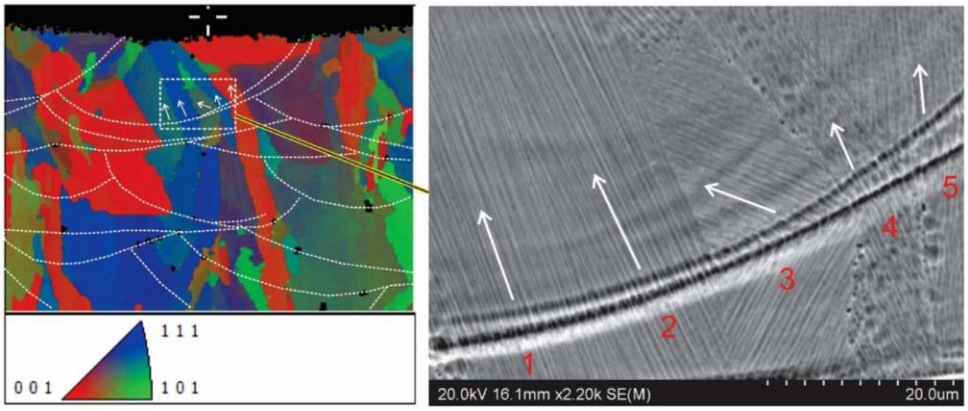

Figure 12. EBSD and Secondary image of LPBFed part displaying competitive growth of crystals with a different orientation at melt pool boundaries [24].

The microstructure of LPBFed samples is made of elongated columnar grains parallel to the building direction and crossing several melt pool boundaries [22,23]. Grain size and morphology are significantly changing with different cross-sections. In the cross-section perpendicular to building direction, it has been observed that grains are more likely to be equiaxed specifically in the re-melted area [23] (Figure 13). The morphology and distribution of grains have been observed to be consistent with the scanning path of the laser. It is claimed that re-melting can be responsible for equiaxed grains in the overlapped area of single lines and leads to having a bimodal distribution of grains (larger grains at the middle and smaller at the side of the track) [23]. Strong [100] crystallographic texture has been observed in both transverse and longitudinal cross-sections; however, the transverse cross-section seems to be more defused in texture [23]. Significant intergranular misorientation has been observed from the EBSD data of the sample [23]. The estimated misorientation from the EBSD result is up to 4°. However, for more accurate measurement, the TEM analysis can be really helpful.

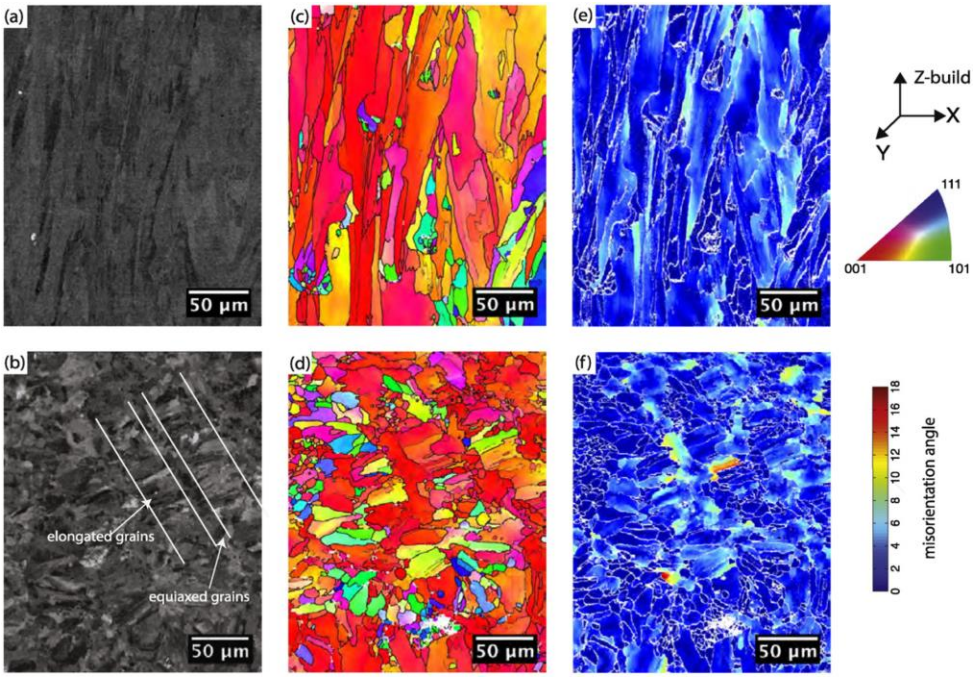

Figure 13. EBSD mapping of as LPBF sectioned along with (a), (c), and (e) longitudinal direction and (b), (d), and (f) transverse direction [23].

According to two recent studies on as-LPBF Ni-base superalloys samples, high dislocation density has been observed in the microstructure [22,23]. Two different hypotheses have been claimed for the existence of high dislocation density between cells in the microstructure. Although one of the works is criticizing the other one, the author believes both hypotheses can be true and may cause together to have such high dislocation density at subgrain boundaries (Figure 14).

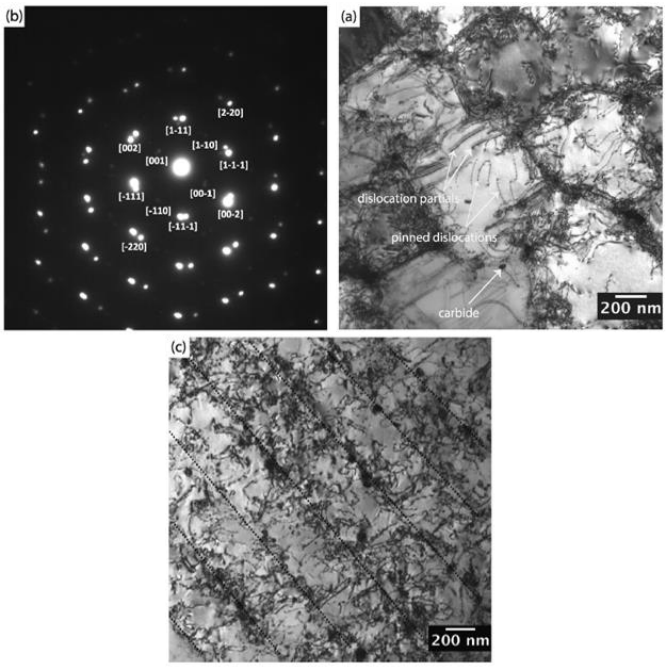

Figure 14. TEM bright-field images from (a) transverse cross-section and (c) longitudinal cross-section of the as-LPBF part showing high dislocation density at cell walls. Also, (b) displaying the SAD pattern of a selected area in transverse cross-section showing double spots related to the misorientation of cells [23].

2.3.3 High dislocation density due to misorientation

Figure 15 shows one grain in the transverse cross-section of the as-LPBF sample. The cells in the grain are assigned to different colors which represent different crystallographic orientations. More in detail, blue spots shows the gradient of orientation in the selected grain. Misorintations are more likely to be between cells instead of inside cells. This means that cells stay in the same crystallographic orientation during solidification but they may differ from each other.

Heat flow direction is mainly perpendicular to the solid-liquid interface during the solidification of the LPBF. As a result, the heat flow changes along with the solid-liquid interface [24]. On the other hand, grains tend to grow in a direction in which matches more with heat flow direction; therefore, sub-grains may slightly change in orientation to be more along with heat flow direction [23]. Besides, double spots in the SAD pattern of Figure 14 are mentioned to be representative of changes in orientation of cells, which have been measured around 7º. Misorientation between cells can be related to high dislocation density as they will represent sub-grain boundary which in this case appears as cell boundaries [23].

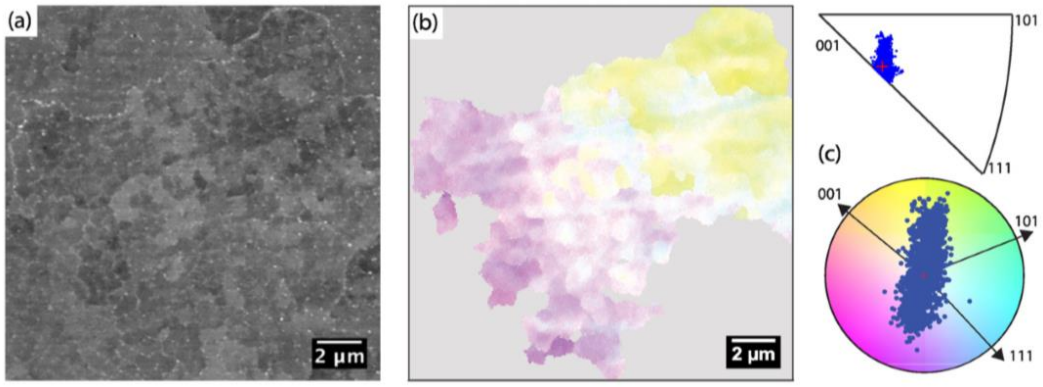

Figure 15. (a) Backscatter mode SEM image from a transverse cross-section of the as-manufactured sample showing one grain made of small cells. (b) Displaying misorientation between cells from the inverse pole-figure mapping of the grain [23].

2.3.4 High dislocation density due to the second phases

To inspect the element's segregation in size of a nanometer, STEM analysis has been equipped with an EDS detector to analyze elemental composition in high magnification. X-ray dispersive element mapping shows that Co, W, and Ni element concentrations at the boundary of cells are lower than the center of cells. On the other hand, precipitates have been observed to be enriched by Hf, Ti, Ta, and W and contain oxygen and/or carbon. It is noted that the existence of oxygen may be due to the evaporation of Al during the LPBF process, leading to reaction with W, Ti, Ta, and Hf [22]. Also, this enrichment has been mentioned to be MC carbides in which Al also has been seen to segregated to these carbides and make metastable carbides (Figure 16) [23]. It should be noted that γ' precipitate cannot be concluded only from the high concentration of Al and Ti shown by the STEM-EDX technique at cell boundaries due to the very small size of these second phases.

The existence of heavy alloying elements such as Hf and Ta can be due to their low solubility in the Ni-base matrix. Two possible phenomena can happen to have these heavy allowing elements at cell boundaries. Firstly, it can happen during the solidification in which Hf transfers mostly to the liquid phase between cells. Secondly, diffusion can happen after solidification in the solid-state. Diffusion can happen rapidly in high temperatures, therefore, the heavy element can travel to the boundary of cells as they have higher dislocation density and make it easier for both nucleate and growth at these positions.

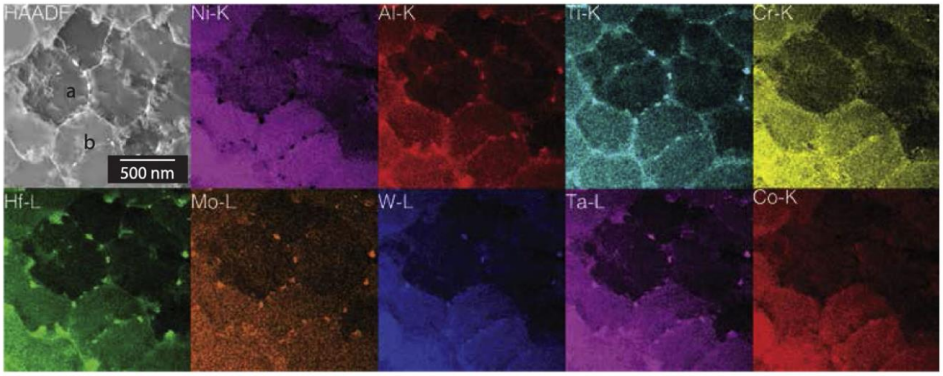

Figure 16. TEM picture of several cells with as-LPBF condition following with EDS area mapping of alloying components. Elements are identified in each picture with the corresponding concentration mapping [23].

Figure 17 shows the cell structure of an as-LPBF sample with the TEM bright field imaging technique. As it has been discussed the fine cell structure in size of 500 (nm) to 700 (nm) has been observed from TEM images as a result of the high cooling rate existing during the solidification [22]. In higher magnification, the dislocation can be observed as well as second phases (such as carbides and gamma prime) at cell boundaries [22]. To distinguish dislocation from second phases, the sample in the TEM chamber has been rotated. Besides, it has been observed that dislocations that were away from the Bragg condition disappear, while second phases at cell boundaries remain in the picture regardless of changes in the orientation of the sample [22]. Partial dislocation has been observed both in the middle of cells and at cell boundaries (Figure 17). Dislocation density at the center of cells is much lower than cell boundaries [22,23].

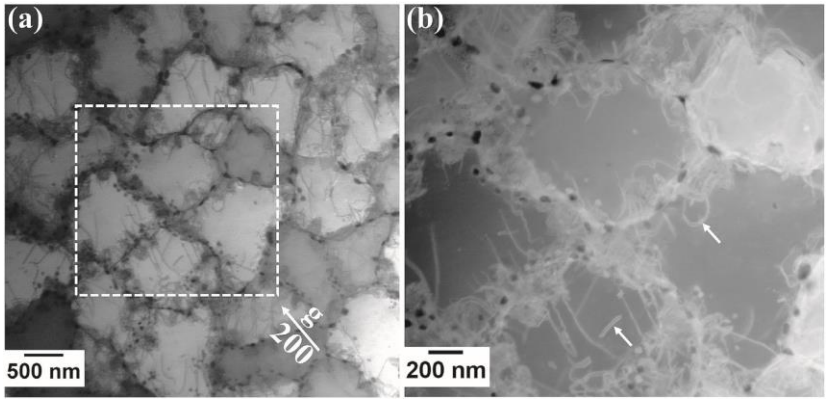

Figure 17. (a) Bright field picture of the transverse cross-section of cells. (b) Higher magnification showing dislocations in pair (marked with white arrows) [22].

Thermal gradient in the as-LPBF samples is inherent during the manufacturing process. This thermal gradient makes dissimilar thermal expansion in different locations, which leads to having residual stresses in the final product. Residual stresses can move dislocations in the microstructure. Observation of the existence of gamma prime particles and dislocation in pairs in the as-LPBF samples can be another proof

that the ordered γ' phase influences the movement of dislocation [22]. Existing dislocation move from the middle area of the cell toward cell boundaries and second phases (both precipitates and carbides) can trap this dislocation at cell walls and cause to have a high dislocation density in sub-grain boundaries [22].

2.3.5 Effect of the alloying element on the formation of phases in LPBF parts

Each nickel-base superalloy has been designed to have at least one of the strengthening mechanism. The mechanism is designed to happen with different alloying elements. In this part, the author is aiming at the effect of alloying elements on forming the second phases by comparing different Ni-base superalloys. Table 1 Shows the elements existing in three different superalloys of CM247LC [22,23], Inconel 718 [25], and Hastelloy X [21].

Table 1. Nominal composition for three Ni-base superalloys powder used for the LPBF process.

Elements	Fe	Cr	Nb	Mo	Ti	Al	Mn	Si	C	Ta	W	Hf	Co	Ni
CM247LC	-	8.11	-	0.52	0.74	5.49	-	-	0.08	3.18	9.66	1.29	9.41	Bal
IN718	19.6	19.2	5.2	3.0	0.95	0.43	0.16	0.21	0.05	-	-	-	-	Bal
HX	19.5	21.3	-	9	-	-	0.48	0.32	0.05	-	0.56	-	1.04	Bal

Figure 18. TEM Dark-field imaging showing the generation of γ' precipitates in the as-LPBF microstructure (a) bimodal distribution of γ' at cell wall and (b) higher magnification displaying finer γ' in the intracellular *region* [*23]*. shows the existence of γ'precipitates in the microstructure of as-LPBF CM247LC Ni-base superalloy. A bimodal distribution of gamma prime particles has been observed, where larger γ' precipitates up to 50 nm in size has been seen at cell walls, while intercellular γ' defined from higher magnification and resolution found up to 5 nm [22,23]. As it has been mentioned in the introduction, the formation of γ' precipitates is due to existence of Ti or Al elements. Here in the CM247LC alloy, there is a large portion of Al+Ti element in the nominal composition of alloy which leads to having γ' precipitates even in the as-LPBF fabricated part.

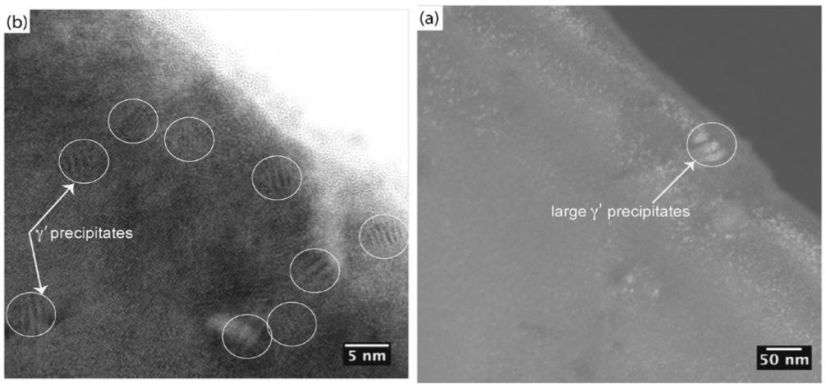

Figure 18. TEM Dark-field imaging showing the generation of γ′ precipitates in the as-LPBF microstructure (a) bimodal distribution of γ′ at cell wall and (b) higher magnification displaying finer γ′ in the intracellular region [23].

Comparing with CM247LC, there is a big difference in the microstructure of as-LPBF Inconel 718 in which second phases such as carbides and laves phases have been observed in the microstructure [25,26] TEM imaging has been performed to investigate the microstructure of as-LPBF Inconel 718 in very high magnification (Figure 19). Because of very fine particles observed in the microstructure, nanobeam diffraction patterns have been taken to identify the crystal structure of these dark particles in TEM bright-field images. The result of indexed diffraction patterns reveals that the crystal structure of these particles is very similar to Laves with HCP crystal structure [25]. In addition to that, EDS analysis from base metal and Lave phases showing a much higher concentration in the Nb element where the Laves phase existing [25]. It is worth mentioning that a high concentration of Nb element in Inconel 718 leads to having Laves phases, which mainly consist of $(Ni, Cr, Fe)_2(Nb, Mo, Ti)$. In addition to the Laves phase, small cubic shape carbides in a size of 10 nm have been observed to exist at inter-cellular regions [25,26].

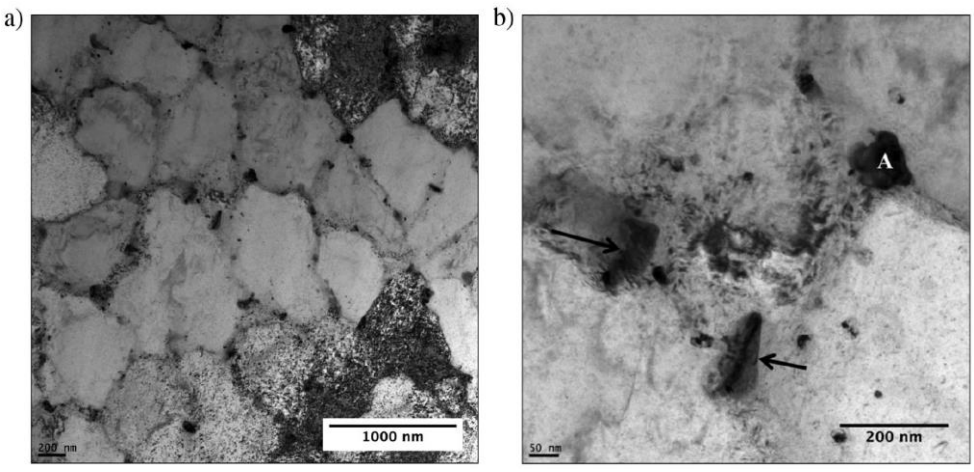

Figure 19. (a) TEM image from the microstructure of as-LPBF Inconel 718 demonstrates segregated area at cell boundaries (b) Higher magnification showing Laves phase (marked with arrows) at cell walls [25].

Hastelloy X is designed to strengthen with a solid solution mechanism where alloying elements are limited to Mo, Cr, Fe, and Co, which all can be a solution in the gamma austenitic matrix (Table 1). That's the main reason that just a few second phases were observed in the microstructure of as-LPBF Hastelloy X [21]. It is mentioned that $M_{23}C_6$ enriched by Cr and M_6C enriched by Mo has been observed at cell boundaries [21]. In addition to that because of residual stresses which commonly happens during thermal cycles with a fast cooling rate at the HAZ area and melt pool region, high dislocation density has been observed at cell walls of Hastelloy X [21].

2.3.6 Microstructural evolution during heat treatment

Heat treatments are usually helpful in terms of reduction in dislocation density and mechanical properties enhancement of parts. Residual stresses in the as-fabricated parts can lead to having cracks' initiation and propagation which are detrimental to mechanical properties. In addition to that, residual stresses can distort the part after removing them from the base plate. Furthermore, it is mentioned that various amount of residual stresses accumulated in a different location makes anisotropy in mechanical properties [26]. Table 2 shows changes in residual stresses in three different heat treatment post-processes compared to as-fabricated condition. It is observed that homogenization can almost remove the residual stresses in the part [26].

Table 2. Residual stress percentage after three different heat treatment[26].

	Direct Ageing	**Solution**	**Homogenization**
$\boldsymbol{\sigma^{Rs}/\sigma_0^{Rs}}$	0.985	0.217	0

With the help of the EBSD technique, it has been observed that partial recrystallization occurs during heat-treatment (HT) at 980ºC for 2 hours [25]. Also, it is mentioned that the columnar structure of grains is still existing in the microstructure after heat treatment with the strong crystallographic texture of <100> along with building direction (Figure 20). It is claimed that this strong texture corresponds to the epitaxial grains which remained in the microstructure and did not recrystallize after HT [21,25]. Comparing to the as-LPBF condition, it has been observed that texture in the heat-treated sample is more defused because recrystallization happened with more random grain orientation nucleation [25].

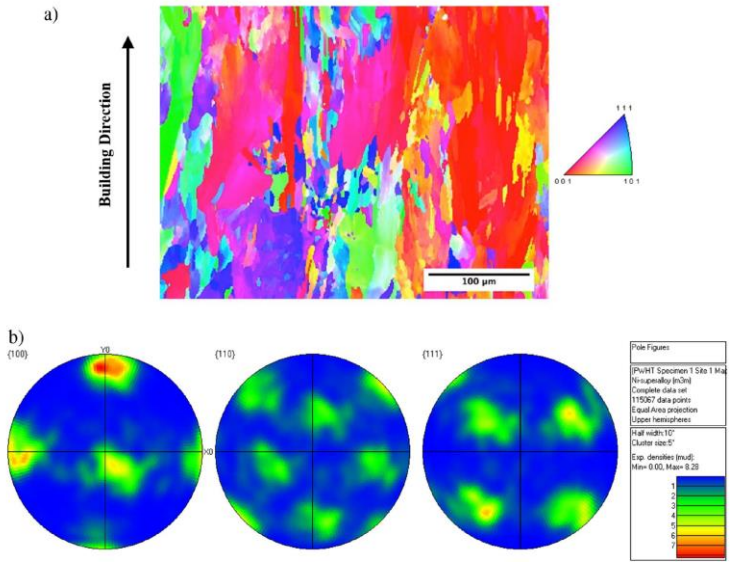

Figure 20. (a) EBSD inverse pole-figure mapping showing columnar grain after heat treatment (b) pole figure of the selected region [25].

Four different steps for heat treatment is taken to consideration as it has been shown in Table 3 in which WC, FC, and AC means water, furnace, and air cooling correspondingly.

Table 3. Heat treatments with their time and temperature in each process[26].

Designation	Homogenization	Solution	Ageing
AS	None	None	None
DA	None	None	720°C/8h/FC at 50°C/h to 620°C+ 620°C/8h/AC
SA	None	980°C/1h/WC	720°C/8h/FC at 50°C/h to 620°C+ 620°C/8h/AC
HA	1080°C/1h/WC	None	720°C/8h/FC at 50°C/h to 620°C+ 620°C/8h/AC
HAS	1080°C/1h/WC	980°C/1h/WC	720°C/8h/FC at 50°C/h to 620°C+ 620°C/8h/AC

Figure 21 shows the microstructure achieved after four different heat treatments mentioned above. Results shows after direct aging (8 hours at 720ºC) melt pool boundaries and cellular solidified structure still exists in the microstructure very similar to the as-LPBF condition [26]. This mainly happens because the aging temperature is low to homogenize or dissolve second phases such as Laves phases created due to segregation happening during solidification. However, after Solution Aging (SA) cellular structure and melt pool boundaries have been disappeared in the microstructure, where Laves phases partially dissolved and needle-like delta phases (in size of a micron) precipitate both at intragranular and intergranular positions [26]. On the other hand, homogenization aging is happening at 1080ºC, which is higher than the solvus temperature of the delta phase and as a result HA, samples no delta phase has been observed and second phases mainly contain carbides at grain boundaries [26]. HSA sample contains a significant portion of the delta phase at grain boundaries comparing to the SA sample (Figure 21 d and h). This is mainly due to the

complete dissolution of the Laves phases after homogenization and as a result, more delta phases formed from the existing Nb element [26].

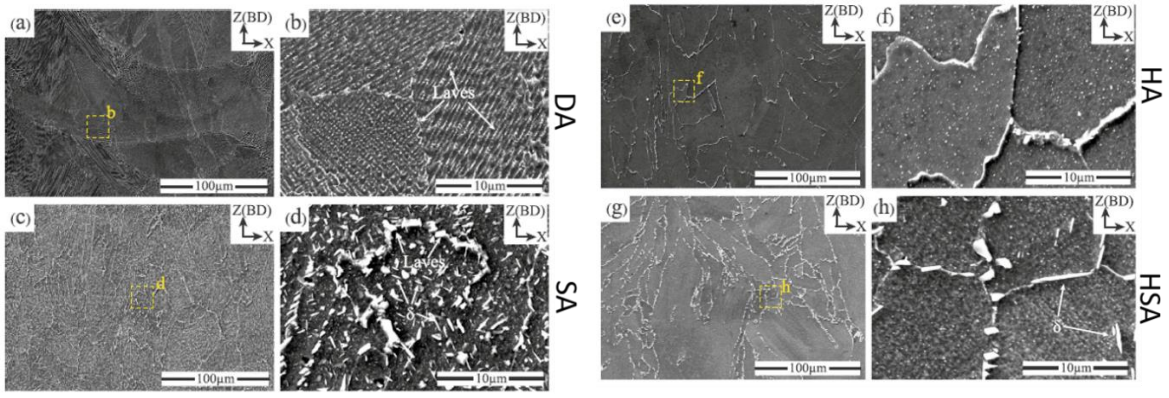

Figure 21. SEM micrographs from longitudinal cross-section of Inconel 718 after (a) DA, (c) SA, (e) HA, (g) HAS, and (b), (d), (f), (h) are magnified area displayed in (a), (c), (e), and (g) [26].

Figure 22 shows the TEM image of dark-field mode from γ' precipitates at microstructure of CM247LC after heat treatment and recrystallization. Bimodal distribution of cuboidal γ' precipitates in size of 200-400 nm with finer γ' precipitates which maybe remained from as-fabricated condition [23]. In addition to γ' phased, very fine carbides observed and identified both from micrograph and X-ray data [23]. Comparing to Inconel 718, γ' precipitates exist instead of delta phases in the microstructure of heat-treated CM247LC because of higher concentration Al element (which is γ' former) and absence of Nb element (which is delta former) in the composition.

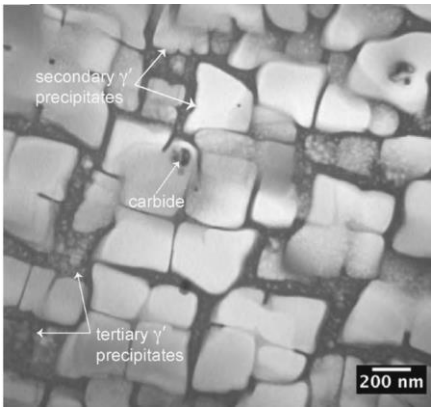

Figure 22. TEM dark-field micrograph of heat-treated as-LPBF CM247LC sample displaying the bimodal distribution of γ' depicted from recrystallized region [23].

There is a big difference in the microstructure of Hastelloy X (HX) compare to precipitation-hardenable Ni-base superalloys (such as CM247 or Inconel 718). After heat treating at 1080 ºC for 2hr changes in microstructure are limited to dislocation density and carbides distribution. Heat-treated HX contains lower dislocation density and more distributed carbides in comparison with the as-LPBF condition [21]. On the

other hand, results reveal that carbides distribution is different in HIP samples in comparison with HIP+HT samples. It has been observed that more carbides formed at grain boundaries in HIP samples while the HIP+HT sample contains distributed carbides without significant concentration at grain boundaries (Figure 23). This is happening because HIP samples cooled in the furnace with a slower cooling rate and as a result, more time for Mo to diffuse and create continuous carbides at grain boundaries [21].

It is observed that the most effective parameters during the heat-treatment would be time and the temperature of heat-treatment. Particularly for Hastelloy X, since solid solution is designed to be the only strengthening mechanism, the temperature is recommended to be around the solutionizing temperature (1177˚C) for the heat-treatment followed by water quenching to avoid formation of carbides in the microstructure.

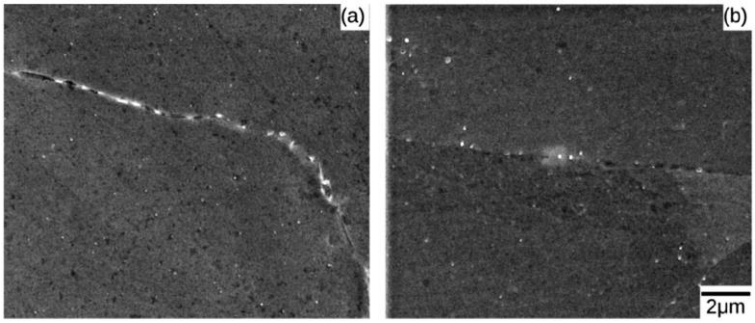

Figure 23. SE mode of SEM image showing more concentration of carbides at grain boundaries in (a) HIP samples in comparison to the (b) HIP+HT sample [21].

2.4 Mechanical behavior of LPBF parts

Figure 24 demonstrating the result of tensile testing of three as-LPBF parts compared to conventionally cast and LPBF+HIP samples. As it has been observed, the ultimate tensile strength (UTS) of as-fabricated CM247LC samples are very similar to the cast and LPBF+HIP samples [23]. On the other hand, the fracture strain of as-LPBF samples is much lower than cast and HIP samples [23]. As it has been discussed in the Heat treatment section, CM247LC is designed to be strengthened with second phases of γ' after post heat treatment. Therefore, the material has been strengthened after heat treatment in cast+HT and LPBF+HIP with precipitation hardening. On the other hand, as-LPBF samples have high dislocation density, fine cellular structure, and super-saturated solid solution in the structure which leads to having again high yield and ultimate strength same as heat-treated samples [23]. It is worth mentioning that residual stresses in the microstructure cause to have both intergranular and intragranular cracks in the microstructure, which are detrimental for mechanical properties. These cracks lead to having lower ductility in as-LPBF parts in

comparison with HIP samples in which defects such as pores and cracks will be mostly removed from microstructure [23].

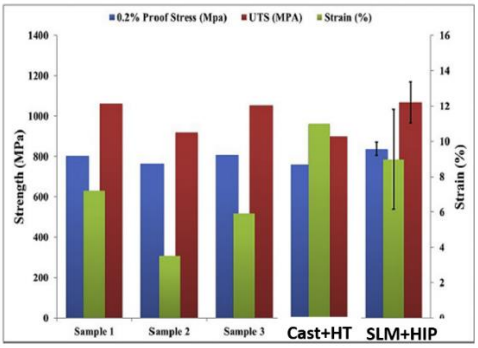

Figure 24. Bar graph demonstrating proof stress, UTS, and fracture strain of three LPBFed, conventionally cast+HT, and LPBF+HIP+HT CM247LC tensile samples [23].

Figure 25 shows the result of yield strength (YS) and fracture elongation of two different Ni-base superalloys of Hastelloy X and Inconel 718 in as-LPBF and heat-treated conditions. Results for Hastelloy X shows that heat treatment mainly the total elongation and decreasing the YS [21]. In contrast to HX results, heat treatment after selective laser melting of Inconel 718 will decrease the total elongation and increase the proof strength of the material (Figure 25) [26].

Hastelloy X is designed to be strengthened with a solution hardening mechanism where microstructure results showed that the solution element has been distributed well in the microstructure of the as-LPBF condition. However, higher strength in as-LPBF samples is due to the fine structure and high dislocation densities which are removed after heat treatment post-processing and reduce the YS and increase total elongation [21]. On the other hand, heat treatment after fabrication of Inconel 718 makes needles like δ precipitates which are in coherent with austenitic γ matrix. The formation of δ phase after heat treatment leads to have lower ductility and higher yield strength due to the fact that δ will make dislocation movements harder [26]. As a result, heat-treated Inconel 718 has higher YS and less ductility in comparison with as-built conditions.

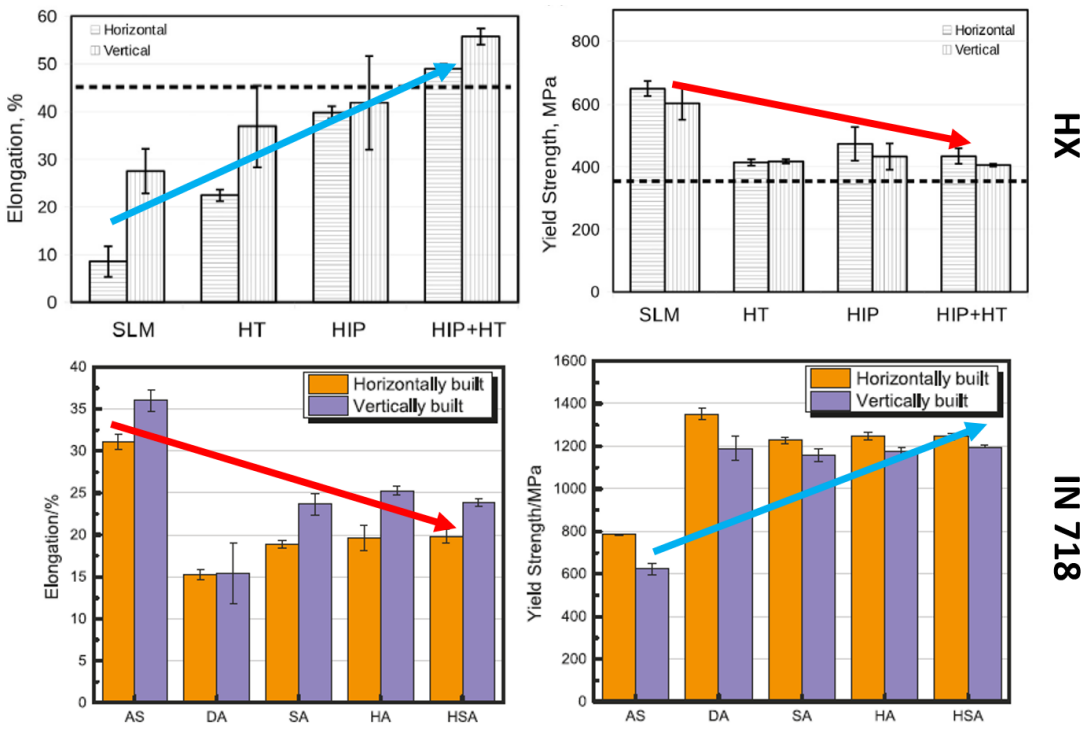

Figure 25. Bar plot for tensile tests for Hastelloy X [21] *and Inconel 718* [26] *for horizontally and vertically built samples.*

Figure 26 shows the microstructure of as-built and deformed Inconel 718 samples after tensile testing. It can be observed that a much higher dislocation density has been created at the cell walls (Figure 26 (a)). It is also shown in Figure 26 (b) that Laves phases can impede dislocation movement (shown by black arrows). As-fabricated Inconel 718 has mostly Laves phases at cell walls and has any other second phases in the intercellular region. As a result, during the deformation, dislocations freely move in the intercellular region and block intracellular areas and become higher in density [27]. Increased tangled dislocation is mainly due to the possibility of so many cross slips that can provide high dislocation density at subgrain boundaries [27].

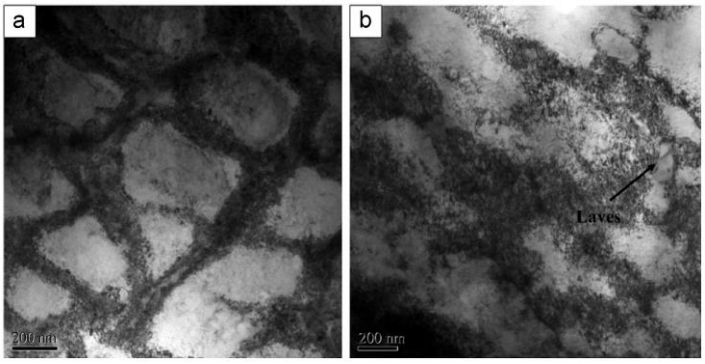

Figure 26. TEM image of as-LPBF Inconel 718 after tensile testing showing (a) dislocation structure at cell walls and (b) impeded dislocations with Laves phases during deformation [27].

Figure 27 shows the microstructure of LPBFed and solution aged (SA) Inconel 718 sample after deformation. Seconded phases which are mostly δ phases displayed to be distributed randomly after heat treatment in the microstructure [27]. It can be observed that dislocation has been blocked with δ phases placed in their path. Comparing with as-LPBF sample, dislocation density in solution aged sample after deformation is higher, due to the existence of second phases (such as γ', γ", and δ phases) which has been created after heat treatment [27]. Distributed second phases make the dislocation motion more difficult, and as a result, the dislocation density in the SA sample becomes higher in comparison to the as-fabricated sample [27]. By increasing in dislocation density, there is going to be more piled up dislocations, therefore dislocation movement becomes harder and the driving force for deformation get enhance till finally sample cut through the incoherent second phases like δ.

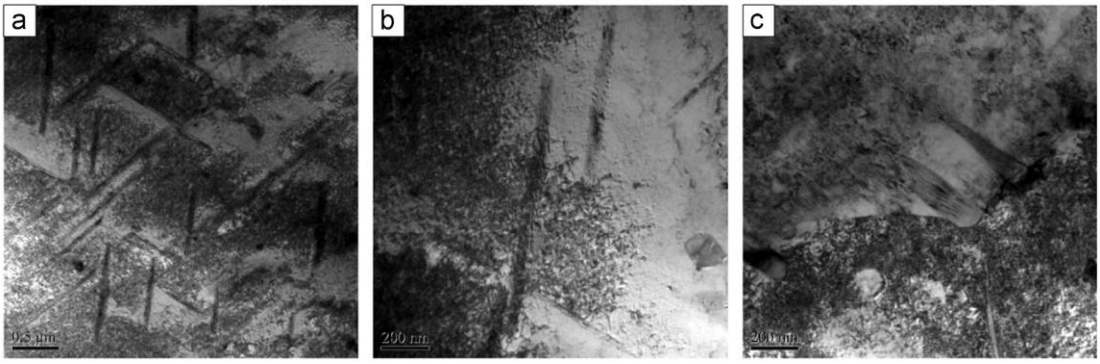

Figure 27. TEM micrograph of solution aged sample after fracturing at tensile test (a) at low magnification, (b) high magnification, (c) at grain boundaries showing the microstructure [27].

It has been also observed that the homogenized solution aged (HSA) samples have slightly more ductility in comparison to the SA sample [27]. As it has been observed in the microstructure of SA Inconel 718, after SA treatment Laves phases still existing at grain boundaries. Homogenization before solution aged will completely dissolve Laves phases and make a better Nb distribution in the matrix. Thus, homogenization before SA causes to have less incoherent δ phases in the microstructure and as a result, have better ductility compared to SA treatment.

2.5 Summary

Investigation on microstructure and mechanical properties of as-fabricated and post-heat-treated Ni-base superalloys suggesting the following findings based on the discussions in the literature:

- SEM micrographs of the cross-section of LPBFed parts reveal that G/R criteria remain high enough during the solidification of LPBF to have a cellular structure in the entire microstructure of LPBF parts.

- The high dislocation density in the subgrain boundaries can be due to misorientation of cells and the existence of very fine second phases at cell walls which leads to blocking dislocations movement.
- High dislocation density and solid solution atoms in the as-build samples strengthens the material.
- Residual stresses in the part can cause both anisotropic mechanical properties and cracks in the microstructure. Appropriate post-heat-treatments can relieve these kinds of residual stresses by the annihilation of dislocation and recrystallization in the microstructure.
- In solid solution Ni-base superalloys, dislocation annihilation reduces strength and increase ductility after post-heat-treatments.
- In precipitation hardening alloys, the formation of second phases compensate for the dislocation annihilation. In most cases, ductility has been decreased after post heat treatment because of the formation of incoherent δ phase in Inconel 718.
- Because there are many factors involved in the microstructure formation of LPBF parts that are influenced by changes in process conditions, it is difficult to predict the microstructure but essential to do in order to control and tune it based on desirable material performance.
- Due to the rapid solidification of LPBF, the anisotropic growth behavior of crystal growth is exaggerated which results in anisotropic mechanical behavior and becomes difficult to alleviate during post-heat-treatment techniques. Therefore, the recrystallization of as-built microstructure becomes an interesting topic to investigate for further studies.

3 An investigation into the effect of process parameters on melt pool geometry, cell spacing, and grain refinement during laser powder bed fusion

3.1 Introduction

Additive manufacturing (AM) of metallic parts has grown in popularity due to its ability to fabricate parts with complex designs [28]. Laser powder-bed fusion (LPBF) is one of several AM techniques that builds parts in a layer by layer fashion. This versatile powder bed process has been used to manufacture parts with adjustable parameters such as laser power, scanning velocity, and layer thickness that can be optimized to print defect-free parts. To achieve acceptable part quality with no porosity, it is necessary to have consolidated layers made of single lines. Thus, an in-depth understanding of the effect of process parameters

on a single track melt pool and the subsequent fast solidification is required to produce condensed layers leading to high-quality parts with low porosity and high strength.

Among all LPBF process parameters, energy input density has been considered as one of the most significant variables [29,30]. The energy input can be written as a function of laser power, scanning velocity, layer thickness, hatching distance, and other variables [28,31,32]. However, based on the works in literature [5,33,34], laser power and scanning velocity are considered as the most effective parameters. Some aspects of the single track formation (such as melt pool and bead geometry) under different sets of process parameters (laser power, scanning velocity, layer thickness, and hatching distance) have been studied for a few materials [29,30,35–37]. The laser energy density (LED) is one of the proposed energy input density functions and is defined as the ratio of laser power to a scanning velocity $\frac{P}{V}(\frac{J}{mm})$ [38]. LED has been used to find the process window for deposition of different materials in the LPBF process [29,33]. In addition, LED has also been utilized to avoid balling, irregular and discontinuous track shapes in LPBF [35,38]. It has also been observed that incomplete melting can be the result of a low LED deposition, while a high LED deposition may introduce keyhole pores, which are detrimental for additively manufactured parts [36].

Interaction of powder particles with laser irradiation during LPBF results in melting and solidification of molten metal. Parallel to melting, understanding the solidification of melted particles and microstructure formation in the melt pool is essential to reach the desired mechanical properties. Since the process parameters directly affect the geometry of the melt pool, changes in microstructure are expected to occur with different process parameters. Several studies have been conducted to evaluate the influence of process parameters on the microstructure of LPBF parts [15,29,39–41]. Singletrack deposition of Inconel 718 showed that the beads produced with low LED result in columnar grains growing upwards, while high LED values lead to grains converging at the center of the bead [15,40]. These long columnar grains observed in the microstructure of LPBF parts highlight the re-melting of previous layers resulting in the continuation of the crystallographic grain growth from grains in the former layers [29,39]. Also, it was reported that the formation of slender columnar grains may be due to the high cooling rate during the LPBF process with different process parameter conditions [41].

In this study, the effect of laser power, scanning velocity, and LED value on the melt pool geometry and corresponding microstructure are investigated for Hastelloy X single tracks printed using an LPBF system. As discussed previously, LED values have been used as a guideline for printing effective LPBF parts. However, it has not been evaluated if the LED criterion is valid for different materials at different LED values. Also, it is important to study the differences, if any, between the observed melt pool geometry and

solidified microstructure at fixed LED values to evaluate the use of LED as a guideline for printing LPBF parts. To conduct this research, a series of single-track depositions of Hastelloy X were performed to study the effect of changes in the laser power and scanning velocity with fixed LED values on the geometry and microstructure of the melt pool. Results reveal that for a fixed LED, laser power has a higher influence on the melt pool dimensions (width and depth) while an increase in laser power has a higher effect on the melt pool depth. A finer cell structure is observed in the melt pool of high laser power and is thought to be due to the higher cooling rates observed at higher laser power. Finally, it is proposed that the grain detachment caused by the increase in the number of partially melted particles (PMP) is the mechanism for the higher number of new grains observed in melt pools created with higher laser power.

3.2 Materials and methods

Hastelloy X gas-atomized powder supplied by EOS GmbH, with the chemical composition listed in Table 4 was used to fabricate the LPBF parts with a $D_{10,}$ $D_{50,}$ and D_{90} of 46.4 µm, 30 µm, and 15.5 µm respectively. As shown in Figure 28, powder particles are mostly spherical with attached satellite particles.

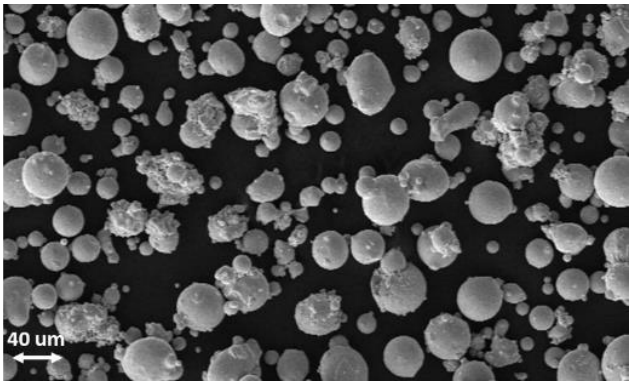

Figure 28. SEM image of powder metal showing the spherical morphology of particles with attached satellites.

Table 4. Nominal composition (in wt.%) of Hastelloy X gas-atomized powder used for selective laser melting process [42].

Ti	Al	Cu	Mn	Si	C	Co	W	Mo	Fe	Cr	Ni
<0.15	<0.5	<0.5	<1	<1	<0.1	1.5 ± 1	0.6 ± 0.4	9 ± 1	18.5 ± 1.5	21.75 ± 1.25	balance

The experimental study was designed to manufacture12 rectangular substrates of Hastelloy X with base dimensions of 25 mm × 17.5 mm × 5 mm. Six single laser scans were applied on top of the 3D printed substrates to form single tracks of length 25 mm. Single tracks with varying laser scanning velocity and power were printed on different substrates while single tracks with the same laser scanning velocity and power but different nominal layer thickness were printed on the same substrate. The 20, 40, and 60 µm single tracks were printed with a base nominal layer thickness of 20 µm where the laser irradiation was

skipped for 1 and 2 layers for the 40 and 60 µm, single tracks. Every single track, with its respective dimensions, was printed twice adjacent to each other (Figure 29) and parallel to the direction of the recoater movement.

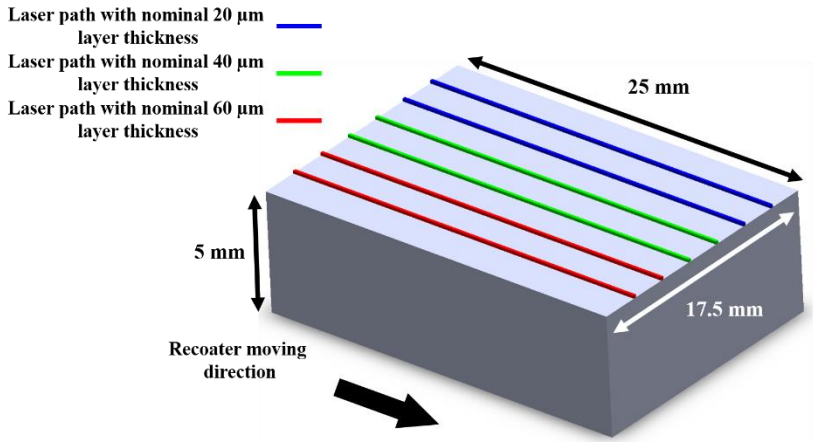

Figure 29. Printed substrate and location of the laser path on top of the substrate to manufacture single tracks.

EOS M290, equipped with a Ytterbium fiber laser, was used for fabricating the substrates and single tracks. As the laser spot size is considered to be a major contributing parameter to melt pool formation [43,44], it is important to mention the effective laser spot size of 80 µm was utilized in this experiment. All substrates were designed with the same process parameters as default EOS Hastelloy X parameters. Printed substrates were double scanned on the last layer to get a smooth surface. After reviewing the process parameters used in available literature for Hastelloy X [45–48], a specific range of laser power and scanning velocity was selected in this study. Three values of LED were chosen for single tracks at different laser powers and scanning velocities, as listed in Table 5. Design of experiments for single-line tracks consisted of varying laser powers (from 150 W to 300 W) and scanning speeds (from 600 mm/s to 2000mm/s). The laser power and velocity were selected based on different LED values as shown in the 1st column of Table 5. The completed specimens were cross-sectioned (4 repetitions at 2.5 mm offsets from the ends of the substrate) using a Struers Accutom-50 precision cutter for a total of 4 cross-sections per single track condition.

Table 5. Set of 12 groups of single tracks showing existing laser powers (P) and scanning velocity (V) for deposited tracks.

LED (J/mm)	P=150 W	P=200 W	P=250 W	P=300 W
0.25±0.0 (J/mm)	V = 600 mm/s	V = 800 mm/s	V = 1000 mm/s	V = 1200 mm/s
0.20±0.01 (J/mm)	V = 700 mm/s	V = 1000 mm/s	V = 1200 mm/s	V = 1500 mm/s
0.15±0.006 (J/mm)	V = 1000 mm/s	V = 1300 mm/s	V = 1600 mm/s	V = 2000 mm/s

The samples were manually polished using progressively finer SiC grinding papers from 320 to 4000 grit sizes. Finally, the samples were polished with 1, 0.1, and 0.05 µm alumina slurry and rinsed with ethanol to remove residual alumina from the surface of the samples. Polished samples were kept in Glyceregia [49] ($HCl\ 50ml - HNO3\ 10ml - Glycerol\ 10ml$) solution for about one minute for etching. The melt pool observation of cross-sectioned parts was performed using a Keyence VK-X250 confocal laser microscope. A Zeiss ULTRA SEM equipped with an EDS detector was used to study the microstructure and chemical composition of deposited single tracks. Electron backscattering diffraction (EBSD) analysis was performed using a JEOL7000F SEM equipped with an Oxford EBSD detector to investigate the grain structure of the fabricated single tracks with different process parameters. Data collection during the EBSD analysis was performed using AZtecHKL and post-processing for data analysis was performed with HKL Channel 5.

3.3 Results and discussion

As mentioned previously, single tracks of Hastelloy X on the LPBF-made substrate were produced in the laser power range from 150 to 300 W with scanning velocities from 600 to 2000 mm/s and layer thickness from 20 to 60 µm. Figure 30(a) and 3(b) show the depth and width of the melt pool region as a function of laser power in which the red, green, and blue colors represent LED values of 0.25 J/mm, 0.20 J/mm, and 0.15 J/mm, respectively. Similarly, triangular, circular, and rectangular markers represent a layer thickness of 20 µm, 40 µm, and 60 µm, respectively. Figure 30(a) and 3(b) demonstrate that the width of the melt pool is increasing from $93 \pm 9\ \mu m$ to $121 \pm 8\ \mu m$ and depth of the melt pool is increasing from $41.8 \pm 6\ \mu m$ to $94 \pm 9\ \mu m$ while the LED increased from 0.15 J/mm to 0.25 J/mm at a fixed laser power of 300 W. A similar trend was also observed by Sadowski et al for LPBF of Inconel 718 [29]. However, here, a general upward trend for both the width and depth of the melt pool is observed while increasing the laser power at a constant LED. For instance, at a constant LED of 0.25 J/mm, the melt pool depth and width change around 25% and 4%, respectively with changing laser power from 150 W to 300 W and scanning speeds from 600 mm/s to 1200 mm/s.

The higher LED results in a higher energy input into the system, therefore it is expected to produce a bigger melt pool geometry which can be confirmed by the data presented in Figure 30 (a,b). It is also reported by Aversa et al [30] that a higher LED value for a single line dramatically increases the depth of the melt pool of AlSi10Mg alloy. A lower LED with a shallower melt pool results in a smaller contact area between the molten metal and the substrate. As a result, there is less wetting of the molten metal on the surface and the tracks become more irregular or undergo balling before solidification [50]. To avoid this, process parameters need to be carefully selected to create an appropriate melt pool depth.

Results in Figure 30 can also be used to analyze the effect of layer thickness on the melt pool geometry of printed single tracks. However, it is in contrast to what has been observed in the literature where increasing layer thickness results to have shallower melt pools and more balling observed for a single track [50]. Results from the current study show no specific deviation for the geometry of the melt pool when the nominal layer thickness changed from 20 µm to 60 µm.

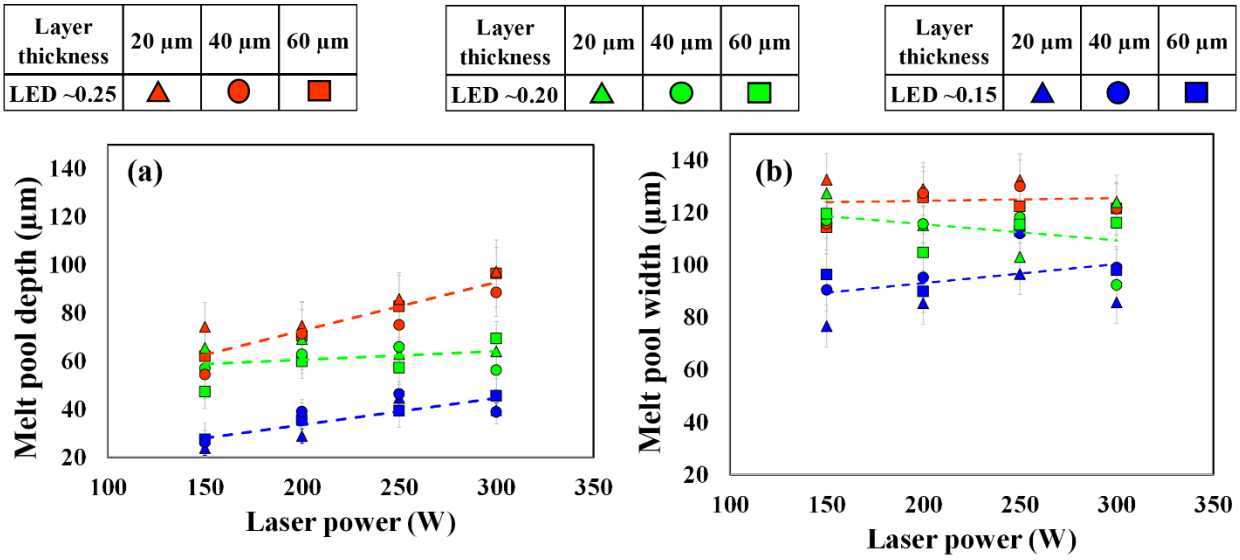

Figure 30. (a) The depth and (b) width of the melt pool as a function of laser power in three different LED values of 0.15, 0.2, and 0.25 (J/mm).

As was observed in Figure 30, melt pool dimensions do not show any significant change with the change in last layer thickness. Insignificant changes in the melt pool dimensions of single tracks with respect to different layer thicknesses may be due to the fact that the effective powder layer thickness is much bigger than the nominal or build layer thickness as reported by Mahmoodkhani et al. [51]. The actual layer thickness in LPBF is not constant and increases from the beginning of the process to reach a steady-state known as the effective layer thickness (ELT) [52,53]. In this study, since only the last deposited layer's nominal thickness was changed from 20 to 60 µm, the effective layer thickness from former layers appears to be dominant in terms of controlling the melt pool geometry.

Insignificant changes in the melt pool size by changing the layer thickness could also be explained due to the surface roughness of the previous layer. It is well known that the rough surface of the last deposited layer makes height to be different at different locations on the top surface during the LPBF manufacturing process [54]. This leads to a non-uniform powder layer added by the recoater for subsequent layers which may be greater than the nominal layer thickness thus negating the effect of changing layer thickness on melt pool dimensions. Figure 31 demonstrates the height map of the top surface of the printed Hastelloy X

substrate with printed single tracks. Measurement along the single-track deposition (white line in Figure 31) shows up to 80 µm variation in height of the substrate, which is much larger than the maximum nominal layer thickness (60 µm) used in this study. This variation in height affects the local layer thickness of powder during the next deposition step and therefore does not show any effect of layer thickness on melt pool dimensions of printed single tracks.

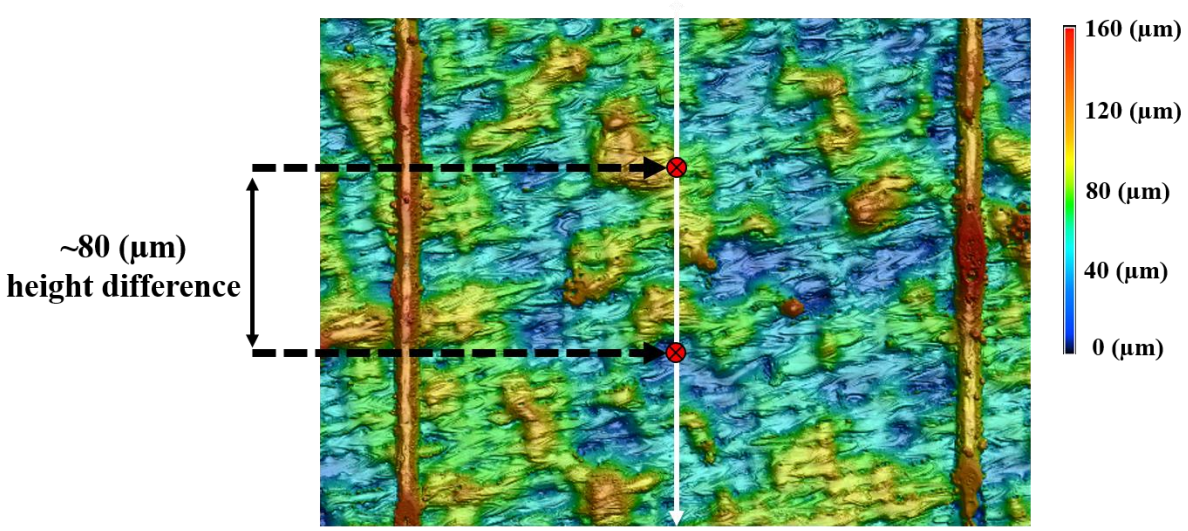

Figure 31. Line scanning of the substrate parallel to single track deposition from top view shows about 80 µm difference in height of the last deposited layer which makes the variation of nominal layer thickness (from 20-60 µm) for the last layer deposition insignificant.

Experimental results from melt pool dimensions with varying laser power and LED show the effect of melt pool width and depth with fixed LED. However, it is important to investigate the effect of laser power and velocity individually. Figure 32 illustrates the effect of changing the LED from 0.15 J/mm to 0.25 J/mm on the melt pool dimensions at a constant power or velocity. Results in Figure 32 (a) and (b) show that whilst keeping the scan velocity constant, decreasing the LED from 0.25 J/mm to 0.15 J/mm results in about a 65% and 30% decrease in melt pool depth and width, respectively. While with fixed power and decreasing LED from 0.25 J/mm to 0.15 J/mm results in about 38% and 13% reduction in melt pool depth and width correspondingly. Therefore, increasing the scanning velocity has a weaker influence on the melting regime compared to a proportional increase in laser power.

As discussed previously, the impact of change in laser power is stronger than corresponding changes in scanning velocity on the melt pool geometry. It is also observed that the melt pool width is larger than the laser beam spot size (80 µm) due to the heat dissipation from molten metal to solid material. Considering the Gaussian distribution of the laser heat source, the average laser radiation intensity at the center of the beam profile is considerably higher than the intensity at the edges [53,55]. Also, due to the Gaussian

distribution, the input energy at the edges is less sensitive to the laser power or scanning velocity changes than at the center. The higher intensity at the center of the laser beam leads to an increase in the surface temperature of the melting metal to the boiling temperature of the metal, which causes recoil pressure on the melt pool and leads to the surface depression in this area [56–58]. This depression, along with higher temperatures at the central zone of the melt pool, provides a driving force for the melt pool penetration while increasing the melt pool depth. This explains the greater sensitivity of the melt pool depth when compared to the width when input energy is changed either by the varying scanning velocity or laser power.

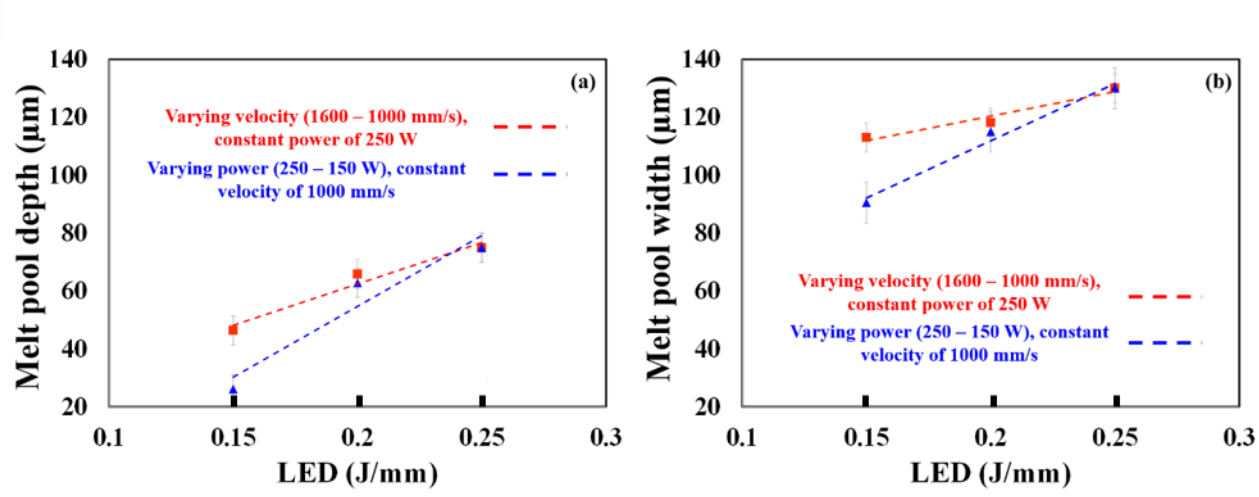

Figure 32. (a) The depth and (b) width of the melt pool as a function of LED with two different passes of changing Velocity and laser power.

It is well known that microstructure can be affected by variation in process parameters [15,37,59]. Figure 33(a) and (b) show SEM images with LEDs of 0.25 J/mm and 0.15 J/mm at laser powers of 300 W and 150 W respectively. Results from Figure 33 (a) and (b) show the cellular structure of the melt pool area at low magnification from cross-sectioned deposited single tracks. A similar cellular structure is observed from Co-based and Ni-base LPBF parts with FCC crystal structure [18,60–62].

SEM images at higher magnification were also captured to analyze the cellular spacing at fixed LED and varying laser power and velocity. Figure 33 (c) and (d) demonstrate the cellular microstructure of single tracks printed with a constant LED of 0.25 J/mm with a laser power of 150 W and 300 W, respectively. Comparing the microstructures reveals that at a fixed LED, the cell size increased from ~285 nm to ~500 properties such as hardness [63,64], it is important to individually investigate the variation of cell spacing

with respect to the fixed LED criteria. Reduction in cell spacing results in higher hardness [63,64] due to a higher number of cell boundaries enriched by dislocations [60,61].

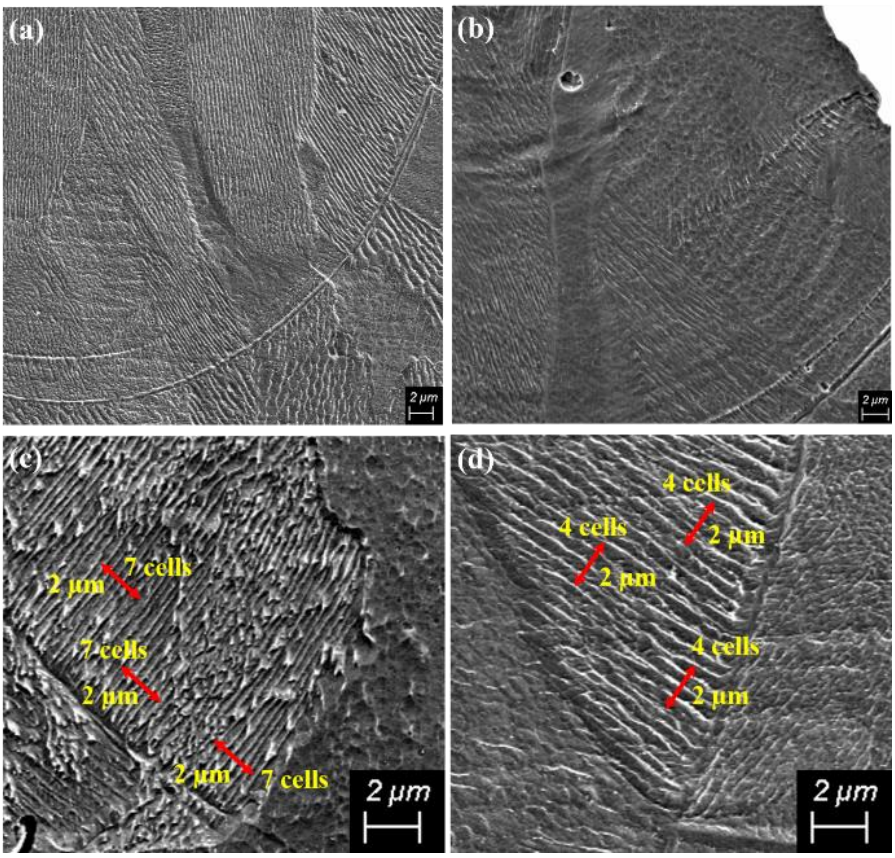

Figure 33. SEM micrographs showing cell structure from the cross-section of deposited single tracks with (a) LED value and laser power of 0.25 (J/mm) and 300 (W) (b) LED value and laser power of 0.15 (J/mm) and 150 (W). In higher magnification, SEM micrographs at melt pool boundaries show the microstructure created by an LED value of 0.25 (J/mm) and laser power of (c) 150 (W) and (d) 300 (W).

Cell spacing in the microstructure strongly depends on the cooling rate at the solid-liquid interface during solidification [59]. High-temperature gradients (G) and high solidification rate (R) in the melt pool result in a higher cooling rate. This higher cooling rate leads to a higher super-cooling and finer cellular structure [65]. As absorbed heat in the melt pool dissipates from the boundary of the melt pool to the surrounding substrate, an approximation of the cooling rate can be established based on the ratio of the melt pool volume (V_s) to boundary area (S_b). A smaller $\frac{V_s}{S_b}$ would result in faster heat dissipation to the substrate and hence, a higher cooling rate during the solidification. On the other hand, a larger $\frac{V_s}{S_b}$ would result in a lower cooling rate. To be able to compare the solidification condition of single tracks fabricated at equivalent LED values with different laser powers, Figure 34 shows the $\frac{V_s}{S_b}$ ratio (which is estimated from the ratio of the melt pool area to the melt pool boundary measured from the cross-sections considering a unit deep in the plate of

single track images) as a function of laser power at constant LED of 0.25 J/mm. As observed, the higher laser power causes a larger $\frac{V_s}{S_b}$ ratio, which leads to lower cooling rates during solidification. Similarly, a lower $\frac{V_s}{S_b}$ the ratio is observed at lower laser power which corresponds to higher cooling rates thus resulting in finer cellular structure compared to the higher laser power fabrication with an identical LED value (Figure 33 (c) and (d)).

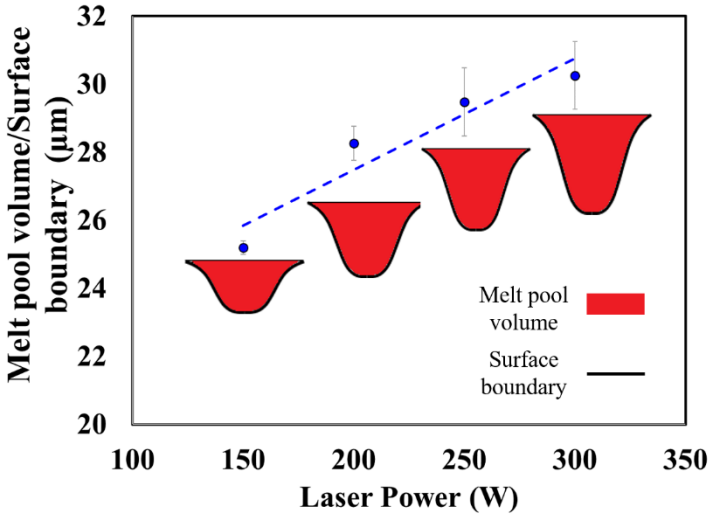

Figure 34. The ratio of melt pool volume to the surface boundary as a function of laser power. Results measured from cross-sections of single tracks deposited with the LED value of 0.25 (J/mm).

It has been established that the cooling rate changes with different process parameters at the same LED. Also, as cooling rate is directly proportional to the temperature gradient and solidification rate ($\dot{T} = G \times R$), a change in cooling rate, suggests a change in G and R at different process parameters for the same LED. Moreover, it is well known that $\frac{G}{R}$ can be employed to identify the solidification mode and resulting cellular, dendritic, or equiaxed structures [59]. Hence, to investigate the possibility of changing solidification modes by varying process parameters of LPBF, two extremes of the current process window are selected (the lowest LED value with the lowest laser power and the highest LED value with the highest laser power). It is observed that a cellular structure is the dominant solidification mode of the LPBF process within the range of selected process parameters (as shown in Figure 33 (a) and (b)). It is worth mentioning that the cellular growth of crystals is not restricted to the melt pool boundary region and continues during solidification as shown in Figure 33 for both extreme parameters, leading to a cellular structure for the entire melt pool. Therefore, it can be concluded that the change in cooling rate at different process parameters affects the temperature gradient and solidification rate on the printed single tracks. However,

this change in cooling rate does not affect the final solidification mode as the $\frac{G}{R}$ is always in the range of cellular structure.

The cellular structure of additively manufactured parts is also reported for Co-29Cr-6Mo alloy which has cellular structures throughout the melt pool where the cooling rate is estimated to be around 2.2×10^6 K/s [18]. However, this is in contrast to what is observed at lower cooling rates of around 3.8×10^4 K/s in AlSi12 alloy, which has a clear transition from a dendritic (at the boundary) to a microcellular structure (in the middle of melt pool) in the deposited layer [66]. On the other hand, AlSi10 shows an almost completely cellular structure in the LPBF part with an estimated cooling rate of 2×10^6 K/s [67]. This reveals that the solidification mode is material dependent, thus each material needs to be studied individually to analyze the associated microstructure. For Hastelloy X, the cooling rate can be estimated from $\lambda = 97\dot{T}^{-0.36}$ where λ is primary cell spacing and $\dot{T}$ is the cooling rate [18,62]. Based on the current experiment, by changing the laser power at LED of 0.25 J/mm, the measured primary cell spacing changes from 0.285 ± 0.05 µm to 0.5 ± 0.1 µm (Figure 33(c) and 5(d)) which lead to a cooling rate from 1.5×10^7 K/s to 2.2×10^6 K/s. This decrease in the cooling rate of around 85% occurs when the ratio of $\frac{V_s}{S_b}$ increases by ~20% at LED of 0.25 J/mm and laser power of 150 W and 300 W.

Results from the cell structure analysis of single tracks at fixed LED shows the variation in cell spacing due to the difference in cooling rates. However, it is also important to study the effect, if any, on the grain morphology. This is important as grain morphology has been linked to material performance such as yield strength [64,68,69]. Figure 35a-b shows inverse pole-figure maps of two cross-sectioned single tracks at a LED value of 0.25 J/mm with laser power of 150 W and 300 W. Melt pool boundaries have been detected from optical images of etched samples and superimposed on the EBSD maps. EBSD results in Figure 35 show the melt pool and the bead area from the cross-sectioned single tracks. Melt pool IPF maps show the grain growth due to grain growth at the melt pool boundary for both cross-sections in the building direction. Similar results of epitaxial growth have also been observed by other research groups from the microstructure of LPBF parts [15,32,60]. In addition, a few nucleated grains are also observed in the middle of the melt pool with a misorientation of more than 15˚ with neighboring grains. A total of 5 new grains (highlighted in Figure 35(a)) were identified with the lower laser power (150 W), whereas 11 new grains (highlighted in Figure 35(b)) were observed with the higher laser power (300 W) at the same LED value. The average number for new grains, which are observed from different cross-sections, was calculated to be about 6±2 and 11±1 for laser power of 150 W and 300 W, respectively. This difference in the number of grains would result in a finer grain structure that would affect the mechanical properties of the printed parts.

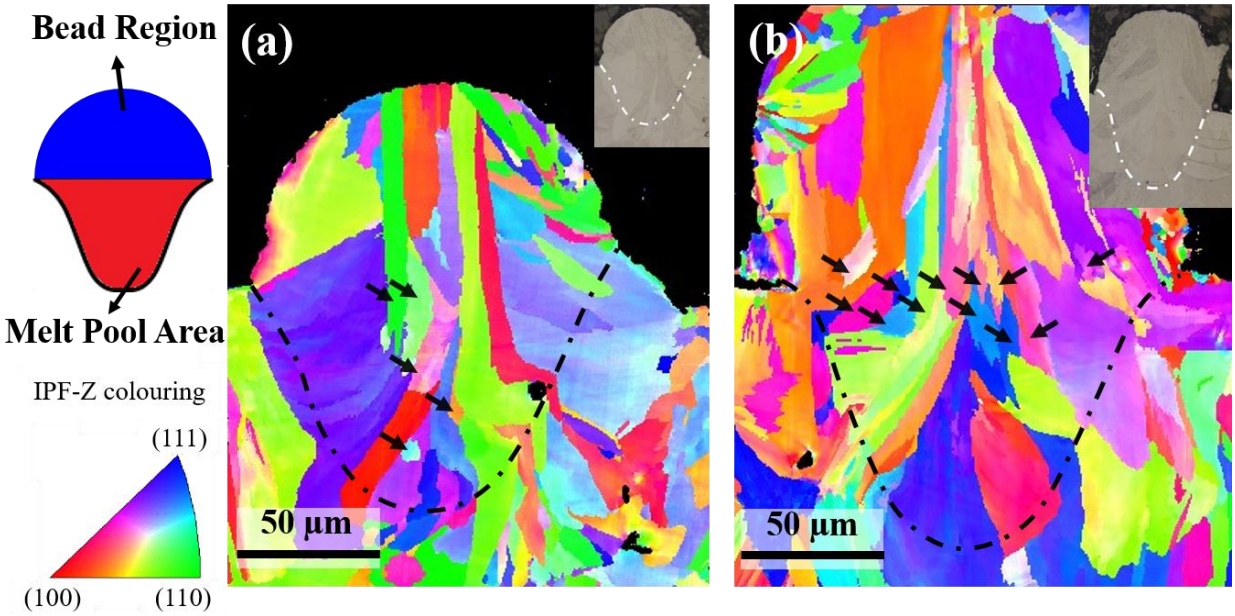

Figure 35. EBSD inverse pole-figure map from deposited single tracks with the LED value of 0.25 (J/mm) and laser power of (a) 150 (W) and (b) 300 (W). Dashed lines correspond to melt pool boundaries which are detected from OM pictures of etched cross-sectioned samples (shown as inserts).

As grain nucleation is observed in the melt pools from EBSD results, it is important to identify the nucleation mechanisms for the presence of new grains. Four different nucleation mechanisms namely; dendrite fragmentation, surface, homogenous/heterogeneous nucleation, and grain detachment have been identified during the rapid solidification of metallic alloys [59]. Due to the existence of cellular structure observed in the single tracks (Figure 33), the possibility of a dendrite defragmentation mechanism is very low. Also, since epitaxial grain growth is observed in the melt pool of single tracks, surface nucleation is not a viable option. If the solute partition coefficient of alloying elements is less than 1, it is possible to have solute pile-up in front of the solid-liquid boundary during solidification, which results in the segregation of alloying elements [70]. Segregation in front of the solid-liquid interface can lead to the high constitutional undercooling, which should be followed by homogenous nucleation of equiaxed grains in the middle of the melt pool [71]. However, according to the EDS line scanning analysis for the single track deposition, it is shown in Figure 36 that there is no significant segregation of main alloying elements along the melt pool depth. It should be noted that allowing elements such as Mo, Ti, and Al which are second phase stabilizer remains constant in the depth of the melt pool. EDS line scanning of melt pools was repeated for two different cross-sections of single tracks with LED of 0.15 J/mm and LED of 0.25 J/mm. Results from both extreme LED values show a lack of segregation in printed Hastelloy X samples. This lack of segregation may be attributed due to the rapid solidification of the melt pool region during the LPBF process [62]. EDS results (Figure 36) show a lack of segregation in the concentration of alloying elements which would not change the undercooling temperature of the melted metal at the center of the melt pool.

As homogeneous nucleation rate is linked to segregation of alloying elements [72], it can be concluded that the observed changes in nucleation rate in Hastelloy X is not due to this mechanism.

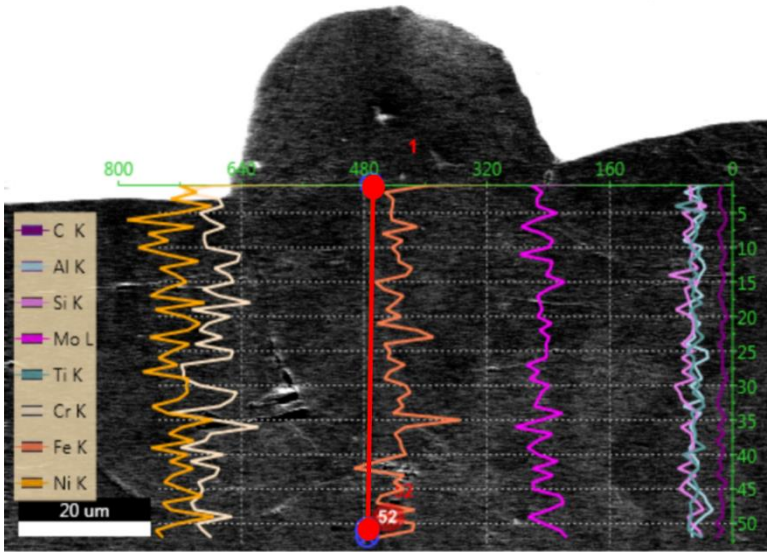

Figure 36. EDS line scanning along with red line shown in the picture showing no specific amount of segregation of the main alloying element during the solidification of single track Hastelloy X. Analysis coming from a cross-section of melt pool area deposited by the LED value of 0.25 (J/mm) and laser power of 300 (W).

Based on the discussion presented thus far, grain detachment might be the best explanation for the nucleation of the grains in the melt pool during solidification. Due to the Bernoulli effect, metal evaporation during the LPBF process enables the flow of inert gas (argon) toward the middle of the melt pool [53]. With the help of high-speed imaging, it is shown that this inert gas flow from the surrounding is strong enough to start the flow of powder particles towards the melt pool [53]. Some of these particles become part of the melt pool while others attach to the periphery. The partially melted particles attach to the solidified metal and may act as nucleation sites for grain growth. On the other hand, molten metal from these PMPs could enter the melt pool to create a potential nucleus inside the melt pool causing grain detachment. SEM secondary mode image and EBSD IPF maps from a cross-sectioned single track are presented in Figure 37. In addition to that, Figure 37 shows three attached particles surrounding the bead region (shown by red areas of A, B, and C). These attached particles might have originated from adjacent powders or spatter particles produced during LPBF. As new grains formed around the periphery of the attached particles do not show epitaxial growth, it can be concluded that grain detachment is the dominant mechanism. Results from attached particle show a significant amount of new orientated grains in the solidified bead region. All the attached particles (A-C) show detached grain growth along with heat flow direction after reaching a substantial under cooling temperature. The bigger size of the attached particle C

leads to have more newly orientated grains in the microstructure on the left side of the melt pool when compared to the particle B in Figure 37.

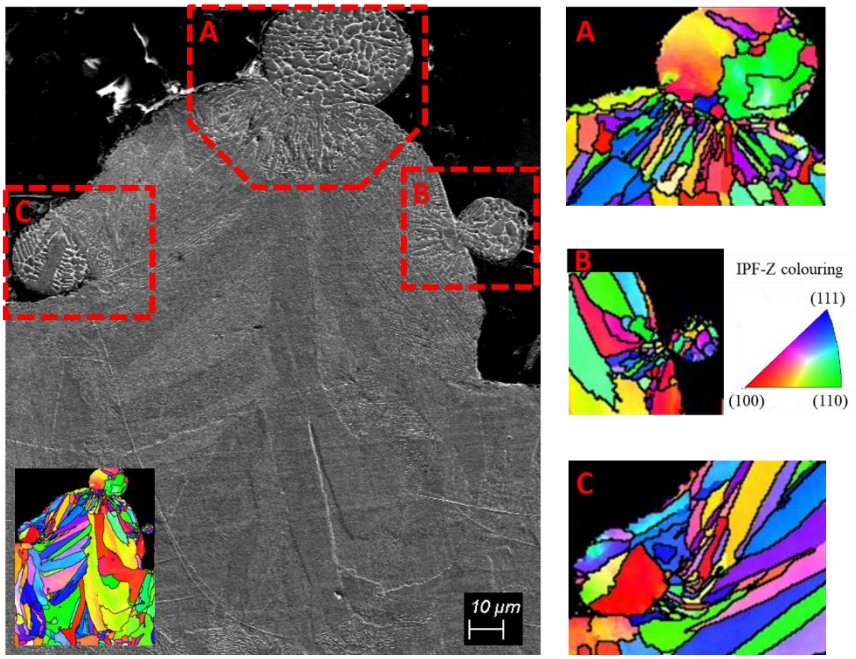

Figure 37. SEM secondary mode of imaging including EBSD inverse pole-figure map from highlighted areas of the single track deposited with an LED value of 0.25 (J/mm) and laser power of 300(W). PMPs attached to a single track show a significant amount of nucleation with new grains.

IPF maps shown above highlight the formation mechanism for new grains in the solidified single track. However, results in Figure 35 show a difference in the number of new grains between solidified melt pools from different laser powers at the same LED. It is observed, that the melt pool width always exceeds the laser beam diameter and the melt pool width is proportional to the laser power (Figure 32 (b)). Therefore, a higher laser power creates a melt pool larger than the laser diameter. This area can be distributed into the hot and cold regions where the hot region corresponds to the area under direct laser irradiation while the cold region corresponds to the difference between the direct laser irradiation and the melt pool width (Figure 38 (a)). Any powder in the hot section would melt completely. However, powder in the cooler band may partially melt and remain in the melt pool as a PMP. However, this cooler band is directly proportional to the laser power. For example, a cooler band increase from ~37 µm to ~45 µm is observed when the laser power is increased from 150 W to 300 W at fixed LED. As the cooler band increases with laser power, the number of PMPs in the melt pool would also increase. As these particles have been shown to cause nucleation in the melt pool, a higher number of PMPs would result in more grains inside the melt pool as shown in Figure 35. Moreover, while the laser irradiation is directly above the area of interest, Marangoni

convection of surface molten metal flows from the center to the periphery of the melt pool [8]. This pushes PMPs to cooler bands until the laser beam passes. This results in an average of 5 more nucleated grains within the melt pool with higher laser power at constant LED (Figure 35).

The increase in PMP observed at higher power can also be attributed to the denudation zone created during laser irradiation [56]. It has been reported that higher laser power results in a wider denuded powder zone around the single track [73]. In addition, laser power has a higher effect than the scanning velocity on the denudation zone [73]. Based on this, higher laser power would result in the addition of more powder particles in the melt pool which would increase the probability of the existence of PMPs.

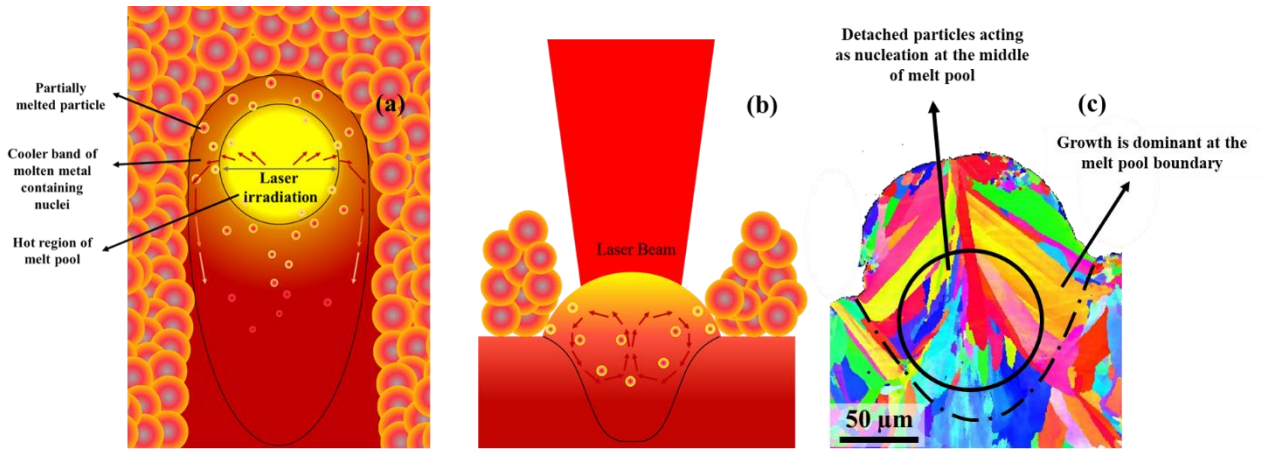

Figure 38. Schematic overview of single track deposition with melt pool flows from (a) top view of single track and (b) longitudinal cross-section. (c) EBSD inverse-pole figure map showing a random orientation of small crystals from PMP in the middle of the melt pool region.

3.4 Conclusion

In this work, independent of the laser power, scanning velocity, and layer thickness, changing the LED (defined as the ratio of beam power to scanning velocity $\frac{P}{V}$ ($\frac{J}{mm}$) value) resulted in significant effects on the geometry of the melt pool in Hastelloy X. However, keeping the LED constant at different laser powers and process speeds did not necessarily result in the same melt pool geometry or microstructure. The following points express the most important conclusions of this study:

- The laser power has a higher effect on the melt pool dimensions than the scanning velocity. Decreasing the laser power with fixed scanning velocity (LED from 0.25 J/mm to 0.15 J/mm) results in about a 65% and 30% decrease in melt pool depth and width respectively. Similarly, increasing the scanning speed at a fixed power (LED from 0.25 J/mm to 0.15 J/mm) results in about 38% and 13% reduction in melt pool depth and width respectively.

- At fixed LEDs, variation in melt pool dimensions is unavoidable due to the stronger influence of the laser power on the melting regime. For example, at an LED of 0.25 J/mm, increasing the laser power from 150 W to 300 W results in increasing the melt pool depth by ~56%.
- It is proposed that the difference in average primary cell spacing (from 285 nm to 500 nm at LED of 0.25 J/mm) with an increase in laser power from 150 W to 300 W is linked with the cooling rate and can be explained by the change in the ratio of $\frac{melt\ pool\ volume}{surface\ boundary}$.
- In general, the microstructure of the cross-section single track melt pools shows a cellular structure with epitaxial growth of grains at melt pool boundaries. However, at fixed LED of 0.25 J/mm a ~90% increase in new grains is observed in the solidified melt pool which results in a finer microstructure at the laser power of 150 W and 350 W respectively.
- Based on experimental EBSD results, it is proposed that the increase in the number of new grains observed in solidified melt pools is due to grain detachment caused by the higher number of survived partially melted particles (PMPs). The increase in the survived PMP at fixed LED of 0.25 J/mm from 150 W to 300 W is probably due to the increase in the width of the cooler band (from ~37 µm to ~45µm) of molten metal that acts as nucleation sites during solidification.

4 Solidification simulation of laser powder-bed fusion: Implementation of a phase-field model coupled with melt pool temperature gradient

4.1 Introduction

Additive manufacturing (AM) became a fast emerging technology during the past decades due to its exceptional manufacturing capabilities. Manufacturing near net shape parts with complex geometries and design freedom are some important benefits of utilizing AM techniques. Laser powder-bed fusion (LPBF) is one of the favored AM techniques in which laser heat-source melts the spread powder and deposit the metallic material during the subsequence solidification process [74]. To ensure the desirable properties (such as mechanical or physical properties), it is essential to gain a deep understanding of the solidified microstructure [75]. In this regard, solidification simulation is a powerful tool to predict the microstructure of the solidified materials when the process condition varies during an optimization process.

During the past few years, some attempts for microstructural simulations have been done for the LPBF process [76]. For instance, Johnson et al. simulated the grain structure of an LPBF part using a kinetic Monte Carlo model [77]. Their model is shown to be powerful in equiaxed to columnar transition prediction but weakens when the simulated grain size is compared to the experimental result [77]. On the other hand, Cellular Automata (CA) is an adoptive tool to simulate the solidified grain morphology during the LPBF process [78]. For example, by implementing a CA-based model, Akram et al. [79] showed a good agreement in morphology between simulated columnar grains and experimentally formed grains. However, the prediction of stand-alone CA models is mostly limited to the grain scaled futures [80]. To reach a higher accuracy in prediction, phase-field models can be beneficial due to their capability of including multi-physics into the problem. Acharya et al. [75] utilized computational fluid dynamics coupled with a phase-field model to simulate the dendritic grain growth, elemental segregation, and crystallographic orientation. However, simulation results are limited to a single-track solidification due to the complexity of the problem.

In this study, we focused on the most important physical phenomena, which are involved in competitive grain growth during the LPBF solidification. Therefore, we employed a phase-field model to consider multi-physics that are elaborated in the non-equilibrium LPBF solidification including solidification anisotropy, temperature gradient, and nucleation process. It should be

noted that the current work aims to achieve the highest accuracy on grain structure prediction in a wide computational window with the lowest computational cost. Therefore, for simplification, we assume that the effect of elemental segregation is negligible on grain structure [48]. As a result, the prediction of the second phases and related phenomena is out of the scope of the current study. The grain structure simulation is divided into 3 different sections including single-track, multi-track, and multi-layer solidification simulations. Each section includes an experimental validation to show the exceptional accuracy of the phase-field model. Side-branching of grains is observed in simulated microstructure and their existence is confirmed in the experimental result. Simulated grain structure shows less than 10% difference in grain dimension compared to what is measured from experimented microstructure. Simulation results discovered that change in the strength of anisotropy significantly influence the crystallographic texture, while the change in the semi-solid interface thickness greatly impacts the length of columnar grains.

4.2 Model description

In this study, a 3D micro-scale finite element model is employed to simulate the initial thermal gradient and melt pool geometry during an LPBF process. Then a phase-field model coupled with thermal gradient is implemented to simulate the competitive grain growth and as a result, the final grain structure after complete solidification.

4.2.1 Macro-scale heat source model and melt pool simulation

In this work, commercial software COMSOL Multiphysics is used to predict temperature gradient and melt pool geometry prior to the solidification [81]. The governing equation for a 3D heat-transfer is described by Zhang et al. [82] when the effect of convection is assumed to be negligible:

$$\rho C_p \frac{\partial T}{\partial t} = \frac{\partial}{\partial x}\left(k_x \frac{\partial T}{\partial x}\right) + \frac{\partial}{\partial y}\left(k_y \frac{\partial T}{\partial y}\right) + \frac{\partial}{\partial z}\left(k_z \frac{\partial T}{\partial z}\right) + Q \qquad (1)$$

where T is temperature, t is time, $C_p$is specific heat, ρ density, Q is the volumetric heat source, and k_x, k_y, k_z are the thermal conductivity of x, y, and z directions.

For the volumetric heat source (Q), a conical-Gaussian model is used [83,84]:

$$Q_v(r,z) = Q_0 \exp\left(-\frac{2{r_0}^2}{r_z^2}\right) \qquad (2)$$

where Q_v is heat intensity distribution, Q_0 is maximum heat intensity value, r_0 is the radius of the heat source on top, and r_d is the bottom radius of the heat source profile and can be obtained from the following equation:

$$r_0(z) = r_0 - (r_0 - r_d)\frac{z_e - z}{z_e - z_i} \qquad (3)$$

where z_e and z_i are z coordinates of the top and bottom of the cone, respectively.

The maximum heat intensity value (Q_0) can be calculated based on thermal energy conservation which is discussed more in-depth in the previous study [81].

4.2.2 Meso-scale solidification simulation

The thermal gradient is obtained from the 2D cross-section (perpendicular to track direction) of heat-source simulation is imported as an input to the solidification simulation. A finite-difference phase-field model with a uniform mesh size of 0.2 μm is implemented for the solidification process.

4.2.2.1 Initialization

To simulate gain growth accurately, each track solidification should be simulated individually. Therefore, the initial computational domain contains the melt pool, the surrounding substrate, and the ambient atmosphere. Random grain orientation has been assigned to single track's melt pool boundaries which are in touch with metal powder, while the orientation of existing grains is used for the rest of melt pool boundaries. After setting the initial condition, a phase-field model is utilized to simulate the solidification and grain growth as followed.

4.2.2.2 Phase-field solidification model

Two main variables play an important role in the model: a temperature field ($\tilde{T}$) and a phase-field (p) both as a function of location (r) and time (t). The ordering parameter p defines the liquid phase (with $p = 0$) and solid phase (with $p = 1$). Nodes at the interface of liquid/solid have p values between 0 and 1 which express the semi-solid state of the interface layer. To track changes in phase-field parameter (p), the whole system is described by the following free-energy which includes the m parameter [85]:

$$\emptyset[p,m] = \int \frac{1}{2}\varepsilon^2|\nabla p|^2 + F(p,m)\, dr \qquad (4)$$

where ε is defining the solid/liquid interface thickness with a considerable small value. It is also can control the mobility of the solid/liquid interface and will be used to introduce the anisotropy of solidification. F is a double-well potential function in which its two local minimums (at $p = 0\ , 1$) may vary by changing the m parameter:

$$F(p,m) = \frac{1}{4}p^4 - \left(\frac{1}{2} - \frac{1}{3}m\right)p^3 + (\frac{1}{4} - \frac{1}{2}m)p^2 \qquad (5)$$

The m parameter is set to change between $[-\frac{1}{2}, \frac{1}{2}]$. Since the global minimum of the F function is completely dependent on the m value (Figure 39), it is assumed that m is the function of the temperature field:

$$m(T) = \left(\frac{\alpha}{\pi}\right)\tan^{-1}[\gamma(\tilde{T}_e - \tilde{T})] \qquad (6)$$

where T_e is the equilibrium temperature, α and γ are positive constant. To ensure the former restriction on the m parameter ($|m| < \frac{1}{2}$) is satisfied, the α parameter must be less than 1. The term $\left(\tilde{T}_e - \tilde{T}\right)$ in Eq.6 implies that the driving force for solidification should be proportional to the undercooling temperature and result in faster or slower mobility of solid/liquid interface.

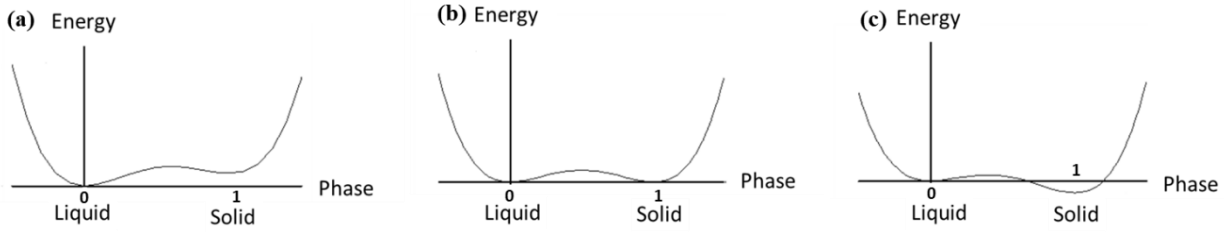

Figure 39. Change in double-well potential function by different m parameter of a) m<0, b) m=0, and c) m>0.

To introduce the anisotropy in crystal growth, we follow the previous idea proposed by [86,87] and define the ε parameter as a function of direction:

$$\varepsilon(\theta) = \bar{\varepsilon}\eta(\theta) \qquad (7)$$

where $\bar{\varepsilon}$ indicates the average value of the solid/liquid interface (ε) and $\eta(\theta)$ represent the anisotropic behavior of growth and defined as follows:

$$\eta(\theta) = 1 + \omega \cos[k_\varepsilon(\theta - \theta_0)] \qquad (8)$$

where ω is a constant which shows the strength of anisotropy, k_ε is the mode of anisotropy which is 4 for an FCC material. θ_0 is the easy growth direction of the crystal, and θ is the direction which is perpendicular to the solid/liquid curvature and can be derived from the primary phase field parameter [86]:

$$\tan\theta = \frac{dp/dy}{dp/dx} \qquad (9)$$

Considering the fact that the phase parameter (p) is not a conserved quantity, the evolution of the phase-field parameter can be described as [85–87]:

$$\tau \frac{\partial p}{\partial t} = -\frac{\delta \emptyset}{\delta p} \qquad (10)$$

Substituting $\emptyset$ variable in Eq (10) using Eq (4,5) result in an expanded form of the phase-field equation as follows:

$$\tau \frac{\partial p}{\partial t} = -\frac{\partial}{\partial x}(\varepsilon\varepsilon' \frac{\partial p}{\partial y}) + \frac{\partial}{\partial y}(\varepsilon\varepsilon' \frac{\partial p}{\partial x}) + \nabla.(\varepsilon^2 \nabla p) + p(1-p)(p - \tfrac{1}{2} + m) \quad (11)$$

where ε' means $\frac{d\varepsilon}{d\theta}$. The Eq (11) is practically useful when the phase-field parameter (p) is changing in time or location. Therefore, its practical meaning is in the vicinity of the solid/liquid interface. In this regard, to reduce the computational cost of the program, we only apply (11) to the area in the neighborhood of the moving solidification interface.

To consider the enthalpy law, temperature field ($\tilde{T}$) is derived from the following equation:

$$\frac{\partial \tilde{T}}{\partial t} = \nabla^2 \tilde{T} + \mathrm{C} \frac{\partial p}{\partial t} \qquad (12)$$

where C is a non-dimensionalized parameter and it is proportional to $\frac{L_f}{k}$ ($\frac{Latent\ heat\ of\ fusion}{thermal\ conductivity}$) and it is inversely relative to the strength of cooling. It should be noted that the model emphasis a dimensionless $\tilde{T}$ parameter, whereas temperatures form the lowest to a characteristic temperature, are ranked from 0 to 1 and any temperature above that are linearly extrapolated. This will keep the

$\tilde{T}$ the parameter in the same order of magnitude of p and correctly represent the temperature gradient in the system. However, to be precise, the temperature parameter ($\tilde{T}$) can be updated with the actual T which is driven from Eq (1) and COMSOL simulation.

Previous studies show that most grains grow from epitaxial nucleation on the pre-existing grains at melt pool boundaries [15,88,89]. However, recent studies revealed the existence of bulk nucleation which significantly affects the grain structure of LPBF parts [88–90]. To include epitaxial nucleation, instant nucleation forms on the melt pool boundary with the same orientation of the parent grain and start to grow when the temperature field ($\tilde{T}$) is lower than the equilibrium temperature. For bulk nucleation, an empirical and adoptive nucleation density (N) can be defined as a function of the supercooling temperature (ΔT) [91,92]:

$$N = \int_0^{\Delta T} \frac{dN}{d(\Delta T')} d\Delta T' \qquad (13)$$

The term $\frac{dN}{d(\Delta T)}$ is indicating the sensitivity of nucleation with respect to the undercooling and can be estimated by a Gaussian distribution given by [92]:

$$\frac{dN}{d(\Delta T)} = \frac{N_0}{\Delta T_\sigma \sqrt{2\pi}} e^{\left(-\frac{\Delta T - \Delta T_c}{\sqrt{2}\Delta T_\sigma}\right)} \qquad (14)$$

where $N_0, \Delta T_\sigma, \Delta T_c$ are nucleation parameters and should be tuned based on material and solidification conditions. The effect of partially melted powder (PMP) nucleation, however, should be added to the system. To include both nucleation types, we set the total number of nucleation sites (N) in the single track from the previous single track experiment [90] in which a range of N has been identified for a particular process parameter of a single melt pool.

4.3 Experimental procedure

To fabricate the LPBF validation parts, Hastelloy X powder supplied by EOS GmbH, with the chemical composition listed in Table 4 is used. Also, Figure 28 shows the SEM image of powder particles and it is observed that the morphology of the powders is mostly with some attached satellite particles.

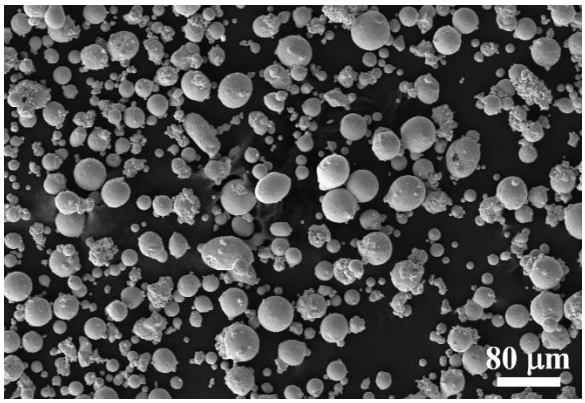

Figure 40. SEM image of powder metal showing the spherical morphology of particles with attached satellites.

Table 6. Nominal composition (in wt.%) of Hastelloy X gas-atomized powder used for selective laser melting process [42].

Ti	Al	Cu	Mn	Si	C	Co	W	Mo	Fe	Cr	Ni
<0.15	<0.5	<0.5	<1	<1	<0.1	1.5 ± 1	0.6 ± 0.4	9 ± 1	18.5 ± 1.5	21.75 ± 1.25	balance

The experimental part was designed to manufacture 3 rectangular substrates of Hastelloy X with base dimensions of 25 mm × 17.5 mm × 5 mm. Each substrate refers to a different part of the simulation validation process which includes single track, multi-track, and multi-layer validation. Three laser scans were applied on top of each 3D printed substrates to deposit single-tracks, multi-tracks, and multi-layers with 25 mm length (Figure 29). Also, high magnification of the cross-sectional view of each laser scan trajectory is shown in Figure 41 (a-c).

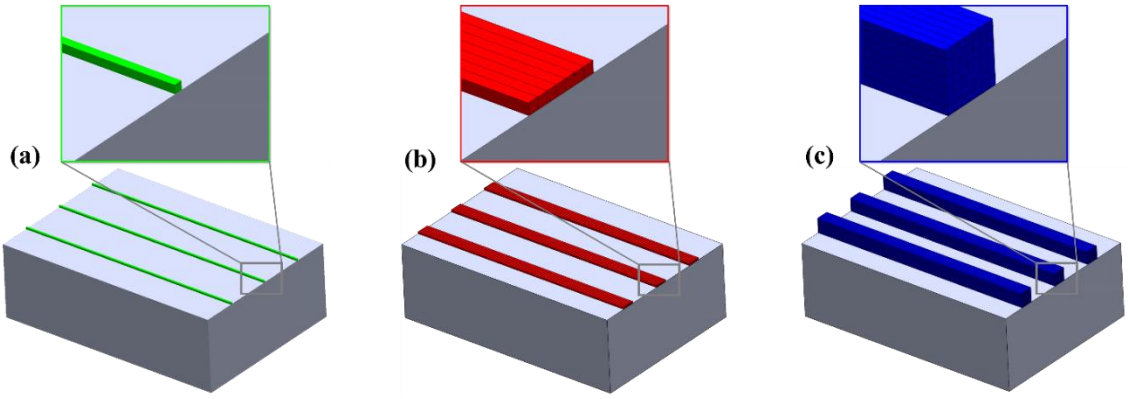

Figure 41. The printed substrate with (a) single-track, (b) multi-tracks, and (c) multi-layer trajectories for experimental validation. The cross-sectional view of each trajectory is shown in a high-magnification image.

EOS M290, equipped with a Ytterbium fiber laser, was used for fabricating the substrates and single tracks. The laser beam profile of EOS M290 is reported to have a 100 µm diameter spot

size. All substrates were designed with the same process parameters as default EOS Hastelloy X parameters. After reviewing the process parameters used in available literature for Hastelloy X [63,64,93–95], a specific process parameter is selected for single-tracks, multi-tracks, and multi-layer depositions. Table 7. Sets of process parameters including laser powers (P), scanning velocity (V), hatch spacing (H), and Layer thickness (t) for experimental studies. shows the selected process parameters in this study. After the fabrication process, the completed specimens were cross-sectioned using a Struers Accutom-50 precision cutter for a total of 4 cross-sections per single track condition. The single-track study is designed to obtain many unknown parameters for a Hastelloy X crystal. This is mostly done by tuning phase-field parameters while getting the closest prediction compared to experimental result. In the next steps (multi-track and multi-layer studies), obtained coefficients from single-track calibration will be used to predict the microstructure.

Table 7. Sets of process parameters including laser powers (P), scanning velocity (V), hatch spacing (H), and Layer thickness (t) for experimental studies.

Study	Laser Power (W)	Laser scanning speed (mm/s)	Hatch spacing (μm)	Layer thickness (μm)
Single-track	200 (W)	V = 1000 mm/s	-	-
Multi-track	200 (W)	V = 1000 mm/s	90 (μm)	-
Multi-layer	200 (W)	V = 1000 mm/s	90 (μm)	40 (μm)

It should be noted that all of the metallurgical analysis is exactly followed by the same procedure described in section 3.2 from the previous chapter. A TESCAN VEGA3 SEM was used to study the microstructure deposited in single-tracks. Electron backscattering diffraction (EBSD) analysis was performed using a JEOL7000F SEM equipped with an Oxford EBSD detector to investigate the grain structure of the fabricated parts. Data collection during the EBSD analysis was performed using AZtecHKL and post-processing for data analysis was performed with HKL Channel 5.

4.4 Result and discussion

To evaluate the accuracy of the model, the current study focuses on three divided sections of single track, track-track, and successive layer simulation. In a single-track simulation, many simulation parameters have been tuned to get the closest simulated result compared to the experiment. In the next step, the model is applied to the track-track and successive layer condition and then simulated results compared to the observed microstructure from the experiment.

4.4.1 Single melt pool simulation

Applying the model to an actual melt pool requires three important inputs that are essential for the initial condition: melt pool geometry, grains at fusion boundary, and temperature. The initial melt pool geometry has been detected from an SEM image of an etched cross-section (Figure 42 (a)). Grains at the fusion boundary are identified from EBSD analysis and their corresponding orientation (easy growth directions) were double-checked with the cellular direction in the SEM image (Figure 42 (b)). Combining the grain orientation and melt pool geometry results in an image similar to Figure 42 (c) in which green color shows the orientation of grains. To obtain the temperature field prior to the solidification, we use the heat source model where simulated melt pool dimensions (width and depth) are comparable to the actual melt pool and the difference in melt pool geometry is negligible (Figure 42 (d)). Superimposing the obtained temperature field to melt pool geometry and grain orientation sets the initial condition where the intensity of blue color in Figure 42 (e) represents the intensity in $\tilde{T}$.

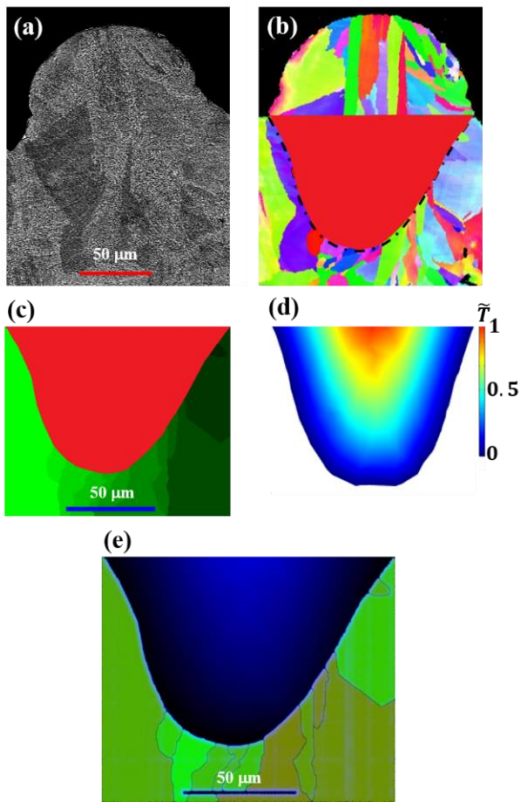

Figure 42. (a) SE-SEM micrograph of a single track cross-section, (b) EBSD image of the single track with extracted melt pool area, (c) post-processed imaged showing grains in green and melt pool in red color, (d) Simulated temperature gradient, and (e) processed image showing initial condition for solidification simulation.

Figure 43 shows the simulation result in (a) and the actual orientation map in (b). Since the original location and a time step of new grains are unknown, it is decided to remove the nucleation module for this part. In this regard, comparing the growth process of primary grains at the fusion boundary can represent the accuracy of the model. Competitive growth showed by circles in Figure 43 where both simulation and experimental results agree to have blocked grains at the depth of the melt pool due to their undesirable easy growth orientation. On the other hand, results reveal that grains may change the preferred growth direction based on the instantaneous temperature gradient. For example, Figure 43 (a, b) shows a grain that changes its growth direction (white color arrows) from horizontal to vertical direction. As it is shown, the phase-field model is capable of predicting the blocking mechanism during the competitive growth. Therefore, it may be possible to predict whole grain structure after the LPBF process.

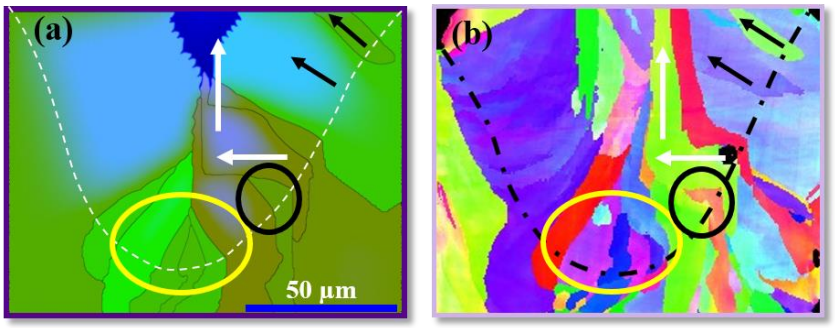

Figure 43. Melt pool solidification results from the simulation in (a) and experiment (EBSD inverse pole figure map) in (b).

4.4.2 Multi-track simulation

Since LPBF parts consist of successive layers that are made of single track series, it is important to examine the accuracy of the model in multi-track solidification condition. In this regard, multi-track deposition is done experimentally and compared to the simulated one with the same process condition. Figure 44 shows the melt pool trajectories, EBSD image, and simulated microstructure of a single layer which consists of seven multi-track depositions. Results show the existence of side branching in both experiment and simulation. Grains at the intersection of two adjacent single tracks have the opportunity of growing aligned with two different thermal gradient directions. This can activate two different easy growth crystallographic directions and results in side-branching of grain (white arrows in Figure 44 (b, c)). A colony of nucleated grains parallel to the building

direction exists mostly in the middle of some melt pools (black ovals in Figure 44 (b, c)). New grains, which are nucleated close to the fusion boundary, either is blocked by other epitaxial grains or block the other grains and become columnar grains. However, nucleated grains in the middle of the melt pool are mostly surrounded by survived columnar grains and have space for growth. In this situation, once several nucleation sites happen in the middle of a melt pool a colony of small grains will be created in the microstructure. On the other hand, some slender grains exist in the middle of a course columnar grain (yellow ovals in Figure 44 (b, c)). This is mostly a result of nucleation with an undesirable crystallographic orientation (with respect to the local thermal gradient) which happens in the path of epitaxial growth. In this regard, the previous grain with a preferred growth direction will interrupt the growth of the new grain and forms a slender grain embedded in a columnar grain.

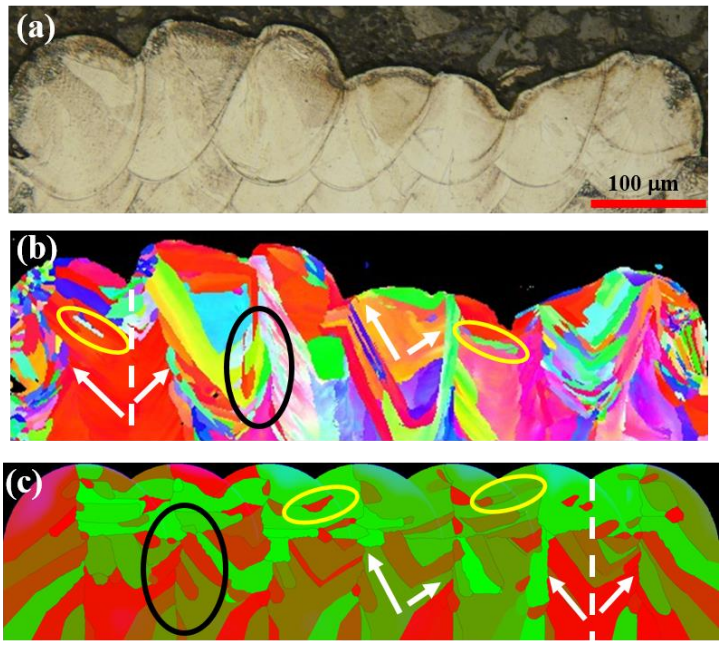

Figure 44. The single-layer consists of seven-track deposition shows: (a) melt-pool trajectories, (b) actual grain structure, and (c) simulated grain structure.

4.4.3 Multi-Layer simulation

Since the LPBF microstructure is an outcome of multi-layer depositions of tracks, it is important to investigate the accuracy of the model in a layer by layer solidification process. Figure 45 shows

the experimental and simulation results of 7 layers of melt pool solidifications. In both conditions, the number of tracks in each layer is also set to seven. The melt pool geometry and its initial temperature gradient is simulated from the previous COMSOL simulation and used in the multi-layer simulation.

Similar to multi-track solidification, the existence of grain side-branching is confirmed by both experimental and simulation results (yellow-colored arrows in Figure 45). While the frequency of side-branching is more in the early layers, their existence is not limited to a particular number of layers. In fact, side-branching may happen in between tracks whenever the columnar grain growth is interrupted by the growth of a new grain that has preferred growth directions along with solid-liquid temperature gradients in two different adjacent tracks.

Side grain structures are considerably finer than the core structure due to the significant contribution of surrounding powder particles in the nucleation process. This feature is also in good agreement between simulation and experimental results showed in Figure 45 where small grains converging toward the core material (transparent white ovals in Figure 45 (a-b)). On the other hand, columnar grains form in the middle area apart from the side fine grain structure. While side grains grow toward the core material, columnar grains grow upward and compete with new grains to survive.

It is important to predict the transition thickness between short-ranged grains and elongated columnar grains. This helps to understand how soon the columnar grain forms on top of a random structure like powder particles or any other randomly oriented structure (base metal). Figure 45 shows that the formation of the elongated columnar grains starts from ~102-150 μm in the experiment which is very close to the simulation results (~96-140 μm). The width of columnar grains is another characteristic that can be set as a probe to be examined. In this regard, a variation in the width of columnar grains has been observed in both simulation and experiment. Grain's width is mainly depending on the surrounding grain environment that a particular columnar grain is growing, therefore, as a result of the random orientation of surrounding grains the columnar grain's width may vary. The width of columnar grains measured between 80-91μm and 79-102 μm in experimental and simulation results, respectively. Interestingly, few grains were observed to grow in between columnar grains and form a continuous slender morphology with a width size of less than 15 μm (showed by white arrows in Figure 45 (a, b)). Closer examination of the

formation of the slender grain during simulation revealed that they are exactly located at the middle of the melt pools whereas temperature gradient direction is always upward (straight vertical) without changing its direction during the whole solidification process. As a result, when a grain with a <100> direction aligned with vertical direction meets the middle of the melt pool, it can continuously compete with any other grain and survive in a narrow region during the competitive growth process.

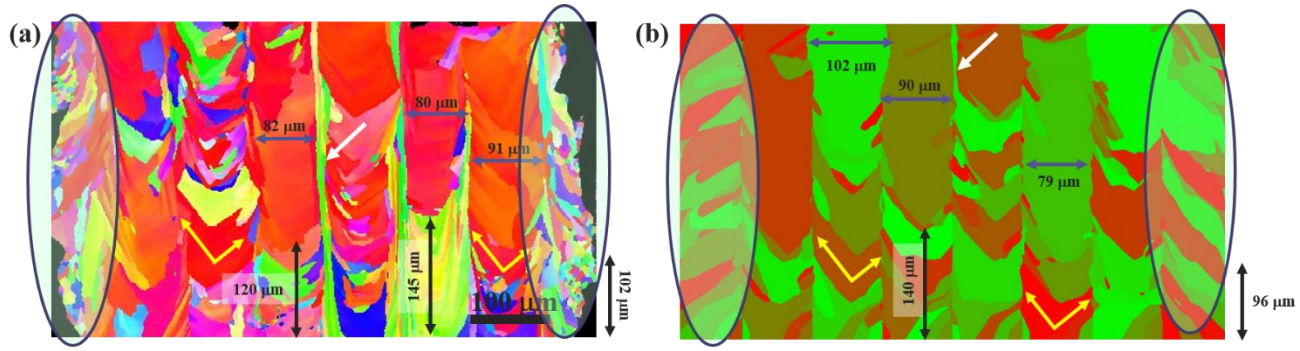

Figure 45. The grain structure of seven-layer depositions: (a) Experimental results, (b) Simulation result.

4.4.4 Sensitivity analysis

The sensitivity analysis is used in this section to ensure that the capability of the method is beyond the use of current material and it can be used for different materials with different parameters. It is also important to check if the model responds correctly with respect to the variable physical coefficient. To do this, here, we focus on two of the most important phase-field parameters ($\bar{\varepsilon}$ and ω) which directly impact the anisotropy in the growth of crystals and competitive grain growth. The sensitivity analysis performed to see whether $\bar{\varepsilon}$ and ω correctly fulfill their physical role in the model and how their variations impact the model prediction. Sensitivity analysis simulations involve variation in one parameter while other parameters are kept constant.

Before investigating the influence of $\bar{\varepsilon}$ and ω constants in the model, it is helpful to understand their physical role in the model. Melt pool solidification of LPBF involves epitaxial grain growth where the moving interface (solid/liquid interface) contains cellular/dendritic structure aligned with a particular direction that grows faster than the other directions (Figure 46 (a)). The strength of the anisotropy coefficient (ω) represents the mobility of the interface in a particular direction (<100> crystallographic direction in an FCC crystal) with respect to any other direction. As a result, increasing the ω value should result in relatively faster crystal growth (in easy growth

directions) and longer cellular morphology (along with <100> directions) in comparison with smaller ω values (Figure 46 (b)). On the other hand, $\bar{\varepsilon}$ coefficient fulfill a different purpose. As it is mentioned, a dendritic/cellular morphology forms the liquid/solid interface at microscales, while a semi-solid interface forms in atomic-scale where atoms constantly being added to and removed from this intermediate layer (Figure 46 (c)). In the case of solidification, the rate of incoming atoms to this layer is higher than ejected atoms and as a result, the interface moves from the solid toward the liquid. It should be noted that both $\bar{\varepsilon}$ and ω are influencing the mobility of the moving interface. Increasing the ω coefficient should not change the average ε in all directions, but giving more weight to those growth directions closer to the <100> crystallographic direction. However, changing the $\bar{\varepsilon}$ coefficient alters the average semi-solid interface thickness (ε) while keeping the ratio between all directions constant.

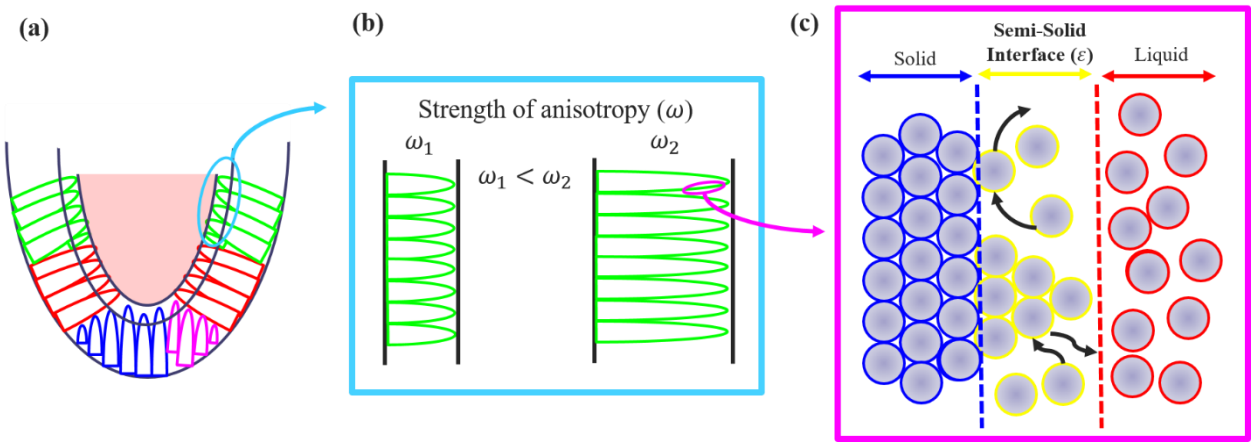

Figure 46. Schematic of solidification in a single melt pool showing (a) competitive grain growth (b) effect of strength of anisotropy (ω) coefficient (c) Semi-solid interface (ε) in an atomic scale.

4.4.4.1 Strength of anisotropy

Figure 47 shows the simulated microstructure with the strength of the anisotropy coefficient (ω) of 0.02 and 0.05. It is observed that with a lower ω value grain boundaries appears as straight lines while increasing the ω value results in curved shape grain boundaries. The crystal growth of grains in a single melt pool is shown at higher magnification images on the right side of each microstructure. It is observed that decreasing the ω value significantly decrease the length of the cells at the solid/liquid interface when a 60% decrease in ω value results in ~42% reduction in cells length at the interface. This means the ω parameter truly fulfils its physical role in the model. Interestingly, the overall crystallographic texture seems to be different from the altered ω value.

With ω value of 0.02, majority of grains are oriented at a 45˚ angle to the horizontal direction, however, at a higher value of ω (0.05), significant amount of columnar grains appears with 0˚ / 90˚ orientation. Increasing the ω parameter gives more wight to those grains which are aligned with the temperature gradient. With the current simulated temperature field distribution, crystallographic orientation will be dominated by cube texture when ω value is chosen to be 0.05 or higher. It should be noted that ω values higher than 0.1 resulted in a unrealistic microstructure (not a converging problem) since the strength of anisotropy cannot be higher than a particular value.

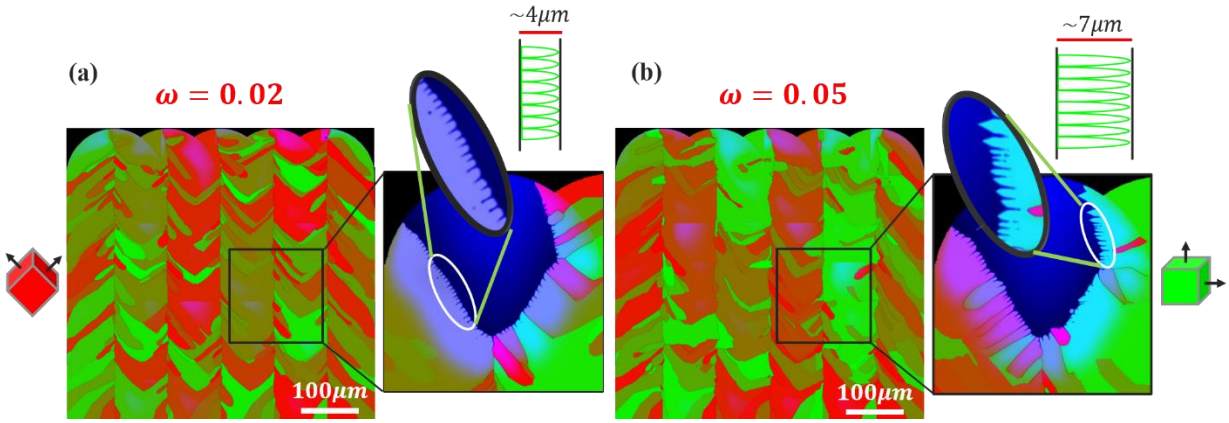

Figure 47. Simulated grain structure shows the difference in cell morphology and crystallographic orientation when ω constant is set to (a) 0.02 and (b) 0.05.

4.4.4.2 Semi-solid interface constant

Similar to ω coefficient, the interface thickness coefficient changes the anisotropy of the crystal growth, but in a different manner. Figure 48 (a-c) shows the changes in the microstructure when $\bar{\varepsilon}$ coefficient is changed from 5×10^{-3} to 1.5×10^{-2}. Increasing the $\bar{\varepsilon}$ value strengthens the anisotropic behavior of the crystal growth, therefore, increasing the surviving chance of grain with preferred orientation during the competitive grain growth. As a result, it is observed that the maximum length of columnar grains is ~110 μm, 227 μm, and 330 μm with $\bar{\varepsilon}$ value of 5×10^{-3}, 10^{-2}, and 1.5×10^{-2}, respectively. It is noteworthy to mention that the maximum length of grains is measured between 200-260 μm from experimental results.

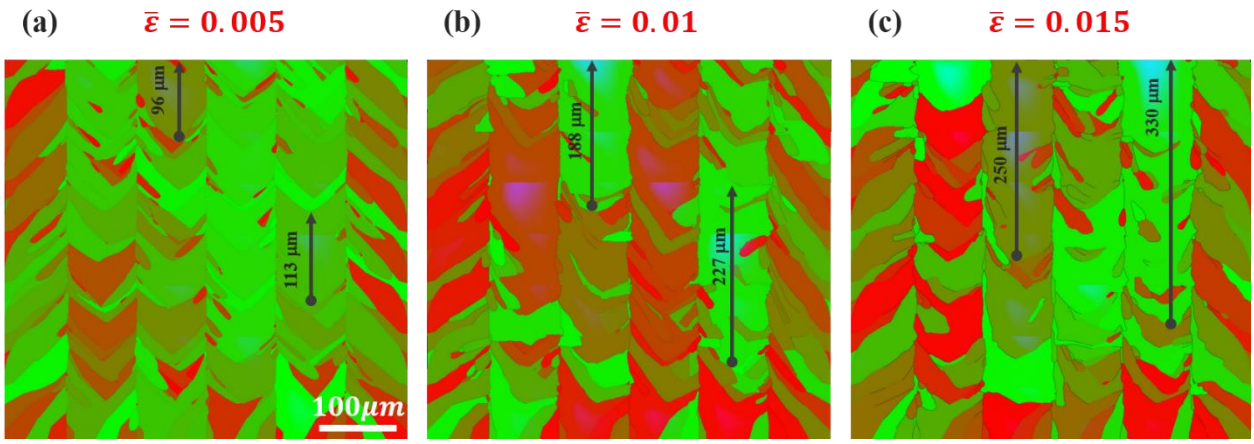

Figure 48. Simulated grain structure shows the difference in grain structure when the semi-solid interface dimensionless constant ($\bar{\varepsilon}$) varies between 0.005 to 0.015.

4.5 Conclusion

In the current study, a phase-field model is utilized to simulate the solidification process during LPBF. The simulated grain structure is validated with the corresponding experimental result. The predicted microstructure shows similar grain morphology and size when it is compared to the actual microstructure. Also, the solidification simulation brought a valuable insight into the formation of LPBF grain structure. Some of the most valuable understandings are briefly discussed here:

- It is possible to predict the crystal growth paths during LPBF melt pool solidification by just considering solidification anisotropy and melt pool temperature gradient. This is shown in single melt pool solidification when the phase-field initial condition is obtained from the experimental measurement and simulated solidified grain structure compared to the experimental result.
- Multi-track solidification simulation reveals the reason behind the formation of side-branching of gains. It is possible for grains, which are located in the vicinity of single track overlapped regions, to find the chance of growing in two different directions. As a result, two different easy growth directions (aligned with the normal direction of adjacent melt pool boundaries) will be activated that allows side-branching of grains.
- From the multi-track study, a colony of small grains was observed mostly in the middle of melt pools where the overlap region is not big enough to re-melt these features. These

grains are mostly elongated along with building direction and their existence is also observed in the actual EBSD results.

- The model shows a good accuracy in terms of predicting the formation of columnar grains. For example, multi-layer solidification simulation shows columnar grain formation after ~96-140 μm build-up when experimented microstructure (with the same process condition) shows ~100-150 μm transition thickness for columnar grain formation.
- The simulation is tested in terms of grain dimensions and shown to be accurate in grain dimensions prediction. For example, the width of simulated columnar grain measured between 79-102 μm when the experimental measurements from EBSD analysis show columnar grain's width between 80-91μm.
- Sensitivity analysis is performed to investigate the role of some important phase-field parameters in the LPBF grain structure formation. The strength of anisotropy is found to have a great impact on the dominant crystallographic texture. On the other hand, the change in semi-solid interface thickness results in significant variation in length of columnar grains (changing the maximum length of columnar grain from 113 μm to more than 330 μm).

5 Controlling mechanical properties of additively manufactured Hastelloy X by altering solidification pattern during laser powder-bed fusion

5.1 Introduction

Laser powder-bed fusion (LPBF) is one of the most well-known additive manufacturing (AM) techniques with more design freedom compared to conventional methods [96]. Since micro-size defects are detrimental to mechanical properties of as-built LPBF parts, the main process parameters (such as laser power [2,4], scanning velocity [5,97], hatch spacing [28,97], and layer thickness [28,51]) are mostly devoted to optimizing the level of porosity in printed parts. The laser scan strategy is one of the adjustable process parameters that can affect the solidification pattern but does not have a considerable effect on the density of the printed parts as the melt pool size and applied energy density are mostly related to the other process parameters. However, a poorly selected scanning strategy may create systematic pores [97,98]. In a defect-free as-built part, mechanical properties are mostly controlled by microstructure. Such an example can be found in [23,99,100] where alternating grain size, presence of a second phase, crystallographic texture, etc. were reported to affect the mechanical response of printed parts. Therefore, the laser scan strategy can be used in controlling the solidified microstructure of the fabricated part and the corresponding mechanical properties.

Current literature shows a variation in the mechanical properties of the same material due to a lack of knowledge in the as-built microstructure of printed LPBF parts [101–103]. For example, Inconel 718 LPBF parts from different works show an ultimate tensile strength between 1065 MPa and 1120 MPa [96,104]. Based on these results, it is believed that the microstructure of the as-built parts can be tuned using the appropriate set of process parameters to achieve the desired mechanical properties. Due to the different thermal histories obtained from different sets of process parameters, the as-built microstructure varies and consequently, the mechanical properties vary as well [101,105]. Generally, due to the low energy barrier for epitaxial growth in the LPBF process [20], grains at melt pool boundaries grow epitaxially along the preferred crystallographic direction (<100> direction in FCC crystals) which is also along the heat flow direction [15,24,106]. Hence, the competitive growth of grains is unavoidable where faster grains (with <100> crystallographic direction aligned with heat flow) interrupt slower grains during solidification [15,107]. Dominant crystallographic texture and columnar morphology observed in LPBF parts is the consequence of repeated laser scanning in a particular direction which results in the anisotropic mechanical behavior [108–110]. In this regard, post-processing such as heat treatment (HT) and hot isostatic pressing (HIP) can be used to alleviate the anisotropic behavior of as-build parts but increase the final product cost [46,109,111]. However, it is cost-efficient, if this anisotropic behavior can be controlled by changing the process parameters to avoid any post-processing.

Since material properties are highly dependant on the microstructure [112–114], grain refinement mechanisms can be used to improve the mechanical properties. In general, many grain refinement mechanisms have been proposed and applied successfully namely; mechanical, chemical, and thermal methods [112,114]. In the mechanical method, grains are subjected to refinement by electromagnetic or vibration stirring during solidification where both mechanical forces result in dendrite fragmentation and lead to higher nucleation rate and finer grain structure [114–116]. However, the need for additional equipment makes this undesirable [114]. Changing the overall composition for refining grain structure counts as a chemical method where their popularity is due to their low cost [117–119]. Such an example of the chemical method is adding inoculant to the system which results in considerably higher heterogeneous nucleation during solidification [113,117]. Refinement methods that control the temperature field of molten metal will be under the category of thermal methods. For example, extreme supercooling induced by high cooling rates during solidification is an example of thermal methods that can result in a columnar to equiaxed transition (CET) of grain structure [112,120]. CET has been shown to improve the mechanical behavior in directional solidification processes [112]. However, as CET is conducted during solidification, the application of CET to LPBF parts will be challenging as a strong heat flow along the building direction is inherent to the LPBF process.

Based on the discussion presented above, current works in literature do not offer a comprehensive agreement on the control of microstructure during the LPBF process. In this study, a laser scan strategy has been used to control the microstructure and the corresponding mechanical behavior of Hastelloy X LPBF parts. A new grain refinement mechanism under the category of thermal methods has been proposed to achieve a superior mechanical strength. It has been found that thermal history (made of heat flow directions in different successive layers) can control not only the crystallographic texture but also the grain size. Interpretation of tensile testing and Vickers hardness data for as-built LPBF samples is performed with a focus on the effect of microstructure on the primary mechanical behavior in different samples with respect to their building orientations. Results show that interruptive columnar grain growth mechanism can be introduced during solidification of stripe rotational scanning strategy in which higher tensile strength is due to its finer microstructure compared to the other scan patterns. On the other hand, a large grain structure with a strong Goss texture obtained from a unidirectional scan strategy results in the lowest tensile strength and hardness. Moreover, horizontal (ND/TD) planar anisotropy in tensile behavior with unidirectional scan strategy is correlated to the difference in the crystallographic orientation of grains with respect to the loading direction. The anisotropic tensile behavior of LPBF parts (from vertical (BD) to horizontal (TD/ND) direction) seems to alleviate once the average aspect ratio of the columnar grains is closer to one.

5.2 Experimental methods

A commercially available Hastelloy X gas-atomized powder, (Table 4), from EOS GmbH, was used in this study with D10, D50, and D90 of 15.5 µm, 29.3 µm, and 46.4 µm, respectively. The average powder size of Hastelloy X has been measured around 30 µm. Figure 49 depicted from utilized Hastelloy x powder where most of the particles are spherical. The inset picture is the magnified image of a spherical particle with some attached satellites to the surface. An EOS M290 (equipped with a Ytterbium fiber) was employed to print the laser powder-bed fusion Hastelloy X samples with different scanning strategies but identical process parameters (scanning velocity of 1250 mm/s, laser power of 250 W, a layer thickness of 40 µm, and hatch spacing of 80 µm). Four different scanning strategies were used and are referred to as; a) Uni-paths (Stripe Uni), b) chessboard rotational (Chess Rot) c) XY raster (Stripe XY), and d) rotational (Stripe Rot) (Figure 50a-d). It should be noted that the Stripe XY performs a 90˚ rotation in the laser path after each scan whereas Stripe Rot and Chess Rot perform a 67˚ rotation in the laser path. It should be noted that 67˚ rotation makes the highest randomness in scanning direction during different deposition layers.

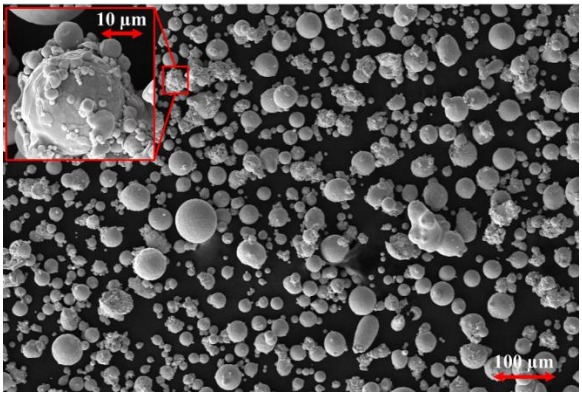

Figure 49. SEM image of Hastelloy X powder metal.

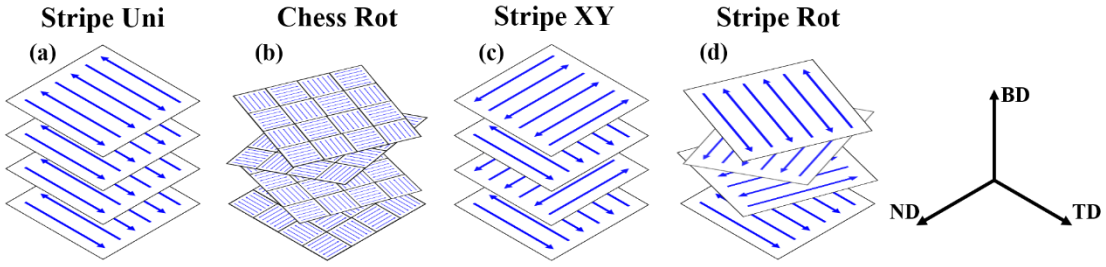

Figure 50. Schematic representation of four different scan strategies of (a) Stripe Uni without any rotation and bidirectional, (b) Chess Rot with squares of $\boldsymbol{2mm \times 2mm}$ *and 67˚ rotation, (c) Stripe XY with 90˚ rotation, and (d) Stripe Rot with 67˚ rotation between layers. Also, three different reference directions of BD, ND, and TD has been shown.*

Table 8. Nominal composition (in wt.%) of Hastelloy X gas-atomized powder used for selective laser melting process[42].

Ti	Al	Cu	Mn	Si	C	Co	W	Mo	Fe	Cr	Ni

<0.15	<0.5	<0.5	<1	<1	<0.1	1.5 ± 1	0.6 ± 0.4	9 ± 1	18.5 ± 1.5	21.75 ± 1.25	balance

Tensile tests were performed according to ASTM E8 standard [121] in the displacement control mode at the rate of 0.45 mm/min. Tensile samples (Figure 51b) with three repetitions were also printed with the different scanning strategies and are identified as building direction (BD), transverse direction (TD), and normal direction (ND) where BD is parallel to the building direction of the printed part, TD is parallel to the recoater moving direction, and ND is perpendicular to the recoater moving direction (Figure 51a). All tensile samples were built successfully except the Stripe Uni and Chess Rot BD samples that were canceled due to recoater impact. An Instron 8872 servo-hydraulic frame with a load capacity of ±25 kN was used for testing the samples under uniaxial tensile loading while a Wolpert Wilson 402 MVD micro Vickers hardness tester was used (500 g force with 10 s dwell time) to measure the hardness in ND, TD, and BD cross-sections.

Cubes with dimensions of 1 cm × 1 cm × 1 cm and faces perpendicular to the TD, ND, and BD were also printed with different scanning strategies for microstructure characterization (Figure 51a). The melt pool observations for printed cubes were performed using a Keyence VK-X250 confocal laser microscope. While a JEOL7000F scanning electron microscope (SEM) equipped with an Oxford EBSD detector was used to perform the electron backscatter diffraction (EBSD) analysis. AZtecHKL was used for data collection during the EBSD analysis and all post-processing for data analysis was performed with HKL CHANNEL 5.

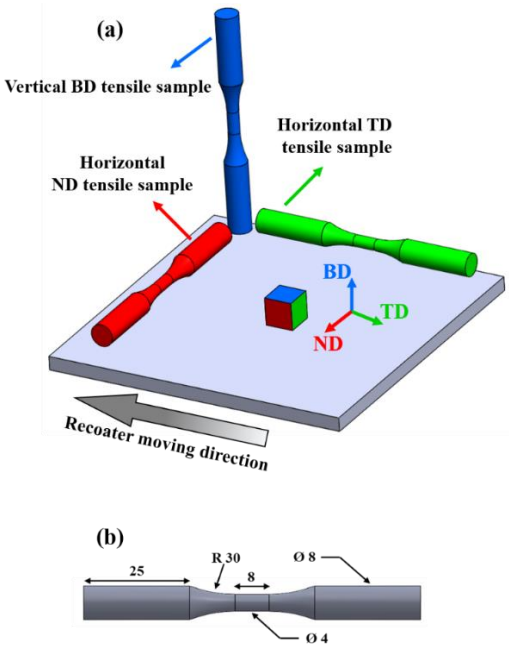

Figure 51. (a) Schematic representation of tensile and cube samples orientation on the build plate. Nomenclature of reference directions for mechanical and microstructural analysis is shown as well. (b) Tensile specimen geometry with dimensions in mm.

5.3 Results and discussions

5.3.1 Microstructure

Figure 52a-d represents the inverse pole figure (IPF) maps for the BD, TD, and ND cross-sections from the Stripe Uni, Chess Rot, Stripe XY, and Rot samples, respectively. Results in Figure 52 a–d highlight the differences observed in the crystallographic orientation of crystals from different directions.

Stripe Uni (Figure 52b) samples exhibit a near single crystal microstructure with a few equiaxed grains visible from the top surface. It should be mentioned that TD cross-sections show the presence of other orientations. The effect of the presence of these orientations will be investigated by the corresponding pole figures. The {110} texture observed in the ND and BD planes for the Stripe Uni sample is due to the 45˚ alignment of two <100> crystallographic directions with BD. Similarly, a {100} texture observed in the TD plane is due to the alignment of the other <100> direction with TD. It should be mentioned that TD is also the laser scanning direction in Stripe Uni samples.

The Stripe XY sample shows columnar grains aligned with BD where a weak Cube texture is observed (Figure 52c). The {100} texture observed in all TD, BD and ND cross-sections is due to the <100> crystallographic directions aligned with reference directions (TD/BD/TD). In the Stripe XY case, the laser track switches between TD and ND, and therefore, a clear demarcation in grain morphology due to laser scan path can be observed in these samples. The presence of a finer grain morphology observed in the BD cross-section might be due to the columnar grain growth and will be discussed later.

The EBSD map from the Chess and Stripe Rot samples show a much finer grain morphology with random orientation of crystals in the microstructure. However, the Stripe Rot samples show fine structures for ND, TD, and BD while Chess Rot samples do not show uniform structures in all cross-sections. Finer grain morphology in the Stripe Rot samples (compared to scanning strategies) is probably due to the interruptive competitive grain growth caused by the rotating laser irradiation path in these samples. As Chess Rot is an island scan strategy, different islands within the same layer undergo a 90˚ rotation. Combined with the 67˚ rotation between different layers, this 90˚ island rotation results in an overall rotation of 157˚. Compared to the 67˚ rotation in the Stripe Rot

samples, this 157˚ rotation observed in the Chess Rot samples reduces the randomness in heat flow directions and hence results in a reduction of grain refinement. The observed TD cross-section results from the Chess Rot (Figure 52b) could be from the island overlap regions where the laser scanning of neighboring islands results in a double re-melting. The presence of the large grains in this cross-section shows the probable effect of the laser re-melting.

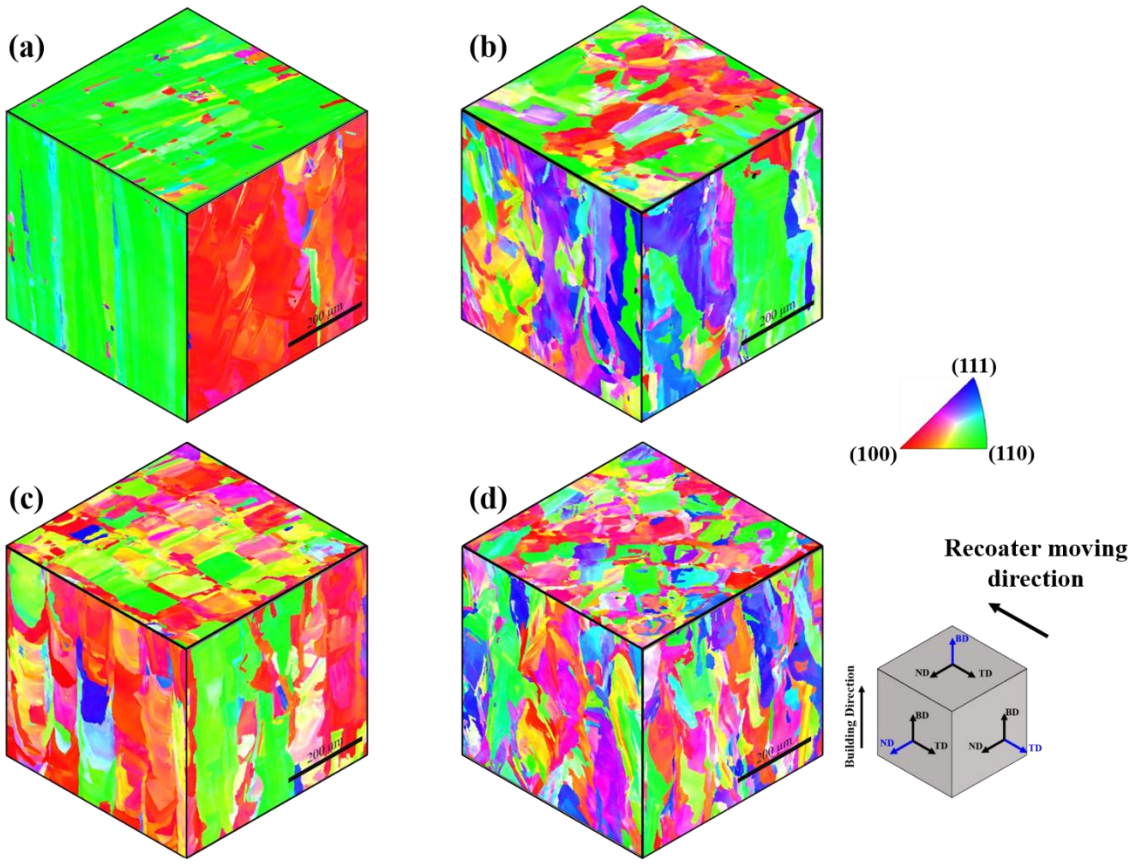

Figure 52. 3D visualization of the microstructure of LPBF samples with a) Stripe Uni, b) Chess Rot, c) Stripe XY, and d) Stripe Rot scan strategy. The reference direction for each graph is normal to the cross-section.

Figure 53 represents the {100} pole-figures of ND, TD, and BD cross-sections from the Stripe Uni, Chess Rot, Stripe XY, and Stripe Rot samples, respectively. Similar to the EBSD results, pole-figures reveal that the strongest crystallographic texture is related to the Stripe Uni sample where BD and ND cross-sections show the same orientation. The maximum of Multiples of Random Distribution (MRD) obtained from pole-figures of samples other than Stripe Uni is approximately between 5 to 9 while Stripe Uni sample shows at least maximum MRD of 20 from all cross-sections. This strong crystallographic texture in the Stripe Uni sample is due to repetitive heat flow patterns created in successive layers which is discussed more in-depth in the future. A

small variation in crystallographic orientations observed in these pole-figures of the Stripe Uni sample can be attributed to the presence of planes other than the {110} as observed in Figure 52a.

The pole-figure from the Stripe XY sample shows a weak Cube texture in which hints at a possibility of a number of {100} planes that are always perpendicular to the ND, TD, and BD cross-sections. Similar to the {100} texture observed in the TD cross-section of Stripe Uni samples, in Stripe XY, as laser scanning direction is switching between ND and TD, {100} texture is observed in both the TD and ND cross-sections. As a result, the other <100> crystallographic orientations will form in the BD cross-sections as observed in EBSD results (Figure 52c). It should be noted that the presence of a rotated <100> orientation observed in the BD cross-section can be due to the sample preparation.

Stripe Rot sample (Figure 53) shows almost random orientation distribution in pole-figure from ND and TD cross-sections. Interestingly, BD cross-section shows a very weak texture of {100} planes. Compared to all other pole-figure contours, Stripe Rot is observed to have the most randomly distributed crystallographic orientation. As it is shown in Figure 53, compared to other samples, the Stripe Rot sample has the maximum MRD of ~5 while other samples have a maximum MRD of more than 7 in different cross-sections. Also, The Chess Rot sample (Figure 53) shows a random crystallographic orientation in ND cross-section while TD and BD cross-sections show weak {110} textures. As it is mentioned before, in the Chess Rot scan strategy, the re-melting and solidification regime is different due to the presence of islands. Therefore, abnormal grain growth may happen in areas with double laser scans. As a result, large grains are observed in the microstructure and therefore result in higher intensity in localized regions (Figure 52b).

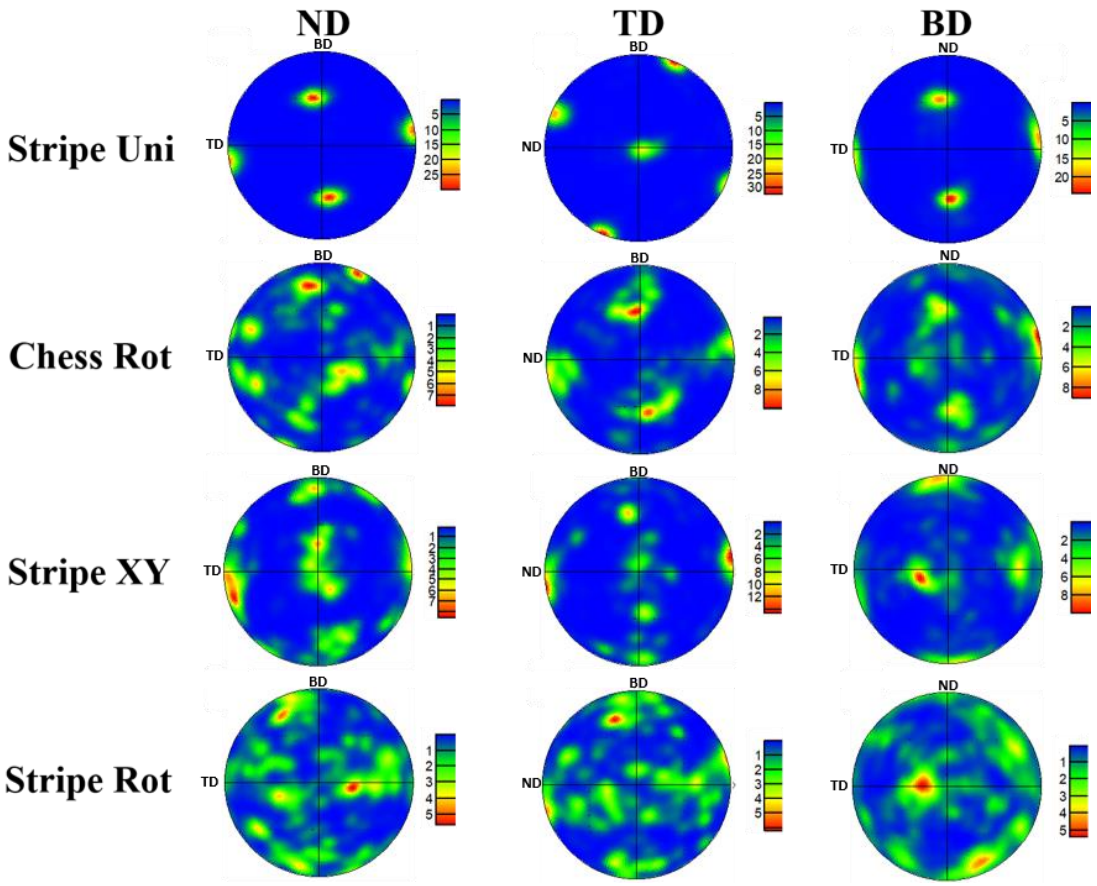

Figure 53. {100} Pole-figure contouring displayed from ND, TD, BD cross-sections of Stripe Uni, Chess Rot, Stripe XY, and Stripe Rot scan strategies.

Different grain morphologies and crystallographic textures can be produced with different solidification patterns caused by varying laser scanning strategies (as observed in Figure 52). It is important to pay attention to the heat flow generated with respect to the applied laser scan strategy to understand the differences observed in these samples. In this regard, Figure 54a-b shows the BD, ND, and TD etched cross-sections from the Stripe Uni, Chess Rot, Stripe XY, and Stripe Rot samples, respectively.

It is well known from the solidification of FCC crystals that <100> is the fastest growth crystallographic direction [15,95]. Since heat flow direction is mainly toward previously deposited layer, dendritic or cellular microstructure is formed in the direction opposite to the heat flow at the beginning of solidification. This heat flow is perpendicular to the solid-liquid interface which is a direction perpendicular to the melt pool boundary [106]. Similar to what is described in the literature for FCC materials fabricated with LPBF and unidirectional scanning strategy [66,106],

for the first track deposition in Stripe Uni scan strategy, the primary dendrites grow along the +45˚with BD. Next, as the laser scans the adjacent track, a partial re-melting followed by crystal growth of the previously solidified microstructure occurs. The overlapped region contains symmetric heat flow direction and the crystals grow in the -45˚with BD to have its second branch of dendrites parallel to the heat flow direction and perpendicular to its primary growth direction (Figure 54a). Since the preferred growth direction in each layer is the same in the Stripe Uni samples, the grain growth in subsequent layer depositions in this sample interrupts any random nuclei to grow because of their slower growth rates.

On the other hand, the Stripe Rot scanning strategy shows a different heat flow pattern. Due to the 67˚ laser scanning rotation in the Stripe Rot samples, the heat flow directions also alter in subsequent layers. Hence, partially melted powders (PMPs) that are originated either from powder bed or spatter powder [54,95] with random orientations, which matches the preferred growth direction to the heat flow, will probably grow and interrupt the other grains from growing. As a result, a higher number of grains participate in the competitive growth, and therefore, a much finer grain structure is observed in the Stripe Rot samples. More details on the grain size are discussed in Section 3.2.1.

As it is observed from Figure 54c, the Stripe XY scan strategy results in the typical parabolic shape of melt pools in the TD and ND cross-sections in every other layer. As a result of 90˚ rotation in scanning direction between successive layers, every other layer has a repeated melt pools cross-section in any fixed reference plane (which are TD/ND here). On the other hand, Chess Rot (Figure 54b) melt pools show arbitrary melt pools in different directions (similar to what is observed from the Strip Rot sample).

Based on the results from EBSD, pole figures and optical micrographs, there might be a relationship between crystallographic textures and observed melt pool patterns. The irregularity in the melt pool shapes caused by different scanning strategies results in different heat flow directions producing different microstructures. This difference should affect the mechanical properties of printed parts with these scanning strategies. However, as grain size plays an important role in defining the mechanical properties [112–114], it is important to analyze the corresponding grain size for these scanning strategies. In addition, based on the observed microstructures, there might

be an anisotropic mechanical response dependant on the scanning strategies. This difference can be explained as textural and morphological anisotropy. Textural anisotropy is caused by dominant grain orientation in microstructure, while the morphological anisotropy is due to variation in grain's aspect ratio [15,69].

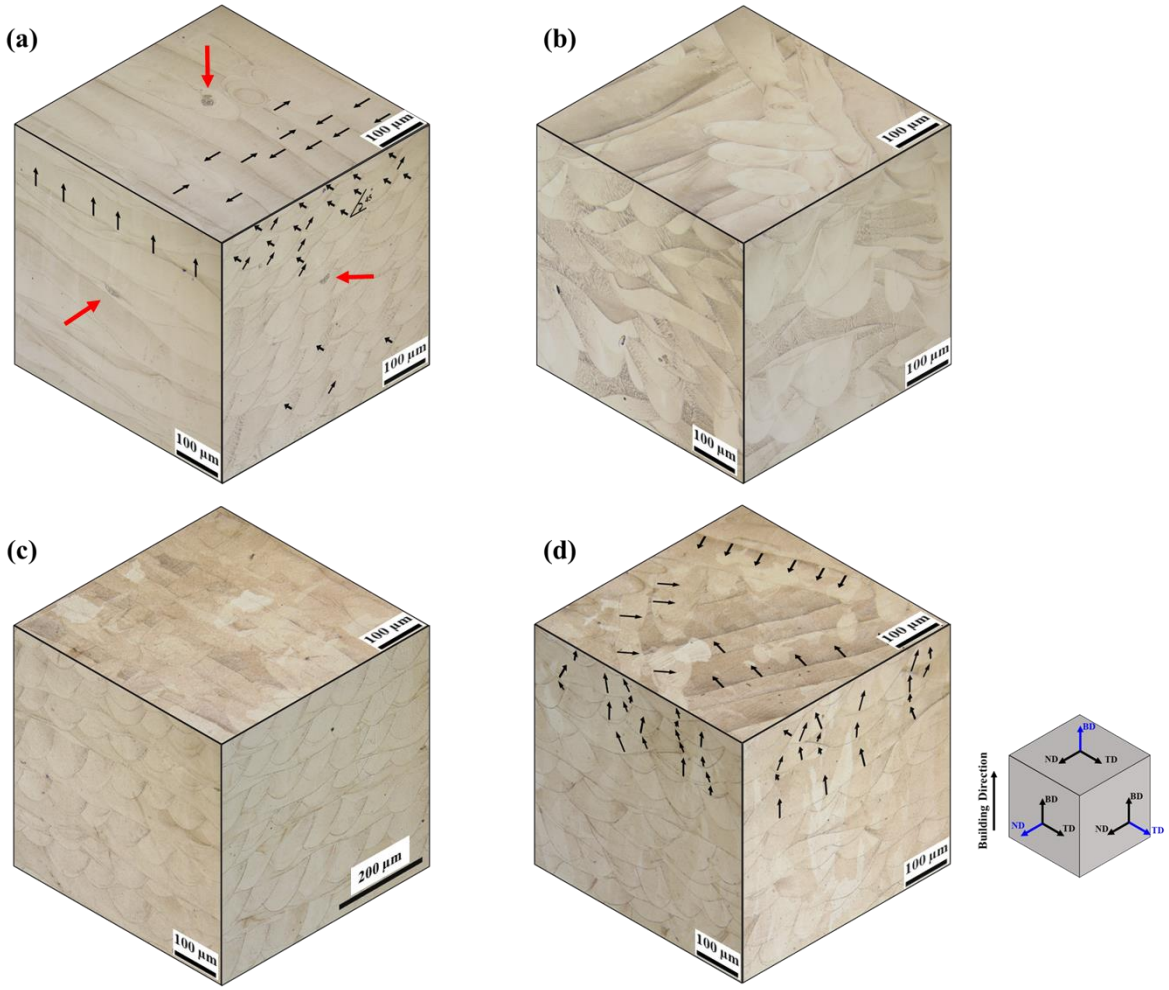

Figure 54. 3D melt pool visualization of a) Stripe Uni, b) Chess Rot, c) Stripe XY, and d) Stripe Rot scan strategy. Black arrows are representative of the main preferred growth directions in individual melt pools. Note: black arrows highlight the direction perpendicular to the melt pool boundary while red arrows point out some partially melted particles (PMP) in the microstructure.

5.3.1.1 Grain size and morphology

To evaluate the effect of scanning strategy on the grain size of as-built microstructure, equivalent circle diameter (ECD) of grains from the ND, TD, and BD cross-sections of Stripe Uni, Chess Rot, Stripe XY, and Stripe Rot samples were calculated and are shown in Table 9. Stripe Uni samples show a maximum grain size of ~850 µm while Chess Rot, Stripe XY, and Stripe Rot show a

maximum grain size of 229 µm, 193 µm, and 102 µm, respectively. Results from Table 9 show the same ECD range for the ND and TD cross-sections of samples while the BD cross-sections show much finer grain size for all scan strategies.

Due to the possible effect of columnar microstructure on mechanical properties, it is important to investigate the width and length of grains observed in the printed samples. Table 9 also shows the respective average width and length of the observed grains. Analysis of EBSD results shows that the average length & width of columnar grains in Stripe Rot, Stripe XY, and Chess Rot scan strategies are about 112 µm & 33 µm, 136 µm & 56 µm, and 195 µm & 54 µm, respectively. This high aspect ratio of grains observed in the current study is a result of competitive grain growth and upward heat flow direction (close to BD) during the LPBF process.

Changing scan strategies also affects the ECD in different cross-sections (ND/TD/BD). Based on the selected scan strategy, the heat flow pattern alters from repetitive ordered (in Stripe Uni) to random (in Stripe Rot). Therefore, a higher number of participated grain orientations during competitive grain growth would be expected from the randomized heat flow pattern. Since heat flow direction is mainly toward the last deposited layer, grains grow upward and form a columnar structure. As a result, compared to the ND and TD cross-sections, ECD for BD cross-section shows finer grains. It should be mentioned that compared to the grain's length direction, higher grain boundary density can be observed along the grain's width (TD/ND) where much higher grain boundary density exists. This will probably result in an anisotropic mechanical response (TD/ND and BD).

Table 9. Average value ECD, width, and length of grains in three different cross-sections of ND, TD, and BD for Stripe Uni, Chess Rot, Stripe XY, and Stripe Rot sample.

Scan strategy	ND			TD			BD		
	ECD (µm)	Width (µm)	Length (µm)	ECD (µm)	Width (µm)	Length (µm)	ECD (µm)	Width (µm)	Length (µm)
Stripe Uni	800	-	-	848	-	-	554	-	-
Chess Rot	188	54	195	229	69	224	131	54	116
Stripe XY	123	56	136	193	53	226	80	46	78
Stripe Rot	102	33	112	96	31	116	58	30	56

5.3.1.2 Textural anisotropy

In a textured polycrystalline material, Taylor factor (M) can describe the relative strength of a single crystal due to its orientation [122]. Grain orientation affects the Taylor factor in a specific direction as it is calculated from the sum of slips from different slip systems of the grain [123]. Dominant crystallographic orientation in polycrystalline material results in the activation of different slip systems in different sample directions. To investigate the effect of sample orientation and scanning strategy on the favorable orientation of crystal slip, Taylor factors were calculated from EBSD data where the {111}<110> was considered to be the preferred slip system for an FCC crystal.

Figure 55 displays Taylor Factor maps for Stripe Uni, Chess Rot, Stripe XY, and Stripe Rot samples from the ND, TD, and BD cross-sections. Stripe Uni sample shows the lowest average Taylor Factor in TD cross-section while ND and BD cross-sections show similar average Taylor factor values (~3.5). On the other hand, TD/ND/BD cross-sections show similar average Taylor factors for Chess Rot, Stipe XY, and Stripe Rot samples. An average Taylor factor of ~3 is observed for the Chess Rot and Stripe Rot samples while an average Taylor factor of ~2.75 is observed for the Stripe XY sample.

As mentioned earlier, the Taylor factor of individual crystals is completely dependant on the crystalographic orientation of grains with respect to the loading direction. The difference in the Taylor factors for TD/ND/BD cross-sections for the Stripe Uni sample is a result of the designed heat flow pattern and formed Goss texture in the microstructure. Since the ND/BD cross-sections show strong (110) textures (Figure 53), the observed average Taylor factor is also the same in these two cross-sections. On the other hand, the lowest average Taylor factor is observed in the TD cross-section as a dominant (100) texture is observed.

Similarly, the Stripe XY sample shows a weak (100) texture in TD/ND/BD which results in a lower Taylor factor compared to the Chess Rot and Stripe Rot scan strategies. As a result of irregular melt pool patterns observed in the Chess Rot and Stipe Rot scan strategies leads to a higher number of crystallographic orientations participating in competitive grain growth, a considerably higher average Taylor factor (~3) is obtained in these samples (Figure 55). Along

with the grain size, the Taylor factor affects the mechanical strength as it is related to the resistance of crystals to deform from applied loads. Results of grain size and Taylor factor from different scanning strategies suggests the possibility of varying mechanical properties from samples printed with different scanning strategies in different directions. Therefore, an in-depth study on the mechanical properties was conducted and is presented in the next section.

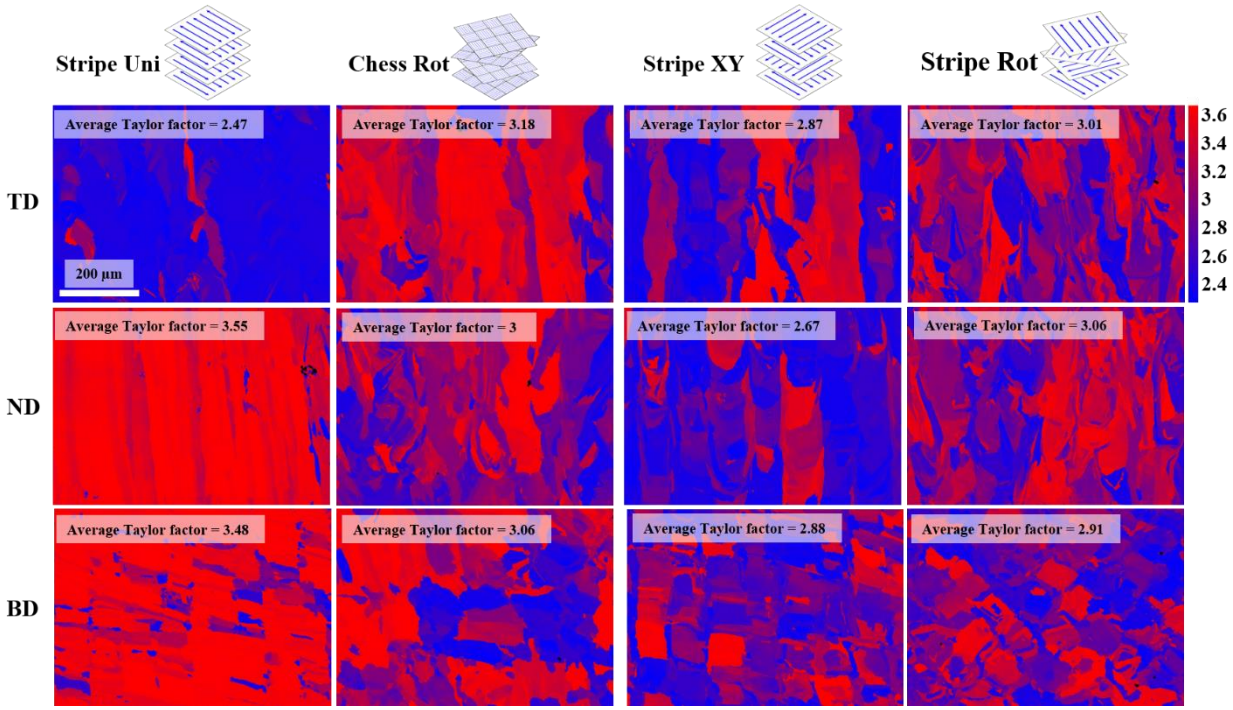

Figure 55. Taylor factor maps for Stripe Uni, Chess Rot, Stripe XY, and Stripe Rot samples from ND, TD, and BD cross-sections. Taylor factor maps are always aligned with the direction normal to the observed cross-section.

5.3.2 Tensile properties and hardness

To correlate the effect of microstructure evolution (grain size, grain morphology, and Taylor factor) on mechanical properties of printed samples, monotonic tensile and hardness tests were performed with different scanning strategies (Stripe Uni, Stripe XY, Chess Rot, and Stripe Rot) in different directions (BD, ND, TD). Figure 56a-d shows the yield strength (YS), ultimate tensile strength (UTS), failure strain, and Vickers hardness for the printed samples, respectively.

UTS results of samples printed in BD, TD, and ND show that the lowest UTS is observed in the BD direction for Stripe XY and Stripe Rot samples. Comparing the UTS from TD/ND samples shows that the lowest UTS was observed from the Stripe Uni sample along the TD direction (~727 MPa) while the highest UTS was observed in the Stripe Rot (~800 MPa) and Chess Rot (~820

MPa) samples. For rotation scanning strategies, such as Chess Rot, Stripe XY, and Stripe Rot, no significant difference in UTS and yield stress (YS) was observed in the ND and TD. However, compared to the TD Stripe Uni samples, ND Stripe Uni samples resulted in a higher average UTS (up to ~22 MPa) and YS (up to ~100 MPa). Comparing the UTS results of BD (vertical) Stripe XY and Stripe Rot samples to their TD/ND (horizontal) samples reveals that BD samples are about ~170 MPa and ~120 MPa lower than TD/ND samples, respectively.

Compared to BD, TD/ND samples with different scan strategies have almost the same average total elongation (from 39% to 46%). TD/ND Chess Rot, Stripe XY, and Stripe Rot samples show an average elongation of $40 \pm 3\%$, $43 \pm 5\%$, and $42 \pm 5\%$, respectively. Similar to the YS and UTS results shown in Figure 56 a & b, there is an insignificant variation in the total elongation from the TD/ND samples for any rotational scanning strategies (Figure 56c). A slight variation is observed from the Stripe Uni sample in which its TD sample has ~7% higher ductility on average compared to its ND direction. It is reported for LPBF parts that elongation can deviate as a result of a deviation in the crystallographic orientation of grains with respect to the loading direction [108]. It is also important to mention that all scan strategies are shown to be similar in terms of grain's morphology from ND and TD cross-sections (Figure 52), as a result, crystallographic texture can be responsible for different mechanical behavior of the material in different directions. The difference in ductility for the TD and ND Stripe Uni samples is probably due to different crystallographic orientations observed in the TD (dominant {100} planes) and ND (dominant {110} planes) cross-sections. In addition, due to the existing higher Taylor factor value in ND compared to TD, a higher resistance of the material to deform and hence results in lower ductility in ND Stripe Uni sample [96,124].

Results show that the BD samples from Stripe XY and Stripe Rot scanning strategies have ~14% higher elongation compared to the ND and TD samples. Due to large elongated grains observed in the ND/TD cross-sections, a lower number of grain boundaries are present normal to the ND/TD loading direction compared to BD loading direction. This has been reported to affect ductility [46]. This induces anisotropic behavior for ductility associated with columnar grain structure. Due to the fact that the average length (along with BD) of columnar grains is about 3-4 times greater than the average width (along with TD/ND) of the grains, the higher elongation from BD samples is expected.

Hardness results from ND and TD directions for Chess Rot, Stripe XY, and Stripe Rot samples show relatively similar values (190 HV - 200 HV). These observations are in agreement with other studies that show Vickers hardness does not differ with respect to the sample's orientation due to the consistency in cooling rate and similar cell size in different directions [46,64,96]. However, specifically for the Stripe Uni sample, hardness measurements from the BD cross-section has ~10 HV lower average value compared to the ND cross-section (Figure 56d). In addition, the average hardness value in the TD cross-section is slightly lower than the ND cross-section which is attributed to the strong Goss texture (Figure 53a).

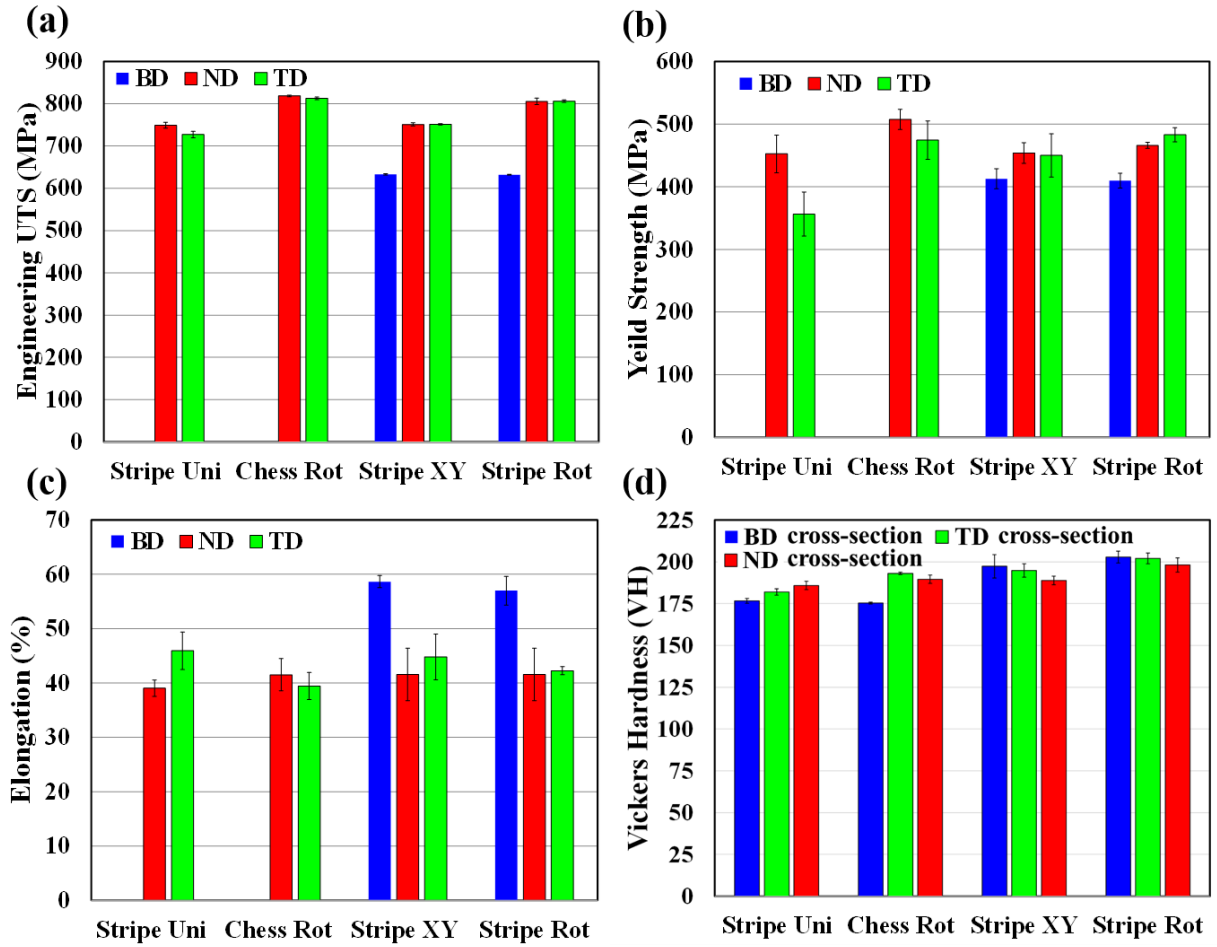

Figure 56. Bar plot of (a) UTS, (b) Yield Strength, (c) Elongation, and (d) Vickers hardness in three directions of BD, ND, and TD obtained from as-built samples with 4 different scan strategies of Stripe Uni, Chess Rot, Stripe XY, and Stripe Rot.

As mentioned previously, Stripe Rot and Stripe XY samples show an increase of ~170 MPa and ~120 MPa for the UTS of ND/TD samples. The increase in UTS observed in ND/TD samples can be explained due to the existence of a much finer grain structure along with the ND/TD compared

to BD (Table 9). The relative difference between the UTS of Stripe Rot and Stripe XY samples can also be attributed to the observed grain morphology.

Comparing the grain size in TD cross-sections of Stripe XY and Chess Rot sample shows similar ECD values of ~229 µm and ~193 µm, respectively. This results in a similar grain boundary density in both samples. However, YS and UTS of the TD Chess Rot sample are 24.3 MPa and 61.4 MPa higher than those of the TD Stripe XY sample (Figure 56 a, c). The Stripe XY scan strategy results in a weak Cube texture, while Chess Rot samples show almost random texture (Figure 53). Hence, the different mechanical response can be due to the different crystallographic texture in Stripe XY and Chess Rot samples (Figure 53). A similar trend is also observed for the Stripe Uni samples with similar ECD values but different yield strength between ND (~452 MPa) and TD (~356 MPa) samples.

To validate the significant effect of texture for TD Stripe XY & TD Chess Rot and ND & TD Stripe Uni samples, Taylor factor and yield strength ratios were calculated. If the texture has a significant effect on the yield strength of these samples, the samples should show a similar Taylor factor and yield strength ratios. Results show that the ratio of TD Taylor factor from Stripe XY to Chess Rot $\left(\frac{2.87}{3.18} = 0.9\right)$ is very close to the ratio of average yield strength $\left(\frac{450.2}{474.5} = 0.94\right)$. This correlation between Taylor factor values and yield strength is probably due to the comparable grain boundary density in Stripe XY and Chess Rot samples. Likewise, a similar Taylor factor $\left(\frac{2.68}{3.48} = 0.770\right)$ and yield strength ratios $\left(\frac{356.43}{452.56} = 0.787\right)$ are observed between the ND and TD Stripe Uni samples. It should be noted that the ratios are only valid for samples with comparable grain morphologies and the absence of second phases [96].

The discussion presented shows the importance of morphological and textural anisotropy produced on the mechanical properties during LPBF. Compared to texture, grain size and morphology show a higher influence on the mechanical properties of printed parts. However, for the same grain size in Stripe Uni TD/ND, the texture is shown to play a minor effect on the mechanical properties. Lastly, similarities between yield strength ratio and Taylor factor ratio show the significance of texture in the prediction of mechanical properties.

5.4 Conclusion

In this study, laser scan strategy has been used to control the competitive columnar grain growth and the corresponding mechanical behavior of Hastelloy X LPBF parts. Parts with different laser scanning strategies namely; Stripe Uni, Stripe XY, Stripe Rot, and Chess Rot were manufactured and characterized to study the effect of scanning strategy on the microstructure and mechanical properties of printed parts. The following conclusions can be drawn from the current study:

- As a result of increasing randomness in the heat flow direction, grain refinement happens and average grain size from ND/TD/BD cross-sections of Stripe Uni, Chess Rot, Stripe XY, and Stripe Rot samples were observed as ~734 µm, 182 µm, 132 µm, and 85 µm, respectively.
- In general, the columnar morphology of grains results in the lowest number of grain boundaries along the BD resulting in the highest total elongation and lowest UTS. For example, in the Stripe Rot sample, the grain size in TD was almost three times smaller than BD and therefore results in a higher UTS (~170 MPa) and lower total elongation (~14%). This mechanical anisotropy was also observed in the Stripe XY samples. Compared to BD, a higher UTS (~120MPa) was observed in the horizontal (TD/ND) direction.
- Repetitive heat flow directions in Stripe Uni scan strategy results in a strong Goss texture. Whereas, a 67° rotation in the solidification pattern (Stripe Rot) results in different heat flow direction in successive layers. As a result, the random orientation of grains is observed without a particular crystallographic texture in the microstructure (pole figures/EBSD).
- Strong Goss texture in Stripe Uni samples results in a planar anisotropic mechanical response. This is due to the change in average Taylor factor between ND (3.48) and TD (2.68) samples which results in lower yield strength (~100MPa) and higher elongation (~6%). In contrast, this planar anisotropy was not observed in the Stripe Rot and Stripe XY resulting in similar Taylor factors in ND/TD.
- In the absence of a difference in grain size and morphology, a good correlation is observed between the Taylor factor and yield strength ratios. For example, the average yield strength ratio (0.94) between the TD Stripe, XY and TD Chess Rot was similar to their corresponding Taylor factor ratio(0.9).

6 Static recrystallization impact on grain structure and mechanical properties of heat-treated Hastelloy X produced via laser powder-bed fusion

6.1 Introduction

Laser powder-bed fusion (LPBF) is a class of additive manufacturing (AM) used for fabricating parts with complex geometries. LPBF can be an alternative manufacturing technique for work hardenable materials (such as Hastelloy X) when the use of traditional subtractive manufacturing methods becomes challenging and more expensive to manufacture the final product [45]. However, this novel manufacturing technique has its own challenges that prevent it from becoming a widespread industrial manufacturing technique [54]. The layer by layer deposition in LPBF is followed by rapid heating and cooling cycles, which introduce heterogeneity in the microstructure, internal stresses, and mechanical anisotropy in the final parts [61,125]. The strong anisotropic mechanical response of LPBF parts can be undesirable from a design point of view and may restrict its extensive use for many applications [126].

The cause of anisotropy in mechanical behavior in LPBF parts is mostly attributed to the directionality of the thermal gradient, which is dependent on the geometry but mainly aligned with the building direction during the solidification of successive layers [21,127]. The anisotropic solidification behavior of crystalline metallic materials results in faster crystal growth in specific crystallographic directions known as easy growth directions. In the presence of a strong temperature gradient, growth occurs preferentially along the dominant easy growth direction that matches closest to the temperature gradient [15]. In this condition, epitaxial grain growth occurs, resulting in the formation of a columnar grain structure after solidification. Furthermore, due to the rapid directional solidification, a cellular sub-structure appears inside the grains, where cell-walls are aligned with the easy growth direction and enriched by dislocations [21,60]. A higher concentration of solute atoms (such as Mo, Cr, and Mn in Ni-based superalloys) and fine carbides and oxides have also been reported in the cell-walls [21,60,61]. This directionally-oriented microstructure may give rise to a strong anisotropic mechanical behavior. For example, in the IN718 alloy, a higher yield and ultimate tensile strength of the material were reported in the horizontal direction, while elongation was significantly greater in the building direction [96,111]. The same trend for anisotropic mechanical behavior has been reported for LPBF-made Hastelloy X [21,128,129], as well as a high dependency of Young's modulus to the loading direction [110]. The aforementioned findings from the literature reveal that anisotropy in LPBF parts is inevitable and may not be simply removed by altering manufacturing process parameters. In this case, post-heat-treatment processes such as solutionizing and hot isostatic pressing (HIP)

can be beneficial as they may change the microstructure and the corresponding mechanical properties of the part [21,111].

This study delves into the recrystallization of the grain structure after LPBF in order to homogenize the microstructure, relieve internal stresses, and reduce the level of anisotropy in mechanical behavior. In this regard, tensile Hastelloy X samples were printed horizontally and vertically and then post-heat-treated at the Hastelloy X solutionization temperature. A significant amount of the columnar as-built grain structures has been replaced by recrystallized equiaxed and strain-free grains. Recrystallized grains are enriched by coherent twin-boundaries without any preferred alignment when the as-built grains show low angle grain boundaries aligned with the building direction. Static recrystallization leads to isotropic yield strength and elongation behavior of parts after 8.5 hours of high-temperature heat-treatment. However, the small difference in ultimate tensile strength between heat-treated vertical and horizontal samples is attributed to the remaining as-built columnar grains.

6.2 Materials and Methods

6.2.1 Printing and Material

In the present study, an EOS M290 was utilized to produce tensile samples in vertical and horizontal directions with 3 repetitions (Figure 57). The Hastelloy X powder supplied by EOS was used with a D50 < 30 μm [127] and the nominal chemical composition shown in Table 4. All samples were printed with laser power of 195 W, hatch distance of 0.09 mm, layer thickness of 0.04 mm, laser scanning speeds of 850 mm/s and 1300 mm/s, and a 67˚rotation in laser scanning direction between successive layers [88]. During the printing process, the build plate temperature was kept at 80˚C. In addition, for deflection measurements, cantilevers were also printed on LPBF substrates with the geometry and dimensions shown in Figure 57(d).

Table 10. Nominal composition (in wt.%) of gas-atomized Hastelloy X powder used for LPBF in this study [42].

Ti	Al	Cu	Mn	Si	C	Co	W	Mo	Fe	Cr	Ni
<0.15	<0.5	<0.5	<1	<1	<0.1	1.5 ± 1	0.6 ± 0.4	9 ± 1	18.5 ± 1.5	21.75 ± 1.25	balance

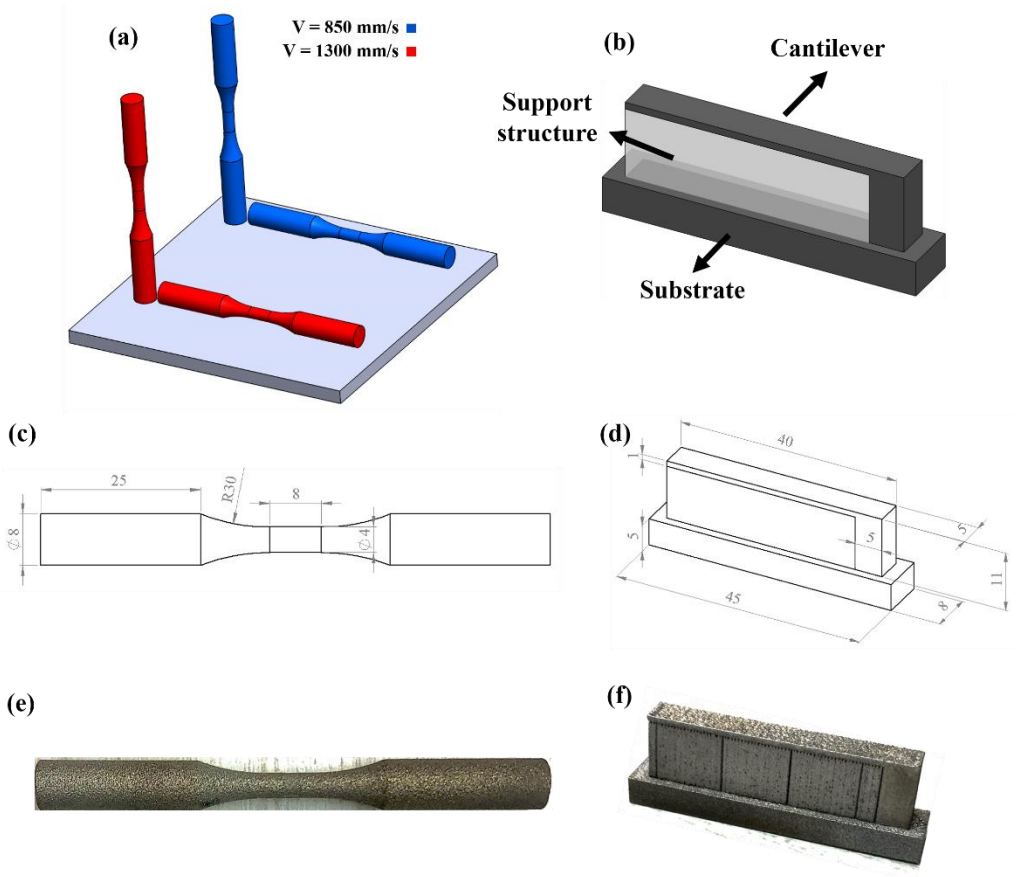

Figure 57. (a) Schematic representation of tensile sample orientations on the build plate. (b) 3D design of cantilever. Specimen geometry of (c) tensile samples and (d) cantilever samples with dimensions in mm. Also, a typical printed tensile sample and cantilever sample are shown in (e) and (f), respectively.

6.2.2 Heat-treatment process

High-temperature heat-treatments were performed on the tensile and cantilever samples. The LPBF Hastelloy X samples were placed in an alumina crucible and then heated up to 1177˚C (the solutionizing temperature for Hastelloy X [130]) in a horizontal quartz tube furnace under an ultra-high purity argon atmosphere. A ramp-up of 5 K/min and different holding times of 3, 6, and 8.5 hours were used followed by water quenching.

6.2.3 Material characterization techniques

A Keyence VK-X250 confocal laser microscope was utilized for microstructure observation after etching the polished cross-sections. For electron backscatter diffraction (EBSD) analysis, grinding (up to 2400 grit size) followed by vibratory polishing (Buehler VIBROMET 2) with a colloidal silica suspension was done. A JEOL7000F scanning electron microscope (SEM) equipped with an Oxford EBSD detector was used to

study the evolution of microstructure in heat-treated samples. In addition, AZtecHKL and HKL CHANNEL 5 software were used for EBSD data collection and analysis.

For transmission electron microscope (TEM) sample preparation, a Zeiss NVision40 equipped with a Gallium (Ga) focused-ion-beam (FIB) was used to selectively lift-out an $8\,\mu m \times 8\,\mu m$ area at grain boundaries and thin the sample down to ~100 nm. A Jeol 2010F TEM equipped with an Oxford EDS detector was used to observe dislocation structure and characterize second-phase particles during scanning transmission electron microscopy (STEM).

6.2.4 Mechanical Testing

An Instron 8872 servohydraulic machine with a load capacity of ±25 kN was used for quasi-static tensile testing under standard laboratory conditions. Tensile tests were performed according to ASTM E8 standard [121] in the displacement control mode at the rate of 0.45 mm/min. An Instron 2630-120 extensometer with an 8 mm gauge length and ±4 mm travel was used for strain measurement in quasi-static tests. Among the different annealing times, the longest heat-treatment time (8.5 hours) is selected for tensile testing of heat-treated samples.

6.2.5 3D Optical scanning and deflection measurement

An AICON SmartScan coordinate measuring machine (CMM) was used to capture the 3D data of the deflected parts. The 3D data was compared to the as-built STL files to calculate the overall deflection.

6.3 Results and Discussion

6.3.1 Microstructure

6.3.1.1 As-built microstructure and microstructure evolution during recrystallization

The recrystallization of metallic materials depends on the initial grain structure prior to heat treatment [131]. Esmaeilizadeh *et al.* [88] showed that laser scanning speed can be used as a key parameter to customize the as-built grain structure of LPBF parts. Therefore, to investigate the effect of the initial grain structure, two extreme laser scan speeds of the high-density region (1300 mm/s and 850 mm/s) are chosen to fabricate both coarse and fine grain structures before developing the heat-treated microstructure.

Optical micrographs of longitudinal cross-sections are displayed in Figure. 58. The sample printed with the higher scanning speed (1300 mm/s) shows some lack of fusion porosities (marked by blue arrows in Figure. 58(c)) and partially melted particles (marked by black arrows in Figure. 58(c)). However, these defects are not found in the sample produced with the lower scanning speed (850 mm/s). Moreover, in the

microstructure of the samples before heat-treatment (Figure. 58(a, c)), typical melt pools and corresponding boundaries can be observed, while after, no melt pool can be detected in the heat-treated samples, as shown in Figure. 58(b,d). In addition, the cellular structure did not appear after 3 hrs of annealing whereas annealing twins formed in the annealed samples (marked by red arrows in Figure. 58(b,d)).

With higher scanning speed the energy density is lower in comparison to that of lower scanning speed, resulting in narrower single tracks and smaller overlaps. As a result, the possibility of the formation of lack of fusion (LOF) defects and partially melted powders (PMPs) between melt pool tracks increases in samples produced with higher scanning speed [127]. In addition, due to the existence of a higher number of PMPs, the development of a finer grain structure is expected in samples manufactured with higher scanning speeds. The finer grain structure results in a higher density of grain boundaries, which may influence the number of potential nucleation sites during recrystallization.

Melt pool boundaries and cell walls are formed as a result of fast solidification, which includes a high dislocation density [60,61]. During the recovery process, the dislocation annihilation process is achieved by the cross-slip, glide, and climb of dislocations. This results in a new arrangement of dislocations in the crystal structure and diminution of dislocation content, leading to the complete disappearance of melt pool boundaries and cell walls. On the other hand, the occurrence of twinning in the microstructure can be attributed to the grain boundary migration and will be discussed in the next section.

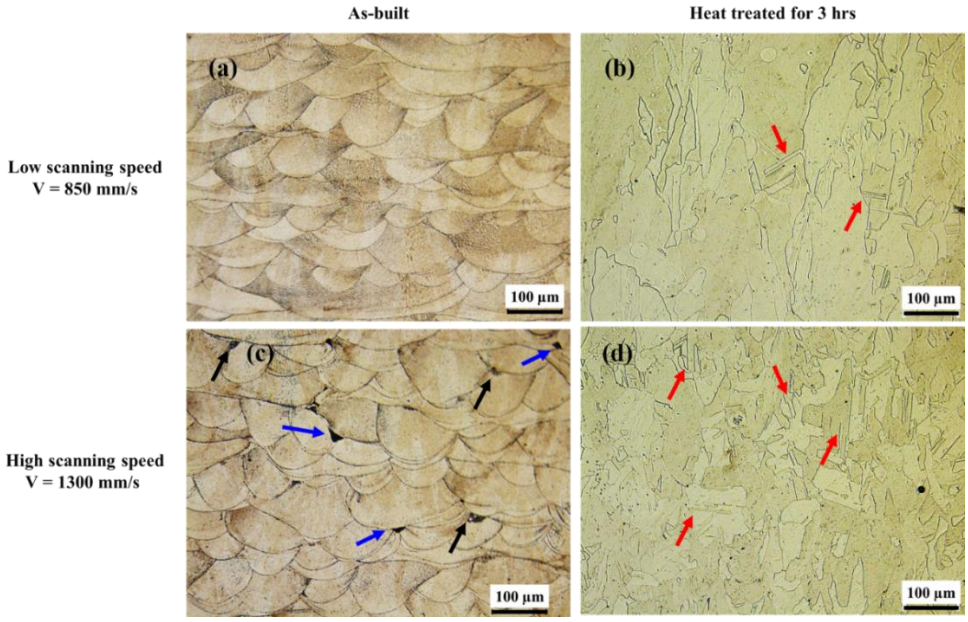

Figure. 58. Optical micrograph of the longitudinal cross-section of samples that are produced with the laser scanning speed of 850 mm/s (a,b) and 1300 mm/s (c,d) before and after 3 hours of heat-treatment.

As can be observed from Figure. 58, after 3 hours of annealing, very few annealing twins appear while the majority of the grains observed in the microstructure are the as-built solidified grains with columnar morphology. To increase the number of recrystallized grains in the microstructure, the annealing time was extended to 8.5 hours. Also, EBSD analysis with Kernel Average Misorientation (KAM) mapping was performed to distinguish recrystallized grains from as-built grains.

Figure. 59 shows the calculated kernel average misorientation (KAM) maps of as-built and annealed samples. Boundaries with misorientation values of more than 15˚ are shown in yellow and considered as high angle grain boundaries (HAGB). The maximum intensity of the local misorientation is 2˚ in both high and low scan speed samples. The KAM maps of as-built samples (Figure. 59. (a,e)) show that almost all grains are locally misoriented, while the annealing process introduces misorientation-free recrystallized grains embedded in the as-built structure (Figure. 59. (b-d,f-h)). The longer the annealing process, the higher the portion of misorientation-free regions in the microstructure.

It has been shown that the crystal misorientation gradient in the as-built grains directly follows the solidification and thermal path [132]. On the other hand, with a rotational scan strategy, thermal gradient direction alters from one direction to another, leading to the formation of a locally misoriented region in the solidified columnar grain. Considering the fact that local misoriented regions contain geometrically necessary dislocations [133], a potential driving force for recrystallization is the energy reduction associated with the removal of the initial solidified grains and the introduction of strain-free grains.

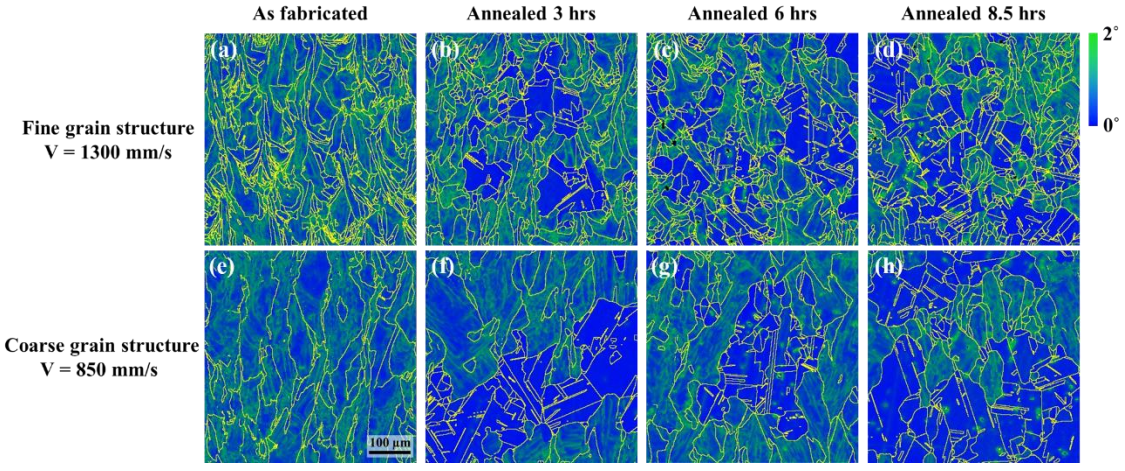

Figure. 59. Kernel average misorientation maps of samples which are produced by a scanning speed of 1300 mm/s (a-d) and 850 mm/s (c-h) in as-built and heat-treated conditions.

The presence of high dislocation density in the cell walls of LPBF Hastelloy X was reported by [129,134]. As dislocation density profoundly affects mechanical properties, it is also important to investigate the role of the heat-treatment and particularly the recrystallization process on the dislocation structure. In this

regard, an annealed LPBF sample produced with 850 mm/s laser scanning speed is selected for TEM analysis. The coarse grain structure makes it easier to distinguish recrystallized and non-recrystallized grains, and find an appropriate region to lift out with FIB and analyze with TEM. Figure. 60 shows STEM bright-field (BF) images of the sample produced with 850 mm/s laser scanning speed and heat-treated for 8.5 hours. As can be observed, there is a considerable difference in dislocation density between the recrystallized and as-built grains (Figure. 60 (a-c)). After 8.5 hours of heat-treatment, a significant amount of single dislocations can be observed in the recovered as-built grain where dislocations rearranged within the subgrain boundary with a stable configuration (Figure. 60 (b)). However, the recrystallized grain shows an almost dislocation-free structure with only a few ordered dislocations in the entire grain (Figure. 60 (a,c)). This significant reduction in dislocation density affects the yield strength of the annealed material, which is discussed in the quasi-static mechanical property section.

The corresponding selected area diffraction (SAD) patterns of recrystallized and as-built grains, which are displayed in the insets of Figure. 60 (a,b), confirm a high distortion in the nickel crystal structure with lattice constant parameters of $a = 3.63\ \mathring{A}$. This can be ascribed to a high concentration of solute atoms (such as Cr, Fe, and Mo) in the nickel matrix. It is also noteworthy to mention that no Mo-rich or Cr-rich M_xC_y carbides were observed in the samples heat-treated for 8.5 hours, which is in contrast to what was reported for post-heat-treated Hastelloy X LPBF samples [21,134,135]. This is due to the fact that the heat-treatment process in the current study is followed by water quenching, preventing the diffusional formation of M_xC_y carbides, which usually takes place at high temperatures up to ~980˚C [136]. However, oxide particles in the range of 50-100 nm in size were observed in the matrix, which will be discussed further in section 3.1.2.

Based on what was discussed in the aforementioned section, the driving force for recrystallization is lowering the internal energy of the deformed structure by replacing high dislocation density containing misoriented grains with misorientation and dislocation-free grains. However, the existence of locally misoriented subgrains after 8.5 hours of annealing (Figure. 59 (d,h) and Figure. 60 (b)) reveals that the distorted crystal structure cannot be solely responsible for starting and continuing the recrystallization process in LPBF parts. In fact, some other factors may also strongly affect the nucleation and growth of the recrystallized grains during recrystallization.

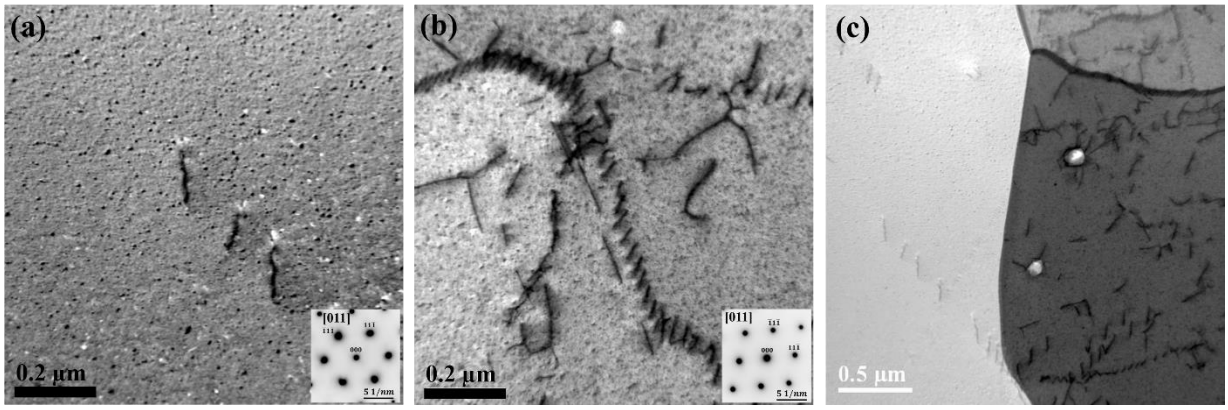

Figure. 60. BF-STEM images of the annealed sample after 8.5 hours of heat-treatment showing the dislocation structure in (a) recrystallized grain, (b) as-built grain, and (c) interface of recrystallized/solidified grains.

Figure 61 shows the inverse pole figure (IPF) maps of as-built and annealed microstructures and corresponding grain boundary maps. The calculated recrystallization fraction of heat-treated samples is shown in Figure 62, which is obtained based on the forward scatter detector (FSD) images from random locations. Recrystallization is taking place in up to ~52% and ~49% of the as-built microstructure produced with 850 mm/s and 1300 mm/s laser scanning speed, respectively. As is observed, the as-built samples only consist of columnar grains aligned with the building direction (Figure 61 (e,m)) while annealed samples show a significant amount of equiaxed grains surrounded by as-built grains (Figure 61 (f-h),(n-p)). Analysis of grain boundaries shows that the as-built grains contain low angle grain boundaries (LAGB), which are aligned with the building direction. However, recrystallized grains do not show LAGBs and instead, contain straight $\sum 3$ coincidence site lattice (CSL) boundaries without any visible preference in their orientation. It is also important to mention that the finer initial as-built LPBF grain structure (developed by higher scan speed) resulted in finer recrystallized grains in the annealed microstructure (Figure 61 (h,p)).

As was discussed in the previous section, recrystallization may develop strain-free grains in certain locations of the microstructure. However, it is important to identify the reason for the formation of newly recrystallized grains. Generally, static recrystallization is divided into two steps: nucleation and growth [137,138]. The nucleation step corresponds to the formation of a low internal energy crystal, which is separated from other grains by HAGBs. The growth step, however, is related to the migration of the HAGBs, replacing a distorted crystal structure by a new strain-free recrystallized grain [131]. A nucleus cannot form from the thermal fluctuation mechanism since the formation of a new HAGB requires a high value of surface energy [137]. However, existing subgrains with high misorientation angles (2-15˚) can provide the required mobility to develop into a recrystallized grain [131,137]. Pre-existing high local misorientations at HAGBs can act as nucleation sites to form a new crystal with a different orientation with respect to the parent grains [139,140]. Therefore, a finer grain structure at the initial stage may provide

more potential nucleation sites compared to a coarse grain structure (Figure 61 (h,p)). It is worth noting that the local misoriented regions (green regions in Figure. 59 (a,e)), which are not in the vicinity of HAGBs, may not act as potential nucleation sites due to the low mobility of their LAGB, resulting from the low misorientation angle. Consequently, the most effective parameter to influence the average grain size after the annealing process is the initial HAGB density, which corresponds to the number of potential nucleation sites during recrystallization.

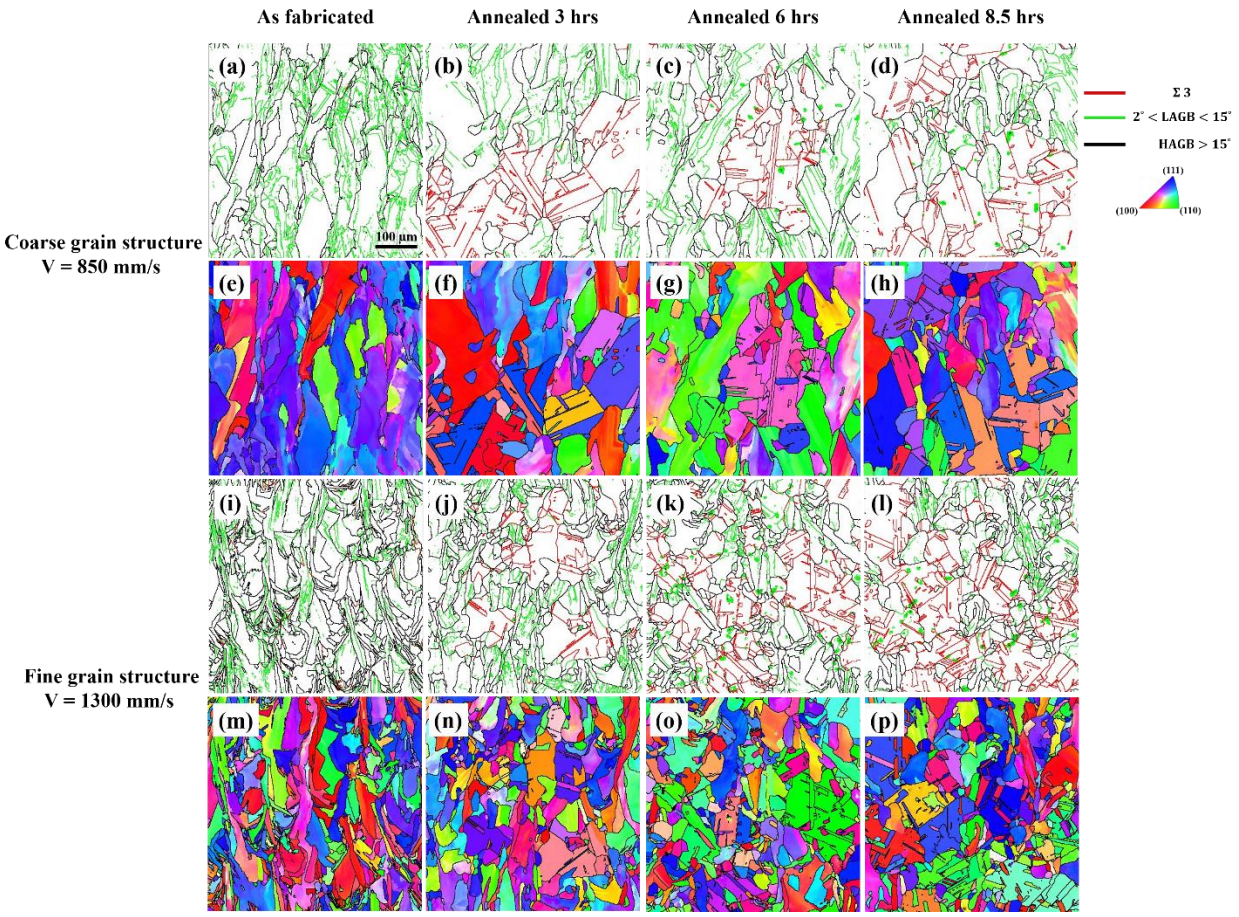

Figure 61. Development of recrystallized microstructure showed by EBSD IPF maps and grain boundary maps of samples produced with scanning speeds of 850 mm/s and 1300 mm/s in as-built and heat-treated conditions.

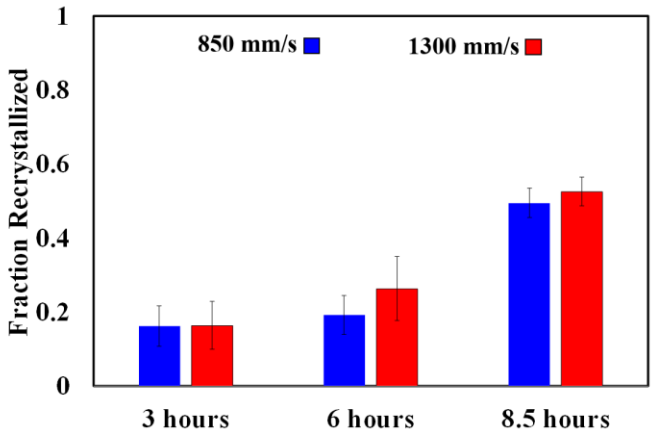

Figure 62. Recrystallization progress of samples produced with scanning speeds of 850 mm/s and 1300 mm/s.

To investigate the variation in grain boundary misorientation angle, the relative frequency of LAGBs (<15˚) and HAGBs (>15˚) in the as-built and annealed conditions are shown in Figure. 63. It is observed that low angle boundaries (mostly less than 10˚) are dominant in the as-built microstructure of both coarse and fine-grained structures, while annealing for 8.5 hours significantly generates new HAGB misorientation peaks (specifically at ~60˚ and to some extent at ~38˚). Also, the LAGBs can be found in the heat-treated samples but in relatively low frequencies in comparison to as-built samples.

Variations in the thermal gradient direction during solidification creates local misorientation in as-built grains (Figure. 59 (a,e)), which corresponds to the existence of LAGBs with high frequency (more than 50%) in the as-built structure (Figure. 63 (a,c)). On the other hand, after 8.5 hours of heat-treatment, HAGBs become dominant where the total percentage of HAGBs reach 52.6% and 55.7% in coarse and fine grain structure samples, respectively. Particularly, the total fraction of HAGBs with misorientation close to the coherent twin boundary is ~21% and ~26% in samples with coarse and fine grain structure, respectively. The presence of high-frequency HAGBs with around 60˚ misorientation after heat-treatment is correlated to the formation of annealing twins. An annealing twin can form through boundary migration if a growth fault occurs at triple points [131]. The driving force for the formation of the new grain, which is twinned with its parent grain, is the formation of ∑3 low energy boundaries, resulting in a drop in the total boundary energy of the material [131,137]. The density of the coherent twin-boundaries is highly dependant on the stacking fault energy (SFE) of the material [141]. With an increase in SFE, the probability of twin formation is decreased due to the lower stability of the twin boundary at higher energy [142]. Although the SFE of nickel is high at room temperature, it decreases dramatically at temperatures higher than its Curie temperature [111]. Furthermore, the addition of alloying elements (such as Al, Ti, Cr, and Mo in Hastelloy X) to a nickel matrix decreases the SFE of the alloy [143]. Therefore, annealing twins are expected to form after grain boundary migration and recrystallization in Hastelloy X.

It should be mentioned that the ~38˚ angle misorientation in grain boundary (as shown in Figure. 63 (b,d)) is related to the formation of very few boundaries with orientation close to that of $\sum 7$, which appeared after 3, 6, and 8.5 hours of heat-treatment. It is reported that grain boundaries close to the orientation of $\sum 7$ boundaries grow faster in FCC polycrystalline materials in comparison to the other grain boundaries [137]. Therefore, slow progress in the recrystallization process observed in the present study could be related to the low ratio of $\frac{HAGB\ Orientation\ close\ to \sum 7}{HAGB\ Orientation\ close\ to \sum 3}$. This low ratio implies a high density of low energy boundaries rather than mobile grain boundaries, which could have decelerated the growth process during recrystallization.

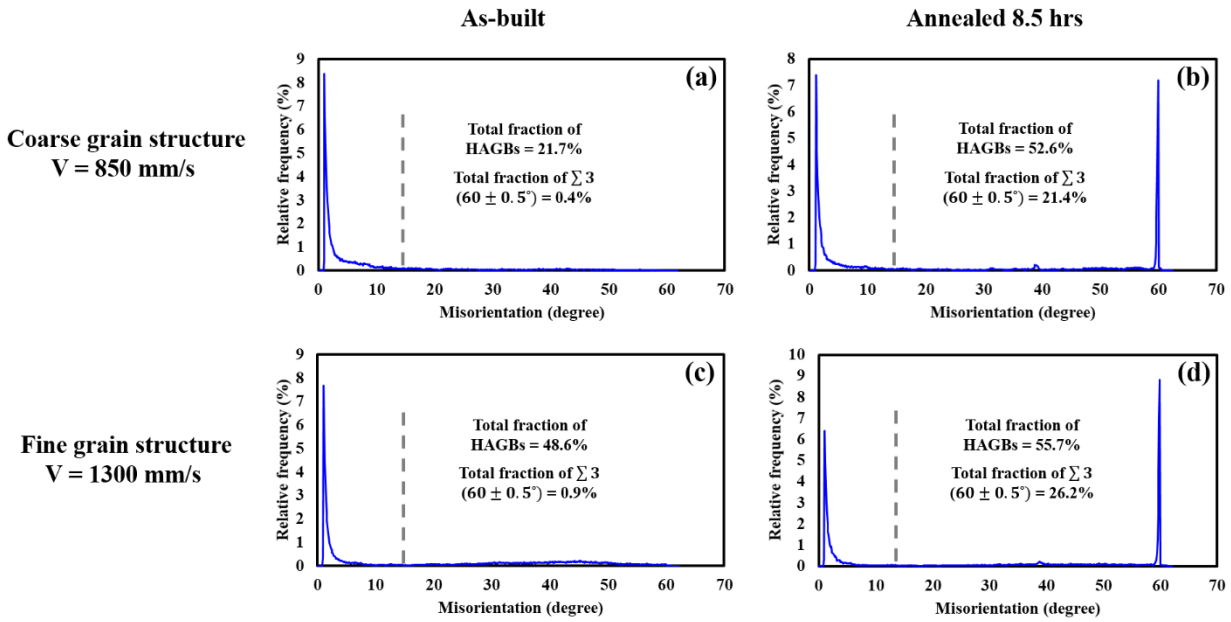

Figure. 63. Misorientation-angle distribution of as-built and annealed samples with scanning speeds of (a,b) 850 mm/s and (c,d) 1300 mm/s. Note: the class width of the histograms is 0.1˚.

6.3.1.2 Boundary migration inhibition during recrystallization

Based on the results presented in Figure 62, only ~50% of the microstructure was recrystallized after 8.5 hours of the high-temperature annealing process in both coarse (with 850 mm/s) and fine (with 1300 mm/s) grained structures. The effect of this microstructural change on the mechanical properties of the heat-treated material will be discussed in the mechanical property section. However, to understand the cause of the slow progress of recrystallization, it is important to address the reason why and how the as-built grains still

appear after 8.5 hours of annealing. We believe this is related to the presence of immobile grain boundaries and oxide particle (which is stabled in high temperature) pinning during the growth step of recrystallization.

6.3.1.2.1 Low mobility boundaries

Figure. 64 (a) shows the IPF map of the 850 mm/s sample after 8.5 hours of heat-treatment in which 52.8% of the as-built microstructure is replaced by strain-free recrystallized grains. Some magnified regions on the interface of the recrystallized and as-built grains are also shown in Figure. 64 (b-d) to investigate more details of the recrystallization process. It is observed that a growing recrystallized grain may meet regions in the as-built structure with a similar crystallographic orientation (shown by the red arrow in Figure. 64 (b)). This creates a low mobility LAGB (shown with white color lines in Figure. 64 (a,b)), which grows very slowly. On the other hand, many other grains are observed to create grain boundary misorientation angles close to that of the coherent twin boundary (e.g. grain boundary between grain A and B with a ~57˚ misorientation angle). Subsequently, the low mobility grain boundaries give rise to grain migration inhibition during recrystallization.

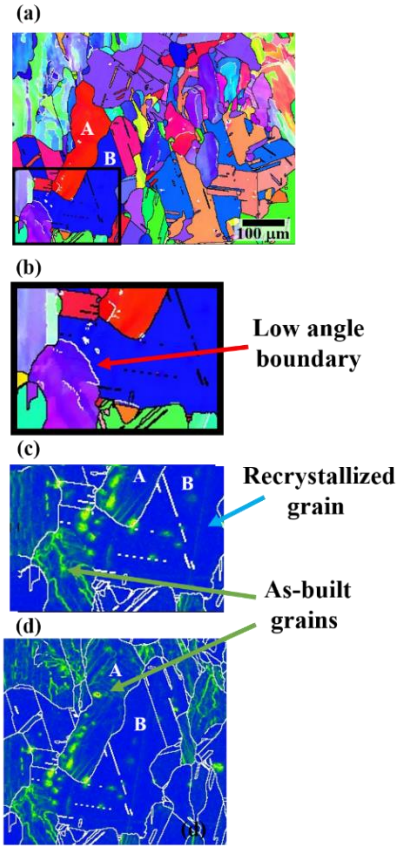

Figure. 64. EBSD IPF and KAM maps showing grain boundary inhibition during recrystallization due to the development of LAGBs between solidified grains and recrystallized grains.

6.3.1.2.2 Particle pinning

Most commercial alloys include fine particles that strongly influence the recrystallization progress during heat-treatment. Particles with short distance spacing can act as a barrier to the migration of both HAGBs and LAGBs [137]. Previously, closely spaced and fine Al-Ti-O enriched particles have been observed in the as-built microstructure of LPBF Hastelloy X [134]. Interestingly, in the current study, the presence of closely spaced Al-Ti-O enriched particles was detected after 8.5 hours of the solutionizing process, mainly in as-built grains (Figure. 65 (a-d)). The EDS measurement reveals that the composition of these particles is 46.5 at.% Al, 42.7 at.% O, 2.7 at.% Ti, and 8.1 at.% of all other remaining elements. The size of these particles is in the range of 40-100 nm. It is also observed that the density of these particles in the as-built grain is higher compared to the recrystallized grain (Figure. 65 (c,d)). Figure. 65 (a,b) shows the BF-STEM image of the microstructure after 8.5 hours of annealing in which the grain boundary between a recrystallized and as-built grain is impeded due to the existence of closely distanced Al-Ti-O enriched second phases. Therefore, during the growth step, some grain boundaries meet pre-existing fine dispersoids. This can delay or even prevent further growth of the recrystallized grains.

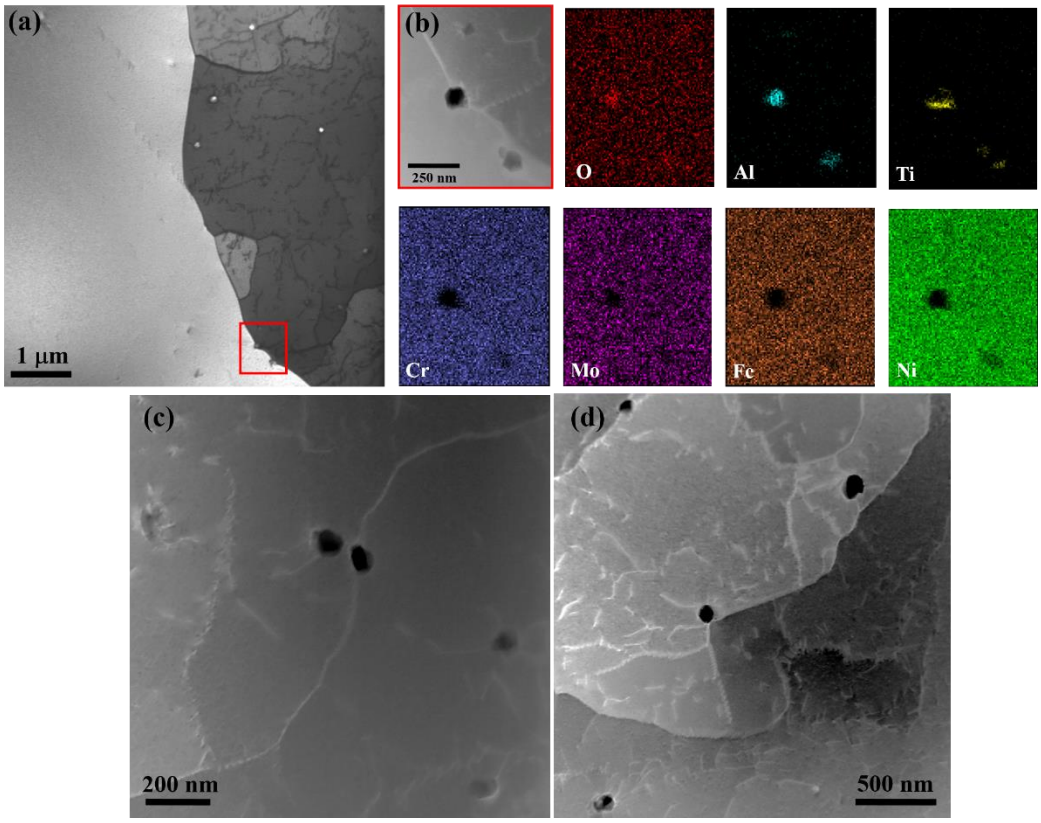

Figure. 65. (a) BF-STEM image around grain boundary between as-built and recrystallization grain, (b) EDS map of the inset shown in (a) displays the presence of Al-Ti-O enriched second phases at a grain boundary. (c,d) Dark-field STEM image of some Al-Ti-O particles in the as-built grains.

6.3.2 Quasi-static mechanical properties

To investigate the effect of the heat-treatment on the tensile properties (ultimate tensile strength (UTS), yield strength (YS), and elongation) of LPBF samples, monotonic tensile tests are implemented on samples in both heat-treated and as-built conditions. In addition, to study the effectiveness of the heat-treatment process on the alleviation of anisotropic mechanical response, samples are produced in horizontal and vertical directions and compared together in as-built and heat-treated conditions.

Figure. 66(a-c) displays the values of YS, UTS, and elongation for annealed and as-built samples. Comparing the values of YS of the samples shows that the highest YS (~689 MPa) belongs to the sample printed at 1300 mm/s in the horizontal direction, while the lowest YS (~300 MPa) is related to the annealed samples. In the as-built condition, there is a significant difference between the YS of vertically and horizontally as-built samples. The YS of horizontally printed samples is about 73 MPa and 192 MPa higher than that of vertically printed samples at 850 mm/s and 1300 mm/s, respectively. However, the annealing process seems to completely alleviate the anisotropic yielding behavior of the as-built material so that samples printed at both higher and lower scanning speeds show almost the same values of YS after heat-treatment regardless of the printing direction.

It is reported that morphological anisotropy in grain structure can be responsible for the observed difference in mechanical strength between vertically and horizontally built samples provided that only columnar grains exist in the microstructure [129]. However, 8.5 hours of annealing process changes the overall morphology of the grains by introducing a large volume of recrystallized equiaxed grains in the microstructure, alleviating the YS difference in the horizontal and vertical direction. In addition, the recovery process, including rearrangement and annihilation of dislocation structures, removes the internal residual stress. This leads to a nearly similar yielding response (~300 MPa) in different directions, along with the formation of ~50% strain-free and equiaxed recrystallized grains (Figure. 59 (d,h)).

In terms of UTS, the highest UTS (~780 MPa) is observed for horizontally printed samples, while the lowest UTS (590 – 630 MPa) is obtained for annealed and vertically printed samples. Comparing the horizontal samples to vertical samples reveals that the difference between the UTS values of as-built 850 mm/s and 1300 mm/s samples is ~127 MPa and ~73 MPa, respectively. However, this difference in UTS values is reduced to ~100 MPa and ~46 MPa for annealed samples after 8.5 hours of heat treatment. Since the YS is almost the same for all 8.5 hours annealed samples, the anisotropic UTS response can be attributed to the difference in the work hardening rate in different directions, which is related to the remained columnar structure.

Based on the results presented in Figure. 66(c), vertical samples show ~26% and ~12% higher elongation compared to horizontal samples printed at 850 mm/s and 1300 mm/s, respectively. It was reported that the columnar morphology of grains and their corresponding aspect ratio were responsible for the anisotropy in the elongation of LPBF parts [21,129]. In the case of the present study, recrystallized grains with equiaxed grain morphology results in alleviation of anisotropic behavior in elongation whereas no significant difference in elongation is observed with respect to the sample orientation. It is also important to note that elongation in vertical samples is not changed after heat-treatment as it is already in the range of reported elongation for solution annealed Hastelloy X (50 - 60%) [130]. However, the elongation of horizontally printed samples increased significantly by ~14% after heat-treatment for samples printed at 850 mm/s and 1300 mm/s. This is expected since the as-built samples show significantly lower elongation than that reported for standard solution annealed Hastelloy X [130].

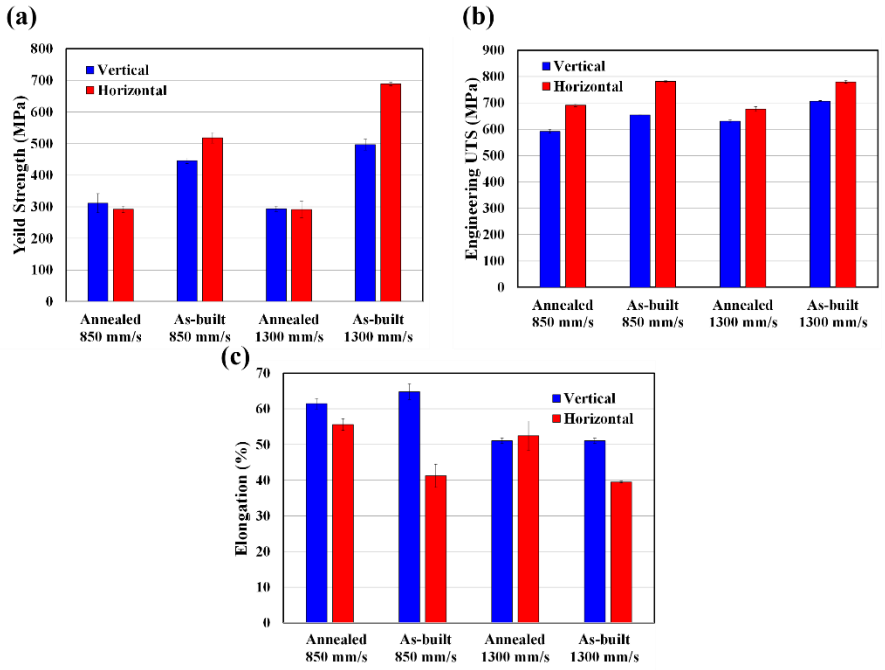

Figure. 66. Bar plot of (a) YS, (b) UTS, and (c) elongation in horizontal and vertical directions obtained from as-built and 8.5 hours heat-treated samples.

Figure. 67 (a,c) shows the stress-strain curves of the tensile samples in as-built and heat-treated conditions. In addition, curves for strain hardening rate versus true strain are displayed in Figure. 67 (b,d). It is believed that FCC materials with medium-range stacking-fault energy (e.g. IN625 and Hastelloy X) show a four-stage strain hardening behavior (A, B, C, and D) during a uniaxial compression test [144]. At the beginning (stage A, Figure. 67 (b,d)), a rapid decrease in the strain hardening rate occurs when the true strain is increasing. However, stage A is interrupted by stage B where a constant or slightly decreasing strain

hardening rate appears. At stage C, a second decreasing regime in strain hardening rate occurs with a much lower slope compared to stage A. It is observed that a second constant strain hardening rate (known as stage D) appears at very large stains. In the current study, stage D was not observed because of necking, where the strain instability takes place earlier than the required true strain for starting stage D.

The falling regime in stage A is mostly associated with the cross-slip of dislocations in FCC polycrystalline materials [145,146]. With increasing true strain, slip planarity can occur due to large lattice fractional stress and short-range ordering (SRO) [144]. Large solute atoms (such as Mo in Hastelloy X) may apply a large lattice frictional stress on dislocations and therefore, more energy is required for dissociated dislocations to join and form a perfect dislocation [144,147]. In addition, the formation of SRO is reported in Ni-Cr alloys to be further facilitated by a post-heat-treatment process [144,148]. The movement of a pair of dissociated dislocations through SRO is thermodynamically unfavorable and creates extra energy in the system [144]. Therefore, stage A will be terminated by stage B in which the cross-slip of dislocations is interrupted and a planar movement of pair dislocations takes place. However, the applied force increases with an increase in true strain. Therefore, at some point (beginning of stage C) Shockley partials can prevail over the lattice frictional stress to form perfect dislocations, giving rise to easier cross-slip. This causes a drop in the strain hardening rate at stage C.

As is seen in Figure. 67 (b,d), for the samples printed with the same orientation (vertical or horizontal), the annealed samples show a higher strain hardening rate in comparison with as-built samples. This can be due to the existence of twin boundaries which act as a barrier for slip propagation during deformation. Although the YS of annealed samples is much lower than that of as-built ones (200 – 400 MPa), a smaller difference in UTS (~100 MPa) is observed between annealed and as-built samples because of the higher strain hardening rate in annealed samples (Figure. 67 (b,d)). On the other hand, after the annealing process, the strain hardening rate was observed to be higher in the horizontal direction compared to the vertical one. This can be attributed to the remaining as-built columnar grains in the microstructure after 8.5 hours of annealing (Figure 61 (h,p)).

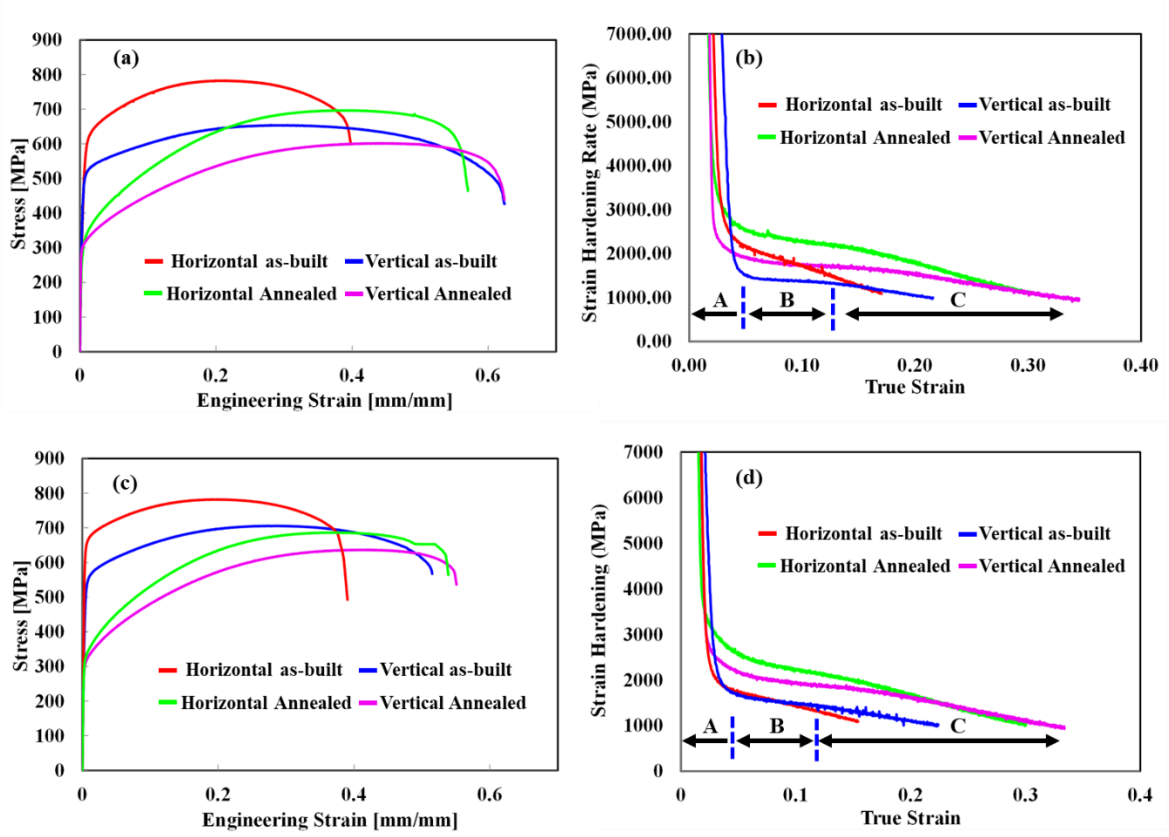

Figure. 67. (a) Engineering stress-strain curves of as-built and heat-treated samples with a laser scanning speed of (a) 850 mm/s and (c) 1300 mm/s. Also, the corresponding strain hardening rate-true strain curves are shown in (b) for the laser scanning speed of 850 mm/s and in (d) for LSS of 1300 mm/s.

6.3.3 Distortion after support removal

To investigate the effectiveness of the heat-treatment process in terms of relieving the internal stresses, cantilevers were produced on LPBF substrates and support structures. In the as-built sample, after cutting cantilevers from the support structure, the deflection of the cantilever's tip was around $2.1 \pm 0.1\, mm$ (Figure. 68(a,b)). However, annealing of the sample for 8.5 hours before support removal results in no significant deflection of the cantilever after the cutting process (Figure. 68(c,d)).

Interaction between the elastic stress fields around dislocations may generate internal stresses in the material [131]. For example, the repulsive force between two positive and parallel screw dislocations is $F = \frac{Gb^2}{2\pi x}$, where G, b, and x are the shear modulus of the material, Burgers vector, and distance between the dislocations, respectively [131,149]. As dislocation density increases in the material, the average distance between dislocations decreases, which in turn, increases the internal stresses. The origin of the residual stresses in the as-built LPBF material is plastic deformation resulting from non-uniform local

thermal expansion and high dislocation density [96]. To minimize the internal stresses, dislocation annihilation during the recovery and recrystallization process can be beneficial. In as-built grains, the two parallel dislocations of opposite Burgers vector (dislocation dipole) can annihilate each other by gliding, climbing, or a combination of both if they are thermally activated [131]. Therefore, the density of dislocations may decrease dramatically (as shown in Figure. 60). As a result, internal stresses and corresponding deflection after annealing and support removal may alleviate deflection along with the formation of strain-free and equiaxed recrystallized grains (Figure. 59 (d,h)).

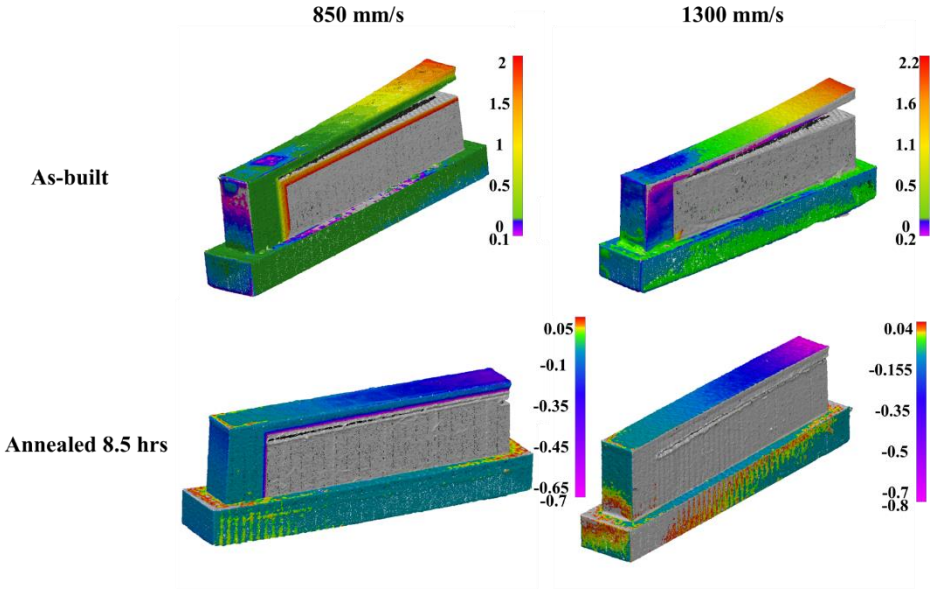

Figure. 68. 3D optical scanned images of as-built and annealed samples. [Note: the deflection of the cantilever's tip is alleviated after 8.5 hours of heat-treatment].

6.4 Conclusion

In this work, as-built and heat-treated LPBF Hastelloy X samples were analyzed. An in-depth analysis has been done into the change in microstructure, such as local misorientation, dislocation structure, and grain boundary structure after a heat-treatment process. Effects of the altered microstructure on the quasi-static tensile response – including anisotropic tensile behavior and work hardening rate – were also investigated. The main conclusions from the current study are as follows:

- Post-heat-treatment of LPBF Hastelloy X can result in static recrystallization where as-built misoriented crystals (up to 2˚) are replaced by strain-free grains without local misorientation. Recrystallization fraction is highly dependent on annealing time and can vary from ~16% to ~50% when the heat-treatment time changes from 3 hours to 8.5 hours.
- The initial grain size of the LPBF microstructure plays an important role in recrystallization. Comparing coarse grain structure (produced with a lower scanning speed of 850 mm/s) to fine

grain structure (produced with a higher scanning speed of 1300 mm/s) reveals that the initial finer LPBF grain structure, which includes higher grain boundary density, provides more nucleation sites for recrystallization and makes the heat-treated grain structure finer.

- As-built Hastelloy X samples contain only columnar grains which are enriched with LAGBs parallel to the building direction. After 8.5 hours of solution treatment, however, the former columnar grain structure is replaced by equiaxed grains with non-oriented ∑3 CSL boundaries. The LAGB total fraction is more than 50% in the as-built condition, however, after 8.5 hours of solution treatment, the HAGBs become a majority. In this case, 21% and 26% of boundaries are allocated to ∑3 CSL boundaries in the samples produced with a laser scanning speed of 850 mm/s and 1300 mm/s, respectively.
- After 8.5 hours of heat-treatment, pre-existing Al-Ti-O nanoparticles (40 – 100 nm) slow down the progress of recrystallization, along with the formation of low mobility boundaries between recrystallized and as-built grains.
- Before heat-treatment, the YS of horizontally printed samples is about 73 MPa and 192 MPa higher than that of vertically printed samples at 850 mm/s and 1300 mm/s, respectively. However, recrystallization after 8.5 hours of heat-treatment completely alleviates the anisotropic yield response.
- The UTS difference in horizontal and vertical samples is decreased by ~27% and ~37% after the 8.5-hour solution treatment of printed samples at 850 mm/s and 1300 mm/s, respectively. The remaining UTS anisotropic response can be related to the residual as-built columnar grains.
- Deflection of parts after support removal can be alleviated with the help of 8.5 hrs of solutionizing followed by water quenching. This can be due to the change in dislocation structure after the heat-treatment process.

7 Conclusions and Future Work

Microstructural characterization and simulation of laser powder-bed fusion are performed throughout this thesis. A fundamental study has been done on the melt pool solidification process, which significantly helped to comprehend the related phenomena of microstructure formation of LPBF parts. This includes nucleation mechanism, growth mechanism, and melt pool formation. Also, the effect of laser heat-source parameters (laser scanning velocity and laser power) on the single-track microstructure is investigated. Since the single-track study provided a deep understanding of melt pool solidification, a microstructural simulation is aimed to predict the as-built microstructure. The solidification simulation project is focused on grain structure prediction by mimicking the epitaxial grain growth during the LPBF process. Many input data were required for the solidification phase-field simulation, taken mostly from single-track experiments from the previous chapter. Besides, experimental validation shows a good agreement between experimental and simulation results. Also, the simulation study brought an insight value into the microstructure formation during the solidification process. It is worth mentioning to say that some of the obtained knowledge from microstructural simulation could not be done through experimental techniques as they only show the beginning and final microstructure without any observation from microstructure formation during solidification.

With the obtained knowledge from the phase-field simulation study, the next chapter is focused on controlling the fabricated microstructure by changing the most important criteria in the solidification. It is designed to change the temperature gradient directions between successive layers by varying the solidification pattern of LPBF. It is shown that the scanning strategy of laser heat-source can control grain size and crystallographic texture of LPBF parts. Changes in scanning strategy showed a significant impact on grain size but it is not an effective way to remove the anisotropy in grain morphology and anisotropic response in mechanical behavior. Therefore, another attempt at post-processing LPBF parts is made in the next chapter to annihilate the columnar grain structure by recrystallization and creation of equiaxed structure in the microstructure. It is shown that direct recrystallization through a proper high-temperature heat-treatment is an effective way for alleviation of mechanical anisotropy. However, some obstacles (e.g. particle pinning and low angle grain boundaries) have been identified for recrystallization progress during the heat-treatment. Besides, the dislocation structure of recrystallized and as-built grains have been compared together. The effectiveness of the heat-treatment process has been shown by comparing the mechanical behavior of heat-treated to as-built parts.

7.1 Conclusions

Some of the most important conclusions of this thesis can be described as follows:

- The melt pool microstructure consists of a fine cellular structure in coarse columnar grains due to the high G/R value during rapid solidification. Melt pool dimensions (width and depth) may vary at a fixed laser energy density (LED) value due to different strengths of laser power and velocity. Besides, at fixed LED of 0.25 J/mm a ~90% increase in new grains is observed in the solidified melt pool, which results in a finer microstructure at the laser power of 150 W and 350 W, respectively.
- Due to grain detachment from partially melted powders (PMP), a significant amount of bulk nucleation is happening during the melt pool solidification. It is proposed that the increase in the number of grains in the melt pool is attributed to the increase in width of the cooler band of molten metal, which raises the number of survived PMP and nucleation rate. For example, at fixed LED of 0.25 J/mm, changing the laser power from 150 W to 300 W results in the increase in the width of the cooler band (from ~37 μm to ~45μm) of molten metal and rise the number of new grains in the melt pool.
- Considering the anisotropy in solidification (crystal growth), experimental nucleation data, melt pool geometry, and melt pool temperature gradient in the phase-field model can give us a fair accuracy to the simulated the grain structure. In this regard, a single track melt pool solidification simulation has been performed. The grain growth paths were shown to be almost the same as the experimental result when an actual initial condition (obtained from the experimental measurement) is assigned to the system.
- The justification of grains side-branching has been done in the multi-track simulation section. It is visualized that grains in the vicinity of single-tracks overlap can get a chance to grow in two different easy growth directions, which are parallel to two different temperature gradients from adjacent melt pools.
- In the multi-layer deposition, due to the existence of the powder-bed (with a higher number in PMP nucleation), a finer grain structure is observed from side areas (in-touch with powder-bed) compared to the core. This is confirmed by both simulation and experimental results from the Multi-layer study.
- The width of simulated columnar grain measured between 79-102 μm when the experimental measurements from EBSD analysis show columnar grain's width between 80-91μm.
- It is discovered that higher randomness in the heat-flow direction will result in a higher number of grains involved in epitaxial growth during solidification. Changing the laser scanning strategy can be an effective way to increase the randomness in the heat flow direction. For example, the average grain size from three normal cross-sections of Stripe Uni and Stripe Rot samples were observed as

~734 µm and 85 µm, respectively, due to the increase in heat flow randomness from the Stripe Uni scanning strategy to the Stripe Rot scanning strategy.

- The as-built columnar grain morphology is one of the main reasons to have a strong anisotropic mechanical response. In this regard, quasi-static loading along with building direction results in the highest total elongation and lowest UTS compared to loading along with horizontal directions when the lowest number of grain boundaries along the building direction was detected. For example, in the Stripe Rot sample, the average width of grains in tangential direction was around three times smaller than building direction. Hence, a higher UTS (~170 MPa) and lower total elongation (~14%) were observed from tangential direction compared to building direction.

- Post-heat-treatment of LPBF parts can be used to employ static recrystallization to alleviate most of the anisotropic mechanical response. While as-built grains are observed to be distorted and misoriented (up to 2˚), recrystallized strain-free grains are detected to be stain-free and without any visible local misorientation. The recrystallization progress is highly controlled by annealing time when 3 hours to 8.5 hours of annealing can vary the fraction recrystallized from ~16% to ~50%.
- Pre-existing Al-Ti-O nanoparticles (40 – 100 nm) along with low-angle grain boundaries formation were identified as obstacles for the recrystallization progress. The crystallographic structure of these phases is still unknown and needs further characterization analysis.
- The heat-treatment process was successful in terms of alleviation in anisotropic mechanical response. For example, the yield strengths of as-built samples are measured to be higher in the horizontal direction compared to the vertical direction (up to 192 MPa). However, after heat-treatment, the difference in yield strength between horizontal and vertical directions is completely disappeared in all conditions.

7.2 Recommendations and Future Work

It is intended to predict and control the microstructure of the LPBF Hastelloy X material. Based on the results and discussions which were previously described in the earlier section, the primary goal has been fulfilled in this research work. However, it is realized that there are so many aspects of the project which can be improved or extended for further studies. Therefore, some recommended future work has been proposed in this section as follows:

- In the current study, a phase-field model is utilized to predict the grain structure of the LPBF microstructure. While the model is capable of predicting many aspects of FCC, BCC, and HCP materials, it is only tested for Hastelloy X. Theoretically, prediction of other materials can be done with the required thermal data and phase-field parameters.

- Since Hastelloy X is a solid solution strengthened Ni-based material, the prediction of the second phases was out of the scope of the current study. However, for other Ni-based superalloys (e.g. Inconel 718) second phase prediction can be useful as it is involved in solidification cracking and mechanical properties of LPBF material. In this case, a set of diffusion equations can be coupled to the proposed model to predict the formation of secondary phases.

- While the scanning strategy can change the grain structure and crystallographic texture of the LPBF material, it can also be utilized to make functionally graded materials. During the build-up process, the scanning strategy can be easily changed without affecting the manufacturing process. However, the change in the microstructure will be done gradually and requires its individual research study.

- It is discussed in Chapter 6 that the static recrystallization during a direct high-temperature heat-treatment is slow and time-consuming. This is mostly attributed to the low number of nucleation positions in the microstructure. In this case, some pre-existed particles can be added to the metallic powder to help the nucleation process to make the recrystallization faster. Considering that this additional particle may affect the solidification and powder characteristics from the beginning of the LPBF process, finding the appropriate material for nucleation purposes can be very challenging.

Letter of copyright permission

This section is providing the necessary copyright permissions for those materials which have been re-used in this thesis. The licenses and permissions for Chapters 3, 5, and 6 from Elsevier (publisher) have been granted. It is Elsevier's policy that, "as the author of the Elsevier article, you retain the right to include it in a thesis or dissertation, provided it is not published commercially. Permission is not required, but please ensure that you reference the journal as the original source." A proper referencing is applied in this thesis to give the credit to the respective publication. Also, this section provides the licenses and the permissions for using figures from different articles:

Permission for Figure 2:

ELSEVIER LICENSE
TERMS AND CONDITIONS

Apr 30, 2021

This Agreement between University of Waterloo -- Ali Keshavarzkermani ("You") and Elsevier ("Elsevier") consists of your license details and the terms and conditions provided by Elsevier and Copyright Clearance Center.

License Number	5058910919792
License date	Apr 30, 2021
Licensed Content Publisher	Elsevier
Licensed Content Publication	Materials & Design
Licensed Content Title	A critical review of powder-based additive manufacturing of ferrous alloys: Process parameters, microstructure and mechanical properties
Licensed Content Author	Haniyeh Fayazfar,Mehrnaz Salarian,Allan Rogalsky,Dyuti Sarker,Paola Russo,Vlad Paserin,Ehsan Toyserkani
Licensed Content Date	Apr 15, 2018
Licensed Content Volume	144
Licensed Content Issue	n/a
Licensed Content Pages	31
Start Page	98
End Page	128
Type of Use	reuse in a thesis/dissertation

Permission for Figures 3:

PLS Clear

PARTIES:

1. **Cambridge University Press** [CompanyNumber] (Licensor); and
2. **Ali Keshavarzkermani** (Licensee).

Thank you for your recent permission request. Some permission requests for use of material published by the Licensor, such as this one, are now being facilitated by PLSclear.

Set out in this licence cover sheet (the **Licence Cover Sheet**) are the principal terms under which Licensor has agreed to license certain Licensed Material (as defined below) to Licensee. The terms in this Licence Cover Sheet are subject to the attached General Terms and Conditions, which together with this Licence Cover Sheet constitute the licence agreement (the **Licence**) between Licensor and Licensee as regards the Licensed Material. The terms set out in this Licence Cover Sheet take precedence over any conflicting provision in the General Terms and Conditions.

Free Of Charge Licence Terms

Licence Date:	30/04/2021
PLSclear Ref No:	50279

The Licensor

Company name:	Cambridge University Press
Address:	University Printing House Shaftesbury Road Cambridge CB2 8BS GB

The Licensee

Licensee Contact Name:	Ali Keshavarzkermani
Licensee Address:	200 University Ave W Waterloo N2L 3G1 Canada

Licensed Material

title:	The Superalloys: Fundamentals and Applications
ISBN:	9780521859042
publisher:	Cambridge University Press

Permission for Figure 5:

PLS Clear

PARTIES:

1. **Cambridge University Press** [CompanyNumber] (Licensor); and
2. **Ali Keshavarzkermani** (Licensee).

Thank you for your recent permission request. Some permission requests for use of material published by the Licensor, such as this one, are now being facilitated by PLSclear.

Set out in this licence cover sheet (the **Licence Cover Sheet**) are the principal terms under which Licensor has agreed to license certain Licensed Material (as defined below) to Licensee. The terms in this Licence Cover Sheet are subject to the attached General Terms and Conditions, which together with this Licence Cover Sheet constitute the licence agreement (the **Licence**) between Licensor and Licensee as regards the Licensed Material. The terms set out in this Licence Cover Sheet take precedence over any conflicting provision in the General Terms and Conditions.

Free Of Charge Licence Terms

Licence Date:	30/04/2021
PLSclear Ref No:	50279

The Licensor

Company name:	Cambridge University Press
Address:	University Printing House Shaftesbury Road Cambridge CB2 8BS GB

The Licensee

Licensee Contact Name:	Ali Keshavarzkermani
Licensee Address:	200 University Ave W Waterloo N2L 3G1 Canada

Licensed Material

title:	The Superalloys: Fundamentals and Applications
ISBN:	9780521859042
publisher:	Cambridge University Press

Permission for Figure 10:

ELSEVIER LICENSE
TERMS AND CONDITIONS

Apr 30, 2021

This Agreement between University of Waterloo -- Ali Keshavarzkermani ("You") and Elsevier ("Elsevier") consists of your license details and the terms and conditions provided by Elsevier and Copyright Clearance Center.

License Number	5058930572177
License date	Apr 30, 2021
Licensed Content Publisher	Elsevier
Licensed Content Publication	Materials Science and Engineering: A
Licensed Content Title	Influence of post heat treatments on anisotropy of mechanical behaviour and microstructure of Hastelloy-X parts produced by selective laser melting
Licensed Content Author	Dacian Tomus,Yang Tian,Paul A. Rometsch,Martin Heilmaier,Xinhua Wu
Licensed Content Date	Jun 14, 2016
Licensed Content Volume	667
Licensed Content Issue	n/a
Licensed Content Pages	12
Start Page	42
End Page	53
Type of Use	reuse in a thesis/dissertation

Permission for Figure 11:

ELSEVIER LICENSE
TERMS AND CONDITIONS

Apr 30, 2021

This Agreement between University of Waterloo -- Ali Keshavarzkermani ("You") and Elsevier ("Elsevier") consists of your license details and the terms and conditions provided by Elsevier and Copyright Clearance Center.

License Number	5058930768629
License date	Apr 30, 2021
Licensed Content Publisher	Elsevier
Licensed Content Publication	Materials Characterization
Licensed Content Title	Selective laser melting of Co-29Cr-6Mo alloy with laser power 180–360W: Cellular growth, intercellular spacing and the related thermal condition
Licensed Content Author	K. Darvish,Z.W. Chen,M.A.L. Phan,T. Pasang
Licensed Content Date	Jan 1, 2018
Licensed Content Volume	135
Licensed Content Issue	n/a
Licensed Content Pages	9
Start Page	183
End Page	191
Type of Use	reuse in a thesis/dissertation

Permission for Figure 12:

ELSEVIER LICENSE
TERMS AND CONDITIONS

Apr 30, 2021

This Agreement between University of Waterloo -- Ali Keshavarzkermani ("You") and Elsevier ("Elsevier") consists of your license details and the terms and conditions provided by Elsevier and Copyright Clearance Center.

License Number	5058930768629
License date	Apr 30, 2021
Licensed Content Publisher	Elsevier
Licensed Content Publication	Materials Characterization
Licensed Content Title	Selective laser melting of Co-29Cr-6Mo alloy with laser power 180–360W: Cellular growth, intercellular spacing and the related thermal condition
Licensed Content Author	K. Darvish,Z.W. Chen,M.A.L. Phan,T. Pasang
Licensed Content Date	Jan 1, 2018
Licensed Content Volume	135
Licensed Content Issue	n/a
Licensed Content Pages	9
Start Page	183
End Page	191
Type of Use	reuse in a thesis/dissertation

Permission for Figure 13-16:

ELSEVIER LICENSE
TERMS AND CONDITIONS

Apr 30, 2021

This Agreement between University of Waterloo -- Ali Keshavarzkermani ("You") and Elsevier ("Elsevier") consists of your license details and the terms and conditions provided by Elsevier and Copyright Clearance Center.

License Number	5058930955658
License date	Apr 30, 2021
Licensed Content Publisher	Elsevier
Licensed Content Publication	Materials Characterization
Licensed Content Title	Microstructure of selective laser melted CM247LC nickel-based superalloy and its evolution through heat treatment
Licensed Content Author	V.D. Divya,R. Muñoz-Moreno,O.M.D.M. Messé,J.S. Barnard,S. Baker,T. Illston,H.J. Stone
Licensed Content Date	Apr 1, 2016
Licensed Content Volume	114
Licensed Content Issue	n/a
Licensed Content Pages	13
Start Page	62
End Page	74
Type of Use	reuse in a thesis/dissertation

Permission for Figure 18:

ELSEVIER LICENSE
TERMS AND CONDITIONS

Apr 30, 2021

This Agreement between University of Waterloo -- Ali Keshavarzkermani ("You") and Elsevier ("Elsevier") consists of your license details and the terms and conditions provided by Elsevier and Copyright Clearance Center.

License Number	5058930955658
License date	Apr 30, 2021
Licensed Content Publisher	Elsevier
Licensed Content Publication	Materials Characterization
Licensed Content Title	Microstructure of selective laser melted CM247LC nickel-based superalloy and its evolution through heat treatment
Licensed Content Author	V.D. Divya,R. Muñoz-Moreno,O.M.D.M. Messé,J.S. Barnard,S. Baker,T. Illston,H.J. Stone
Licensed Content Date	Apr 1, 2016
Licensed Content Volume	114
Licensed Content Issue	n/a
Licensed Content Pages	13
Start Page	62
End Page	74
Type of Use	reuse in a thesis/dissertation

Permission for Figure 19:

ELSEVIER LICENSE
TERMS AND CONDITIONS

Apr 30, 2021

This Agreement between University of Waterloo -- Ali Keshavarzkermani ("You") and Elsevier ("Elsevier") consists of your license details and the terms and conditions provided by Elsevier and Copyright Clearance Center.

License Number	5058931373150
License date	Apr 30, 2021
Licensed Content Publisher	Elsevier
Licensed Content Publication	Materials Characterization
Licensed Content Title	Nickel-based superalloy microstructure obtained by pulsed laser powder bed fusion
Licensed Content Author	Y. Tian,J.A. Muñiz-Lerma,M. Brochu
Licensed Content Date	Sep 1, 2017
Licensed Content Volume	131
Licensed Content Issue	n/a
Licensed Content Pages	10
Start Page	306
End Page	315
Type of Use	reuse in a thesis/dissertation

Permission for Figure 20:

ELSEVIER LICENSE
TERMS AND CONDITIONS

Apr 30, 2021

This Agreement between University of Waterloo -- Ali Keshavarzkermani ("You") and Elsevier ("Elsevier") consists of your license details and the terms and conditions provided by Elsevier and Copyright Clearance Center.

License Number	5058931373150
License date	Apr 30, 2021
Licensed Content Publisher	Elsevier
Licensed Content Publication	Materials Characterization
Licensed Content Title	Nickel-based superalloy microstructure obtained by pulsed laser powder bed fusion
Licensed Content Author	Y. Tian,J.A. Muñiz-Lerma,M. Brochu
Licensed Content Date	Sep 1, 2017
Licensed Content Volume	131
Licensed Content Issue	n/a
Licensed Content Pages	10
Start Page	306
End Page	315
Type of Use	reuse in a thesis/dissertation

Permission for Figure 21:

ELSEVIER LICENSE
TERMS AND CONDITIONS

Apr 30, 2021

This Agreement between University of Waterloo -- Ali Keshavarzkermani ("You") and Elsevier ("Elsevier") consists of your license details and the terms and conditions provided by Elsevier and Copyright Clearance Center.

License Number	5058940143740
License date	Apr 30, 2021
Licensed Content Publisher	Elsevier
Licensed Content Publication	Materials Science and Engineering: A
Licensed Content Title	Microstructure and mechanical properties of Inconel 718 produced by selective laser melting: Sample orientation dependence and effects of post heat treatments
Licensed Content Author	Dunyong Deng,Ru Lin Peng,Håkan Brodin,Johan Moverare
Licensed Content Date	Jan 24, 2018
Licensed Content Volume	713
Licensed Content Issue	n/a
Licensed Content Pages	13
Start Page	294
End Page	306
Type of Use	reuse in a thesis/dissertation

Permission for Figure 22:

ELSEVIER LICENSE
TERMS AND CONDITIONS

Apr 30, 2021

This Agreement between University of Waterloo -- Ali Keshavarzkermani ("You") and Elsevier ("Elsevier") consists of your license details and the terms and conditions provided by Elsevier and Copyright Clearance Center.

License Number	5058930955658
License date	Apr 30, 2021
Licensed Content Publisher	Elsevier
Licensed Content Publication	Materials Characterization
Licensed Content Title	Microstructure of selective laser melted CM247LC nickel-based superalloy and its evolution through heat treatment
Licensed Content Author	V.D. Divya,R. Muñoz-Moreno,O.M.D.M. Messé,J.S. Barnard,S. Baker,T. Illston,H.J. Stone
Licensed Content Date	Apr 1, 2016
Licensed Content Volume	114
Licensed Content Issue	n/a
Licensed Content Pages	13
Start Page	62
End Page	74
Type of Use	reuse in a thesis/dissertation

Permission for Figure 23:

ELSEVIER LICENSE
TERMS AND CONDITIONS

Apr 30, 2021

This Agreement between University of Waterloo -- Ali Keshavarzkermani ("You") and Elsevier ("Elsevier") consists of your license details and the terms and conditions provided by Elsevier and Copyright Clearance Center.

License Number	5058930572177
License date	Apr 30, 2021
Licensed Content Publisher	Elsevier
Licensed Content Publication	Materials Science and Engineering: A
Licensed Content Title	Influence of post heat treatments on anisotropy of mechanical behaviour and microstructure of Hastelloy-X parts produced by selective laser melting
Licensed Content Author	Dacian Tomus,Yang Tian,Paul A. Rometsch,Martin Heilmaier,Xinhua Wu
Licensed Content Date	Jun 14, 2016
Licensed Content Volume	667
Licensed Content Issue	n/a
Licensed Content Pages	12
Start Page	42
End Page	53
Type of Use	reuse in a thesis/dissertation

Permission for Figure 24:

ELSEVIER LICENSE
TERMS AND CONDITIONS

Apr 30, 2021

This Agreement between University of Waterloo -- Ali Keshavarzkermani ("You") and Elsevier ("Elsevier") consists of your license details and the terms and conditions provided by Elsevier and Copyright Clearance Center.

License Number	5058930955658
License date	Apr 30, 2021
Licensed Content Publisher	Elsevier
Licensed Content Publication	Materials Characterization
Licensed Content Title	Microstructure of selective laser melted CM247LC nickel-based superalloy and its evolution through heat treatment
Licensed Content Author	V.D. Divya,R. Muñoz-Moreno,O.M.D.M. Messé,J.S. Barnard,S. Baker,T. Illston,H.J. Stone
Licensed Content Date	Apr 1, 2016
Licensed Content Volume	114
Licensed Content Issue	n/a
Licensed Content Pages	13
Start Page	62
End Page	74
Type of Use	reuse in a thesis/dissertation

Permission for Figure 25:

ELSEVIER LICENSE
TERMS AND CONDITIONS

Apr 30, 2021

This Agreement between University of Waterloo -- Ali Keshavarzkermani ("You") and Elsevier ("Elsevier") consists of your license details and the terms and conditions provided by Elsevier and Copyright Clearance Center.

License Number	5058930572177
License date	Apr 30, 2021
Licensed Content Publisher	Elsevier
Licensed Content Publication	Materials Science and Engineering: A
Licensed Content Title	Influence of post heat treatments on anisotropy of mechanical behaviour and microstructure of Hastelloy-X parts produced by selective laser melting
Licensed Content Author	Dacian Tomus,Yang Tian,Paul A. Rometsch,Martin Heilmaier,Xinhua Wu
Licensed Content Date	Jun 14, 2016
Licensed Content Volume	667
Licensed Content Issue	n/a
Licensed Content Pages	12
Start Page	42
End Page	53
Type of Use	reuse in a thesis/dissertation

ELSEVIER LICENSE
TERMS AND CONDITIONS

Apr 30, 2021

This Agreement between University of Waterloo -- Ali Keshavarzkermani ("You") and Elsevier ("Elsevier") consists of your license details and the terms and conditions provided by Elsevier and Copyright Clearance Center.

License Number	5058940143740
License date	Apr 30, 2021
Licensed Content Publisher	Elsevier
Licensed Content Publication	Materials Science and Engineering: A
Licensed Content Title	Microstructure and mechanical properties of Inconel 718 produced by selective laser melting: Sample orientation dependence and effects of post heat treatments
Licensed Content Author	Dunyong Deng,Ru Lin Peng,Håkan Brodin,Johan Moverare
Licensed Content Date	Jan 24, 2018
Licensed Content Volume	713
Licensed Content Issue	n/a
Licensed Content Pages	13
Start Page	294
End Page	306
Type of Use	reuse in a thesis/dissertation

Permission for Figure 26 and 27:

ELSEVIER LICENSE
TERMS AND CONDITIONS

Apr 30, 2021

This Agreement between University of Waterloo -- Ali Keshavarzkermani ("You") and Elsevier ("Elsevier") consists of your license details and the terms and conditions provided by Elsevier and Copyright Clearance Center.

License Number	5058940433884
License date	Apr 30, 2021
Licensed Content Publisher	Elsevier
Licensed Content Publication	Materials Science and Engineering: A
Licensed Content Title	Effect of standard heat treatment on the microstructure and mechanical properties of hot isostatically pressed superalloy inconel 718
Licensed Content Author	G.Appa Rao,Mahendra Kumar,M. Srinivas,D.S. Sarma
Licensed Content Date	Aug 25, 2003
Licensed Content Volume	355
Licensed Content Issue	1-2
Licensed Content Pages	12
Start Page	114
End Page	125
Type of Use	reuse in a thesis/dissertation

References

[1] H. Fayazfar, M. Salarian, A. Rogalsky, D. Sarker, P. Russo, V. Paserin, E. Toyserkani, A critical review of powder-based additive manufacturing of ferrous alloys: Process parameters, microstructure and mechanical properties, Mater. Des. 144 (2018) 98–128. doi:10.1016/j.matdes.2018.02.018.

[2] T. Trosch, J. Strößner, R. Völkl, U. Glatzel, Microstructure and mechanical properties of selective laser melted Inconel 718 compared to forging and casting, Mater. Lett. 164 (2016) 428–431. doi:10.1016/j.matlet.2015.10.136.

[3] V.A. Popovich, E. V. Borisov, A.A. Popovich, V.S. Sufiiarov, D. V. Masaylo, L. Alzina, Functionally graded Inconel 718 processed by additive manufacturing: Crystallographic texture, anisotropy of microstructure and mechanical properties, Mater. Des. 114 (2017) 441–449. doi:10.1016/j.matdes.2016.10.075.

[4] T. Ishimoto, K. Hagihara, K. Hisamoto, S.H. Sun, T. Nakano, Crystallographic texture control of beta-type Ti–15Mo–5Zr–3Al alloy by selective laser melting for the development of novel implants with a biocompatible low Young's modulus, Scr. Mater. 132 (2017) 34–38. doi:10.1016/j.scriptamat.2016.12.038.

[5] B. Song, S. Dong, S. Deng, H. Liao, C. Coddet, Microstructure and tensile properties of iron parts fabricated by selective laser melting, Opt. Laser Technol. 56 (2014) 451–460. doi:10.1016/j.optlastec.2013.09.017.

[6] W.E. King, H.D. Barth, V.M. Castillo, G.F. Gallegos, J.W. Gibbs, D.E. Hahn, C. Kamath, A.M. Rubenchik, Observation of keyhole-mode laser melting in laser powder-bed fusion additive manufacturing, J. Mater. Process. Technol. 214 (2014) 2915–2925. doi:10.1016/j.jmatprotec.2014.06.005.

[7] W.M. Tucho, V.H. Lysne, H. Austbø, A. Sjolyst-Kverneland, V. Hansen, Investigation of effects of process parameters on microstructure and hardness of SLM manufactured SS316L, J. Alloys Compd. 740 (2018) 910–925. doi:10.1016/j.jallcom.2018.01.098.

[8] C. Zhao, K. Fezzaa, R.W. Cunningham, H. Wen, F. De Carlo, L. Chen, A.D. Rollett, T. Sun, Real-time monitoring of laser powder bed fusion process using high-speed X-ray imaging and diffraction, Sci. Rep. 7 (2017) 1–11. doi:10.1038/s41598-017-03761-2.

[9] L.E. Murr, E. Martinez, K.N. Amato, S.M. Gaytan, J. Hernandez, D.A. Ramirez, P.W. Shindo, F. Medina, R.B. Wicker, Fabrication of metal and alloy components by additive manufacturing: Examples of 3D materials science, J. Mater. Res. Technol. 1 (2012) 42–54. doi:10.1016/S2238-7854(12)70009-1.

[10] V. Bhavar, P. Kattire, V. Patil, S. Khot, K. Gujar, R. Singh, A Review on Powder Bed Fusion Technology of Metal Additive Manufacturing, Addit. Manuf. Soc. India. (2014).

[11] R.C. Reed, The superalloys fundamentals and applications, 2006.

[12] B. Geddes, H. Leon, X. Huang, Superalloys: Alloying and Performance, 2010. doi:10.1016/B978-0-7020-2797-0.00001-1.

[13] M.J. Donachie, S.J. Donachie, SUPERALLOYS Second Edition, 2002.

[14] L.E. Murr, A Metallographic Review of 3D Printing/Additive Manufacturing of Metal and Alloy Products and Components, Metallogr. Microstruct. Anal. 6 (2018). doi:10.1007/s13632-018-0433-6.

[15] A. Keshavarzkermani, M. Sadowski, L. Ladani, Direct metal laser melting of Inconel 718: Process impact on grain formation and orientation, J. Alloys Compd. 736 (2018) 297–305. doi:10.1016/j.jallcom.2017.11.130.

[16] W.J. Sames, K.A. Unocic, G.W. Helmreich, M.M. Kirka, F. Medina, R.R. Dehoff, S.S. Babu, Feasibility of in situ controlled heat treatment (ISHT) of Inconel 718 during electron beam melting additive manufacturing, Addit. Manuf. 13 (2017) 156–165. doi:10.1016/j.addma.2016.09.001.

[17] V. Mo, THE MICROSTRUCTURE OF RAPIDLY SOLIDIFIED A1-Fe A L L O Y S S U B J E C T E D T O L A S E R S U R F A C E TREATMENT, 38 (1990) 2587–2599.

[18] K. Darvish, Z.W. Chen, M.A.L. Phan, T. Pasang, Selective laser melting of Co-29Cr-6Mo alloy with laser power 180–360 W: Cellular growth, intercellular spacing and the related thermal condition, Mater. Charact. 135 (2018) 183–191. doi:10.1016/j.matchar.2017.11.042.

[19] N.J. Harrison, K. Mumtaz, ScienceDirect Reduction of micro-cracking in nickel superalloys processed by Selective Laser Melting : A fundamental alloy design approach, 94 (2015) 59–68. doi:10.1016/j.actamat.2015.04.035.

[20] A. Basak, S. Das, Epitaxy and Microstructure Evolution in Metal Additive Manufacturing, (n.d.). doi:10.1146/annurev-matsci-070115-031728.

[21] D. Tomus, Y. Tian, P.A. Rometsch, M. Heilmaier, X. Wu, Influence of post heat treatments on anisotropy of mechanical behaviour and microstructure of Hastelloy-X parts produced by selective laser melting, Mater. Sci. Eng. A. 667 (2016) 42–53. doi:10.1016/j.msea.2016.04.086.

[22] X. Wang, L.N. Carter, B. Pang, M.M. Attallah, M.H. Loretto, Acta Materialia Microstructure and yield strength of SLM-fabricated CM247LC, Acta Mater. 128 (2017) 87–95. doi:10.1016/j.actamat.2017.02.007.

[23] V.D. Divya, R. Muñoz-moreno, O.M.D.M. Messé, J.S. Barnard, S. Baker, T. Illston, H.J. Stone, Materials Characterization Microstructure of selective laser melted CM247LC nickel-based superalloy and its evolution through heat treatment, Mater. Charact. 114 (2016) 62–74. doi:10.1016/j.matchar.2016.02.004.

[24] K. Darvish, Z.W. Chen, M.A.L. Phan, T. Pasang, Materials Characterization Selective laser melting of Co-29Cr-6Mo alloy with laser power 180 – 360 W : Cellular growth , intercellular spacing and the related thermal condition, Mater. Charact. 135 (2018) 183–191. doi:10.1016/j.matchar.2017.11.042.

[25] Y. Tian, M. Brochu, Materials Characterization Nickel-based superalloy microstructure obtained by pulsed laser powder bed fusion, Mater. Charact. 131 (2017) 306–315. doi:10.1016/j.matchar.2017.07.024.

[26] D. Deng, R. Lin, H. Brodin, J. Moverare, Materials Science & Engineering A Microstructure and mechanical properties of Inconel 718 produced by selective laser melting : Sample orientation dependence and e ff ects of post heat treatments, Mater. Sci. Eng. A. 713 (2018) 294–306. doi:10.1016/j.msea.2017.12.043.

[27] D. Zhang, W. Niu, X. Cao, Z. Liu, Materials Science & Engineering A Effect of standard heat treatment on the microstructure and mechanical properties of selective laser melting manufactured Inconel, Mater. Sci. Eng. A. 644 (2015) 32–40. doi:10.1016/j.msea.2015.06.021.

[28] H. Fayazfar, M. Salarian, A. Rogalsky, D. Sarker, P. Russo, V. Paserin, E. Toyserkani, A critical review of powder-based additive manufacturing of ferrous alloys: Process parameters, microstructure and mechanical properties, Mater. Des. 144 (2018) 98–128. doi:10.1016/j.matdes.2018.02.018.

[29] M. Sadowski, L. Ladani, W. Brindley, J. Romano, Optimizing quality of additively manufactured Inconel 718 using powder bed laser melting process, Addit. Manuf. 11 (2016) 60–70. doi:10.1016/j.addma.2016.03.006.

[30] A. Aversa, M. Moshiri, E. Librera, M. Hadi, G. Marchese, D. Manfredi, M. Lorusso, F. Calignano, S. Biamino, M. Lombardi, M. Pavese, Single scan track analyses on aluminium based powders, J. Mater. Process. Technol. 255 (2018) 17–25. doi:10.1016/j.jmatprotec.2017.11.055.

[31] J. Ciurana, L. Hernandez, J. Delgado, Energy density analysis on single tracks formed by selective laser melting with CoCrMo powder material, Int. J. Adv. Manuf. Technol. 68 (2013) 1103–1110. doi:10.1007/s00170-013-4902-4.

[32] T. DebRoy, H.L. Wei, J.S. Zuback, T. Mukherjee, J.W. Elmer, J.O. Milewski, A.M. Beese, A. Wilson-Heid, A. De, W. Zhang, Additive manufacturing of metallic components – Process, structure and properties, Prog. Mater. Sci. 92 (2018) 112–224. doi:10.1016/j.pmatsci.2017.10.001.

[33] D. Gu, Y. Shen, Processing conditions and microstructural features of porous 316L stainless steel components by DMLS, Appl. Surf. Sci. 255 (2008) 1880–1887. doi:10.1016/j.apsusc.2008.06.118.

[34] H. Gong, K. Rafi, H. Gu, T. Starr, B. Stucker, Analysis of defect generation in Ti-6Al-4V parts made using powder bed fusion additive manufacturing processes, Addit. Manuf. 1 (2014) 87–98. doi:10.1016/j.addma.2014.08.002.

[35] I. Yadroitsev, A. Gusarov, I. Yadroitsava, I. Smurov, Single track formation in selective laser melting of metal powders, J. Mater. Process. Technol. 210 (2010) 1624–1631. doi:10.1016/j.jmatprotec.2010.05.010.

[36] K. Kempen, L. Thijs, J. Van Humbeeck, J.-P. Kruth, Processing AlSi10Mg by selective laser melting: parameter optimisation and material characterisation, Mater. Sci. Technol. 31 (2015) 917–923. doi:10.1179/1743284714Y.0000000702.

[37] I. Yadroitsev, P. Krakhmalev, I. Yadroitsava, S. Johansson, I. Smurov, Energy input effect on morphology and microstructure of selective laser melting single track from metallic powder, J. Mater. Process. Technol. 213 (2013) 606–613. doi:10.1016/j.jmatprotec.2012.11.014.

[38] J.J.S. Dilip, A. Anam, D. Pal, B. Stucker, A short study on the fabrication of single track deposits in SLM and characterization, Solid Free. Fabr. Symp. (2016) 1644–1659.

[39] X. Wang, K. Chou, Electron Backscatter Diffraction Analysis of Inconel 718 Parts Fabricated by Selective Laser Melting Additive Manufacturing, Jom. 69 (2017) 402–408. doi:10.1007/s11837-016-2198-1.

[40] Q. Jia, D. Gu, Selective laser melting additive manufacturing of Inconel 718 superalloy parts: densification, microstructure and properties, J. Alloys Compd. 585 (2014) 713–721.

doi:10.1016/j.jallcom.2013.09.171.

[41] X. Gong, X. Wang, J.V. Cole, Z. Jones, K. Cooper, K. Chou, Characterization of Microstructure and Mechanical Property of Inconel 718 from Selective Laser Melting, Proc. ASME 2015 Int. Manuf. Sci. Eng. Conf. MSEC2015. (2015) MSEC2015-9317. doi:10.1115/MSEC20159317.

[42] EOS GmbH - Electro Optical Systems, Material data sheet EOS NickelAlloy HX Material data sheet Technical data, 49 (2015) 1–5.

[43] U. Scipioni Bertoli, A.J. Wolfer, M.J. Matthews, J.P.R. Delplanque, J.M. Schoenung, On the limitations of Volumetric Energy Density as a design parameter for Selective Laser Melting, Mater. Des. 113 (2017) 331–340. doi:10.1016/j.matdes.2016.10.037.

[44] J. Ye, A.M. Rubenchik, M.F. Crumb, G. Guss, M.J. Matthews, Laser Absorption and Scaling Behavior in Powder Bed Fusion Additive Manufacturing of Metals, Conf. Lasers Electro-Optics. 625 (2018) JW2A.117. doi:10.1364/CLEO_AT.2018.JW2A.117.

[45] Q. Han, R. Mertens, M.L. Montero-Sistiaga, S. Yang, R. Setchi, K. Vanmeensel, B. Van Hooreweder, S.L. Evans, H. Fan, Laser powder bed fusion of Hastelloy X: Effects of hot isostatic pressing and the hot cracking mechanism, Mater. Sci. Eng. A. 732 (2018) 228–239. doi:10.1016/j.msea.2018.07.008.

[46] D. Tomus, Y. Tian, P.A. Rometsch, M. Heilmaier, X. Wu, Influence of post heat treatments on anisotropy of mechanical behaviour and microstructure of Hastelloy-X parts produced by selective laser melting, Mater. Sci. Eng. A. 667 (2016) 42–53. doi:10.1016/j.msea.2016.04.086.

[47] Y. Tian, D. Tomus, P. Rometsch, X. Wu, Influences of processing parameters on surface roughness of Hastelloy X produced by selective laser melting, Addit. Manuf. 13 (2017) 103–112. doi:10.1016/j.addma.2016.10.010.

[48] D. Tomus, P.A. Rometsch, M. Heilmaier, X. Wu, Effect of minor alloying elements on crack-formation characteristics of Hastelloy-X manufactured by selective laser melting, Addit. Manuf. 16 (2017) 65–72. doi:10.1016/j.addma.2017.05.006.

[49] G.F. Vander Voort, G.M. Lucas, E.P. Manilova, Metallography and Microstructures of Heat-Resistant Alloys, ASM Handb. Metallogr. Microstruct. 9 (2004) 820–859. doi:10.1361/asmhba0003737.

[50] R. Li, J. Liu, Y. Shi, L. Wang, W. Jiang, Balling behavior of stainless steel and nickel powder during selective laser melting process, Int. J. Adv. Manuf. Technol. 59 (2012) 1025–1035. doi:10.1007/s00170-011-3566-1.

[51] Y. Mahmoodkhani, U. Ali, S. Imani Shahabad, A. Rani Kasinathan, R. Esmaeilizadeh, A. Keshavarzkermani, E. Marzbanrad, E. Toyserkani, On the measurement of effective powder layer thickness in laser powder-bed fusion additive manufacturing of metals, Prog. Addit. Manuf. Online, Available Https//Doi.Org/10.1007/S40964-018-0064-0. 0 (2018) 0. doi:10.1007/s40964-018-0064-0.

[52] P. Bidare, R.R.J. Maier, R.J. Beck, J.D. Shephard, A.J. Moore, An open-architecture metal powder bed fusion system for in-situ process measurements, Addit. Manuf. 16 (2017) 177–185. doi:10.1016/j.addma.2017.06.007.

[53] P. Bidare, I. Bitharas, R.M. Ward, M.M. Attallah, A.J. Moore, Fluid and particle dynamics in laser

powder bed fusion, Acta Mater. 142 (2018) 107–120. doi:10.1016/j.actamat.2017.09.051.

[54] R. Esmaeilizadeh, U. Ali, A. Keshavarzkermani, Y. Mahmoodkhani, E. Marzbanrad, E. Toyserkani, On the effect of spatter particles distribution on the quality of Hastelloy X parts made by laser powder-bed fusion additive manufacturing, J. Manuf. Process. 37 (2019) 11–20. doi:10.1016/j.jmapro.2018.11.012.

[55] L. Ladani, J. Romano, W. Brindley, S. Burlatsky, Effective liquid conductivity for improved simulation of thermal transport in laser beam melting powder bed technology, Addit. Manuf. 14 (2017) 13–23. doi:10.1016/j.addma.2016.12.004.

[56] S.A. Khairallah, A.T. Anderson, A. Rubenchik, W.E. King, Laser powder-bed fusion additive manufacturing: Physics of complex melt flow and formation mechanisms of pores, spatter, and denudation zones, Acta Mater. 108 (2016) 36–45. doi:10.1016/j.actamat.2016.02.014.

[57] S. Ly, A.M. Rubenchik, S.A. Khairallah, G. Guss, M.J. Matthews, Metal vapor micro-jet controls material redistribution in laser powder bed fusion additive manufacturing, Sci. Rep. 7 (2017) 1–12. doi:10.1038/s41598-017-04237-z.

[58] U. Scipioni Bertoli, G. Guss, S. Wu, M.J. Matthews, J.M. Schoenung, In-situ characterization of laser-powder interaction and cooling rates through high-speed imaging of powder bed fusion additive manufacturing, Mater. Des. 135 (2017) 385–396. doi:10.1016/j.matdes.2017.09.044.

[59] S. Kou, Welding Metallurgy, 2002. doi:10.1002/0471434027.

[60] V.D. Divya, R. Muñoz-Moreno, O.M.D.M. Messé, J.S. Barnard, S. Baker, T. Illston, H.J. Stone, Microstructure of selective laser melted CM247LC nickel-based superalloy and its evolution through heat treatment, Mater. Charact. 114 (2016) 62–74. doi:10.1016/j.matchar.2016.02.004.

[61] X. Wang, L.N. Carter, B. Pang, M.M. Attallah, M.H. Loretto, Microstructure and yield strength of SLM-fabricated CM247LC Ni-Superalloy, Acta Mater. 128 (2017) 87–95. doi:10.1016/j.actamat.2017.02.007.

[62] N.J. Harrison, I. Todd, K. Mumtaz, Reduction of micro-cracking in nickel superalloys processed by Selective Laser Melting: A fundamental alloy design approach, Acta Mater. 94 (2015) 59–68. doi:10.1016/j.actamat.2015.04.035.

[63] C. Yan, L. Hao, A. Hussein, P. Young, J. Huang, W. Zhu, Microstructure and mechanical properties of aluminium alloy cellular lattice structures manufactured by direct metal laser sintering, Mater. Sci. Eng. A. 628 (2015) 238–246. doi:10.1016/j.msea.2015.01.063.

[64] J.S. Zuback, T. DebRoy, J.S. Zuback, T. DebRoy, The Hardness of Additively Manufactured Alloys, Materials (Basel). 11 (2018) 2070. doi:10.3390/ma11112070.

[65] W. Kurz, R. Trivedi, Rapid solidification processing and microstructure formation, Mater. Sci. Eng. A. 179–80 (1994) 46–51. doi:10.1016/0921-5093(94)90162-7.

[66] G.P. Dinda, A.K. Dasgupta, J. Mazumder, Evolution of microstructure in laser deposited Al-11.28%Si alloy, Surf. Coatings Technol. 206 (2012) 2152–2160. doi:10.1016/j.surfcoat.2011.09.051.

[67] M. Tang, P.C. Pistorius, S. Narra, J.L. Beuth, Rapid Solidification: Selective Laser Melting of AlSi10Mg, Jom. 68 (2016) 960–966. doi:10.1007/s11837-015-1763-3.

[68] A.S. Taha, F.H. Hammad, Application of the {Hall-Petch} Relation to Microhardness Measurements on Al, Cu, {Al-MD} 105, and {Al-Cu} Alloys, Phys. Status Solidi. 119 (1990) 455–462.

[69] M. Munawar, high-purity copper and aluminium, 82 (2002) 2071–2080.

[70] M.H. Avazkonandeh-Gharavol, M. Haddad-Sabzevar, H. Fredriksson, Effect of partition coefficient on microsegregation during solidification of aluminium alloys, Int. J. Miner. Metall. Mater. 21 (2014) 980–989. doi:10.1007/s12613-014-0999-1.

[71] Q. Zhang, J. Chen, X. Lin, H. Tan, W.D. Huang, Grain morphology control and texture characterization of laser solid formed Ti6Al2Sn2Zr3Mo1.5Cr2Nb titanium alloy, J. Mater. Process. Technol. 238 (2016) 202–211. doi:10.1016/j.jmatprotec.2016.07.011.

[72] D. Montiel, L. Liu, L. Xiao, Y. Zhou, N. Provatas, Microstructure analysis of AZ31 magnesium alloy welds using phase-field models, Acta Mater. 60 (2012) 5925–5932. doi:10.1016/j.actamat.2012.07.035.

[73] M.J. Matthews, G. Guss, S.A. Khairallah, A.M. Rubenchik, P.J. Depond, W.E. King, Denudation of metal powder layers in laser powder-bed fusion processes, Addit. Manuf. Handb. Prod. Dev. Def. Ind. 114 (2017) 677–693. doi:10.1201/9781315119106.

[74] R. Esmaeilizadeh, A. Keshavarzkermani, U. Ali, B. Behravesh, A. Bonakdar, H. Jahed, E. Toyserkani, On the effect of laser powder-bed fusion process parameters on quasi-static and fatigue behaviour of Hastelloy X : A microstructure / defect interaction study, Addit. Manuf. 38 (2021) 101805. doi:10.1016/j.addma.2020.101805.

[75] R. Acharya, J.A. Sharon, A. Staroselsky, Prediction of microstructure in laser powder bed fusion process, Acta Mater. 124 (2017) 360–371. doi:10.1016/j.actamat.2016.11.018.

[76] J.H.K. Tan, S.L. Sing, W.Y. Yeong, Microstructure modelling for metallic additive manufacturing: a review, Virtual Phys. Prototyp. 15 (2020) 87–105. doi:10.1080/17452759.2019.1677345.

[77] K.L. Johnson, T.M. Rodgers, O.D. Underwood, J.D. Madison, K.R. Ford, S.R. Whetten, D.J. Dagel, J.E. Bishop, Simulation and experimental comparison of the thermo-mechanical history and 3D microstructure evolution of 304L stainless steel tubes manufactured using LENS, Comput. Mech. 61 (2018) 559–574. doi:10.1007/s00466-017-1516-y.

[78] O. Zinovieva, A. Zinoviev, V. Ploshikhin, Three-dimensional modeling of the microstructure evolution during metal additive manufacturing, Comput. Mater. Sci. 141 (2018) 207–220. doi:10.1016/j.commatsci.2017.09.018.

[79] J. Akram, P. Chalavadi, D. Pal, B. Stucker, Understanding grain evolution in additive manufacturing through modeling, Addit. Manuf. 21 (2018) 255–268. doi:10.1016/j.addma.2018.03.021.

[80] A. Pineau, G. Guillemot, D. Tourret, A. Karma, C.A. Gandin, Growth competition between columnar dendritic grains – Cellular automaton versus phase field modeling, Acta Mater. 155 (2018) 286–301. doi:10.1016/j.actamat.2018.05.032.

[81] S.I. Shahabad, Z. Zhang, A. Keshavarzkermani, U. Ali, Y. Mahmoodkhani, R. Esmaeilizadeh, A. Bonakdar, E. Toyserkani, Heat source model calibration for thermal analysis of laser powder-bed fusion, Int. J. Adv. Manuf. Technol. 106 (2020) 3367–3379. doi:10.1007/s00170-019-04908-3.

[82] Z. Zhang, Y. Huang, A. Rani Kasinathan, S. Imani Shahabad, U. Ali, Y. Mahmoodkhani, E. Toyserkani, 3-Dimensional heat transfer modeling for laser powder-bed fusion additive manufacturing with volumetric heat sources based on varied thermal conductivity and absorptivity, Opt. Laser Technol. 109 (2019) 297–312. doi:10.1016/j.optlastec.2018.08.012.

[83] C.S. Wu, H.G. Wang, Y.M. Zhang, A new heat source model for keyhole plasma arc welding in FEM analysis of the temperature profile, Weld. J. 85 (2006) 284.

[84] P. Martinson, S. Daneshpour, M. Koçak, S. Riekehr, P. Staron, Residual stress analysis of laser spot welding of steel sheets, Mater. Des. 30 (2009) 3351–3359. doi:10.1016/j.matdes.2009.03.041.

[85] R. Kobayashi, Modeling and numerical simulations of dendritic crystal growth, Phys. D Nonlinear Phenom. 63 (1993) 410–423. doi:10.1016/0167-2789(93)90120-P.

[86] M. Division, Metallurgy Division, Materials Science and Engineering Laboratory, NIST, Gaithersburg, MD 20899, U.S.A. (Received 22 April 1994), 43 (1995). doi:10.1016/0956-7151(94)00285-P.

[87] W.J. Boettinger, A.A. Wheeler, B.T. Murray, G.B. McFadden, Prediction of solute trapping at high solidification rates using a diffuse interface phase-field theory of alloy solidification, Mater. Sci. Eng. A. 178 (1994) 217–223. doi:10.1016/0921-5093(94)90546-0.

[88] R. Esmaeilizadeh, A. Keshavarzkermani, U. Ali, Y. Mahmoodkhani, B. Behravesh, H. Jahed, A. Bonakdar, E. Toyserkani, Customizing mechanical properties of additively manufactured Hastelloy X parts by adjusting laser scanning speed, J. Alloys Compd. 812 (2020). doi:10.1016/j.jallcom.2019.152097.

[89] A. Keshavarzkermani, R. Esmaeilizadeh, U. Ali, P.D. Enrique, Y. Mahmoodkhani, N.Y. Zhou, A. Bonakdar, E. Toyserkani, Controlling mechanical properties of additively manufactured hastelloy X by altering solidification pattern during laser powder-bed fusion, Mater. Sci. Eng. A. 762 (2019). doi:10.1016/j.msea.2019.138081.

[90] A. Keshavarzkermani, E. Marzbanrad, R. Esmaeilizadeh, Y. Mahmoodkhani, U. Ali, P.D. Enrique, N.Y. Zhou, A. Bonakdar, E. Toyserkani, An investigation into the e ff ect of process parameters on melt pool geometry , cell spacing , and grain re fi nement during laser powder bed fusion, Opt. Laser Technol. 116 (2019) 83–91. doi:10.1016/j.optlastec.2019.03.012.

[91] M. Rappaz, C.A. Gandin, Probabilistic modelling of microstructure formation in solidification processes, Acta Metall. Mater. 41 (1993) 345–360. doi:10.1016/0956-7151(93)90065-Z.

[92] X. Li, W. Tan, Numerical investigation of effects of nucleation mechanisms on grain structure in metal additive manufacturing, Comput. Mater. Sci. 153 (2018) 159–169. doi:10.1016/j.commatsci.2018.06.019.

[93] E. Chlebus, K. Gruber, B. Kuźnicka, J. Kurzac, T. Kurzynowski, Effect of heat treatment on microstructure and mechanical properties of Inconel 718 processed by selective laser melting, Mater. Sci. Eng. A. (2015). doi:10.1016/j.msea.2015.05.035.

[94] Q. Han, R. Mertens, M.L. Montero-Sistiaga, S. Yang, R. Setchi, K. Vanmeensel, B. Van Hooreweder, S.L. Evans, H. Fan, Laser powder bed fusion of Hastelloy X: Effects of hot isostatic pressing and the hot cracking mechanism, Mater. Sci. Eng. A. 732 (2018) 228–239. doi:10.1016/j.msea.2018.07.008.

[95] A. Keshavarzkermani, E. Marzbanrad, R. Esmaeilizadeh, Y. Mahmoodkhani, U. Ali, P.D. Enrique, N.Y. Zhou, A. Bonakdar, E. Toyserkani, An investigation into the effect of process parameters on melt pool geometry, cell spacing, and grain refinement during laser powder bed fusion, Opt. Laser Technol. 116 (2019) 83–91. doi:10.1016/j.optlastec.2019.03.012.

[96] D. Deng, R.L. Peng, H. Brodin, J. Moverare, Microstructure and mechanical properties of Inconel 718 produced by selective laser melting: Sample orientation dependence and effects of post heat treatments, Mater. Sci. Eng. A. 713 (2018) 294–306. doi:10.1016/j.msea.2017.12.043.

[97] N.T. Aboulkhair, N.M. Everitt, I. Ashcroft, C. Tuck, Reducing porosity in AlSi10Mg parts processed by selective laser melting, Addit. Manuf. 1 (2014) 77–86. doi:10.1016/j.addma.2014.08.001.

[98] L.N. Carter, C. Martin, P.J. Withers, M.M. Attallah, The influence of the laser scan strategy on grain structure and cracking behaviour in SLM powder-bed fabricated nickel superalloy, J. Alloys Compd. 615 (2014) 338–347. doi:10.1016/j.jallcom.2014.06.172.

[99] V.A. Popovich, E. V. Borisov, A.A. Popovich, V.S. Sufiiarov, D. V. Masaylo, L. Alzina, Impact of heat treatment on mechanical behaviour of Inconel 718 processed with tailored microstructure by selective laser melting, Mater. Des. 131 (2017) 12–22. doi:10.1016/j.matdes.2017.05.065.

[100] D. Herzog, V. Seyda, E. Wycisk, C. Emmelmann, Additive manufacturing of metals, Acta Mater. 117 (2016) 371–392. doi:10.1016/j.actamat.2016.07.019.

[101] N. Shamsaei, A. Yadollahi, L. Bian, S.M. Thompson, An overview of Direct Laser Deposition for additive manufacturing; Part II: Mechanical behavior, process parameter optimization and control, Addit. Manuf. 8 (2015) 12–35. doi:10.1016/j.addma.2015.07.002.

[102] W.E. Frazier, Metal additive manufacturing: A review, J. Mater. Eng. Perform. 23 (2014) 1917–1928. doi:10.1007/s11665-014-0958-z.

[103] U. Ali, R. Esmaeilizadeh, F. Ahmed, D. Sarker, W. Muhammad, A. Keshavarzkermani, Y. Mahmoodkhani, E. Marzbanrad, E. Toyserkani, Identification and characterization of spatter particles and their effect on surface roughness, density and mechanical response of 17-4 PH stainless steel laser powder-bed fusion parts, Mater. Sci. Eng. A. 756 (2019) 98–107. doi:10.1016/j.msea.2019.04.026.

[104] Y. Lu, S. Wu, Y. Gan, T. Huang, C. Yang, L. Junjie, J. Lin, Study on the microstructure, mechanical property and residual stress of SLM Inconel-718 alloy manufactured by differing island scanning strategy, Opt. Laser Technol. 75 (2015) 197–206. doi:10.1016/j.optlastec.2015.07.009.

[105] J. Saarimäki, M. Lundberg, H. Brodin, J.J. Moverare, Dwell-fatigue crack propagation in additive manufactured Hastelloy X, Mater. Sci. Eng. A. 722 (2018) 30–36. doi:10.1016/j.msea.2018.02.091.

[106] H.L. Wei, J. Mazumder, T. DebRoy, Evolution of solidification texture during additive manufacturing, Sci. Rep. 5 (2015) 1–7. doi:10.1038/srep16446.

[107] J.J. Blecher, T.A. Palmer, T. Debroy, Solidification map of a nickel-base alloy, Metall. Mater. Trans. A Phys. Metall. Mater. Sci. 45 (2014) 2142–2151. doi:10.1007/s11661-013-2149-1.

[108] A. Takaichi, Suyalatu, T. Nakamoto, N. Joko, N. Nomura, Y. Tsutsumi, S. Migita, H. Doi, S. Kurosu, A. Chiba, N. Wakabayashi, Y. Igarashi, T. Hanawa, Microstructures and mechanical properties of Co-29Cr-6Mo alloy fabricated by selective laser melting process for dental applications, J. Mech.

Behav. Biomed. Mater. 21 (2013) 67–76. doi:10.1016/j.jmbbm.2013.01.021.

[109] R. Wauthle, B. Vrancken, B. Beynaerts, K. Jorissen, J. Schrooten, J.P. Kruth, J. Van Humbeeck, Effects of build orientation and heat treatment on the microstructure and mechanical properties of selective laser melted Ti6Al4V lattice structures, Addit. Manuf. 5 (2015) 77–84. doi:10.1016/j.addma.2014.12.008.

[110] T. Etter, K. Kunze, F. Geiger, H. Meidani, Reduction in mechanical anisotropy through high temperature heat treatment of Hastelloy X processed by Selective Laser Melting (SLM), IOP Conf. Ser. Mater. Sci. Eng. 82 (2015). doi:10.1088/1757-899X/82/1/012097.

[111] E. Chlebus, K. Gruber, B. Kuźnicka, J. Kurzac, T. Kurzynowski, Effect of heat treatment on the microstructure and mechanical properties of Inconel 718 processed by selective laser melting, Mater. Sci. Eng. A. 639 (2015) 647–655. doi:10.1016/j.msea.2015.05.035.

[112] C.A. Siqueira, N. Cheung, A. Garcia, Solidification thermal parameters affecting the columnar-to-equiaxed transition, Metall. Mater. Trans. A Phys. Metall. Mater. Sci. 33 (2002) 2107–2118. doi:10.1007/s11661-002-0042-4.

[113] X. Wang, S. Lin, J. Yang, Z. Tang, Z. Nie, Microstructure and mechanical properties of Al-Mg-Mn alloy with erbium, Rare Met. 31 (2012) 237–243. doi:10.1007/s12598-012-0498-3.

[114] T.D. Xia, X. Chen, Q.L. Li, W.J. Zhao, Grain refining efficiency and mechanism of pure nickel, Rare Met. 34 (2015) 662–666. doi:10.1007/s12598-013-0125-y.

[115] Q. Zhang, M. Cao, J. Cai, AlSi9Mg aluminum alloy semi-solid slurry preparation by intermediate frequency electromagnetic oscillation process, J. Mater. Process. Technol. 215 (2015) 42–49. doi:10.1016/j.jmatprotec.2014.08.003.

[116] K.B. Nie, X.J. Wang, K. Wu, L. Xu, M.Y. Zheng, X.S. Hu, Processing, microstructure and mechanical properties of magnesium matrix nanocomposites fabricated by semisolid stirring assisted ultrasonic vibration, J. Alloys Compd. 509 (2011) 8664–8669. doi:10.1016/j.jallcom.2011.06.091.

[117] C. Wang, M. Wang, Z. Liu, Z. Liu, Y. Weng, T. Song, S. Yang, The grain refining action of fine TiB2 particles in the electrolytic low-titanium aluminum with Al-4B addition, Mater. Sci. Eng. A. 427 (2006) 148–153. doi:10.1016/j.msea.2006.04.012.

[118] D. Qiu, M.X. Zhang, J.A. Taylor, H.M. Fu, P.M. Kelly, A novel approach to the mechanism for the grain refining effect of melt superheating of Mg-Al alloys, Acta Mater. 55 (2007) 1863–1871. doi:10.1016/j.actamat.2006.10.047.

[119] H. Zhao, Y. Song, M. Li, S. Guan, Grain refining efficiency and microstructure of Al-Ti-C-RE master alloy, J. Alloys Compd. 508 (2010) 206–211. doi:10.1016/j.jallcom.2010.08.047.

[120] V.B. Biscuola, M.A. Martorano, Mechanical blocking mechanism for the columnar to equiaxed transition, Metall. Mater. Trans. A Phys. Metall. Mater. Sci. 39 (2008) 2885–2895. doi:10.1007/s11661-008-9643-x.

[121] ASTM E8, ASTM E8/E8M standard test methods for tension testing of metallic materials 1, Annu. B. ASTM Stand. 4. (2010) 1–27. doi:10.1520/E0008.

[122] H.J. Bunge, Some applications of the Taylor theory of polycrystal plasticity, Krist. Und Tech. 5 (1970) 145–175. doi:10.1002/crat.19700050112.

[123] L. Thijs, M.L. Montero Sistiaga, R. Wauthle, Q. Xie, J.P. Kruth, J. Van Humbeeck, Strong morphological and crystallographic texture and resulting yield strength anisotropy in selective laser melted tantalum, Acta Mater. 61 (2013) 4657–4668. doi:10.1016/j.actamat.2013.04.036.

[124] O. Andreau, I. Koutiri, P. Peyre, J.-D. Penot, N. Saintier, E. Pessard, T. De Terris, C. Dupuy, T. Baudin, Texture control of 316L parts by modulation of the melt pool morphology in selective laser melting, J. Mater. Process. Technol. 264 (2019) 21–31. doi:10.1016/J.JMATPROTEC.2018.08.049.

[125] A.N. Jinoop, J. Denny, C.P. Paul, J.G. Kumar, K.S. Bindra, Effect of post heat-treatment on the microstructure and mechanical properties of Hastelloy-X structures manufactured by laser based Directed Energy Deposition, J. Alloys Compd. 797 (2019) 399–412.

[126] M.W. Wu, P.H. Lai, The positive effect of hot isostatic pressing on improving the anisotropies of bending and impact properties in selective laser melted Ti-6Al-4V alloy, Mater. Sci. Eng. A. 658 (2016) 429–438. doi:10.1016/j.msea.2016.02.023.

[127] A. Keshavarzkermani, E. Marzbanrad, R. Esmaeilizadeh, Y. Mahmoodkhani, U. Ali, P.D. Enrique, N.Y. Zhou, A. Bonakdar, E. Toyserkani, An investigation into the effect of process parameters on melt pool geometry, cell spacing, and grain refinement during laser powder bed fusion, Opt. Laser Technol. 116 (2019) 83–91. doi:10.1016/j.optlastec.2019.03.012.

[128] S. Rosenthal, S. Platt, R. Hölker-Jäger, S. Gies, S. Kleszczynski, A.E. Tekkaya, G. Witt, Forming properties of additively manufactured monolithic Hastelloy X sheets, Mater. Sci. Eng. A. 753 (2019) 300–316. doi:10.1016/j.msea.2019.03.035.

[129] A. Keshavarzkermani, R. Esmaeilizadeh, U. Ali, P.D. Enrique, Y. Mahmoodkhani, N.Y. Zhou, A. Bonakdar, E. Toyserkani, Materials Science & Engineering A Controlling mechanical properties of additively manufactured hastelloy X by altering solidi fi cation pattern during laser powder-bed fusion, Mater. Sci. Eng. A. 762 (2019) 138081. doi:10.1016/j.msea.2019.138081.

[130] Haynes International, Hastelloy ® X Alloy, Haynes Int. 06002 (1997) 16. http://www.haynes.ch/doc/HASTELLOY_X.pdf.

[131] F.J. Humphreys, M. Hatherly, Recrystallization and related annealing phenomena, Elsevier, 2012.

[132] A.T. Polonsky, W.C. Lenthe, M.P. Echlin, V. Livescu, G.T. Gray, T.M. Pollock, Solidification-driven orientation gradients in additively manufactured stainless steel, Acta Mater. 183 (2020) 249–260. doi:10.1016/j.actamat.2019.10.047.

[133] Z.G. Zhu, Q.B. Nguyen, F.L. Ng, X.H. An, X.Z. Liao, P.K. Liaw, S.M.L. Nai, J. Wei, Hierarchical microstructure and strengthening mechanisms of a CoCrFeNiMn high entropy alloy additively manufactured by selective laser melting, Scr. Mater. 154 (2018) 20–24. doi:10.1016/j.scriptamat.2018.05.015.

[134] S. Pourbabak, M.L. Montero-Sistiaga, D. Schryvers, J. Van Humbeeck, K. Vanmeensel, Microscopic investigation of as built and hot isostatic pressed Hastelloy X processed by Selective Laser Melting, Mater. Charact. 153 (2019) 366–371. doi:10.1016/j.matchar.2019.05.024.

[135] G. Marchese, E. Bassini, A. Aversa, M. Lombardi, D. Ugues, P. Fino, S. Biamino, Microstructural evolution of post-processed Hastelloy X alloy fabricated by laser powder bed fusion, Materials (Basel). 12 (2019). doi:10.3390/ma12030486.

[136] B. Geddes, H. Leon, X. Huang, Superalloys: alloying and performance, Asm International, 2010.

[137] R.D. Doherty, D.A. Hughes, F.J. Humphreys, J.J. Jonas, D. Juul Jensen, M.E. Kassner, W.E. King, T.R. McNelley, H.J. McQueen, A.D. Rollett, Current issues in recrystallization: A review, Mater. Sci. Eng. A. 238 (1997) 219–274. doi:10.1016/S0921-5093(97)00424-3.

[138] U. Ali, D. Odoh, W. Muhammad, A. Brahme, R.K. Mishra, M. Wells, K. Inal, Experimental investigation and through process crystal plasticity-static recrystallization modeling of temperature and strain rate effects during hot compression of AA6063, Mater. Sci. Eng. A. 700 (2017) 374–386. doi:10.1016/j.msea.2017.06.030.

[139] P.A. Beck, P.R. Sperry, Strain induced grain boundary migration in high purity aluminum, J. Appl. Phys. 21 (1950) 150–152. doi:10.1063/1.1699614.

[140] W.B. Hutchinson, Recrystallisation textures in iron resulting from nucleation at grain boundaries, Acta Metall. 37 (1989) 1047–1056. doi:10.1016/0001-6160(89)90101-6.

[141] D.C. Van Aken, Formation of annealing twins, Ind. Heat. 67 (2000) 18.

[142] D. Bufford, Y. Liu, Y. Zhu, Z. Bi, Q.X. Jia, H. Wang, X. Zhang, Formation mechanisms of high-density growth twins in aluminum with high stacking-fault energy, Mater. Res. Lett. 1 (2013) 51–60. doi:10.1080/21663831.2012.761654.

[143] X.S. Xie, G.L. Chen, P.J. McHugh, J.K. Tien, Including stacking fault energy into the resisting stress model for creep of particle strengthened alloys, Scr. Metall. 16 (1982) 483–488. doi:10.1016/0036-9748(82)90254-X.

[144] P. Behjati, S. Asgari, Microstructural characterisation of deformation behaviour of nickel base superalloy IN625, Mater. Sci. Technol. 27 (2011) 1858–1862. doi:10.1179/1743284711Y.0000000056.

[145] E.E.D. S. Asgari, R.D.D. S. R. Kalidindi, “Strain Hardening Regimes and Microstructural Evolution during Large Strain Compression of Low Stacking Fault Energy Fcc Alloys That Form Deformation Twins.” Metallurgical and Materials Transactions A (Physical Metallurgy and Materials Science) Sept. 1997, Metall. Mater. Trans. A. 28 (1997) 1781–1782.

[146] F. Hamdi, S. Asgari, Evaluation of the role of deformation twinning in work hardening behavior of face-centered-cubic polycrystals, Metall. Mater. Trans. A Phys. Metall. Mater. Sci. 39 (2008) 294–303. doi:10.1007/s11661-007-9356-6.

[147] S.I. Hong, C. Laird, Mechanisms of slip mode modification in F.C.C. solid solutions, Acta Metall. Mater. 38 (1990) 1581–1594. doi:10.1016/0956-7151(90)90126-2.

[148] N. Clément, D. Caillard, J.L. Martin, Heterogeneous deformation of concentrated NiCr F.C.C. alloys: Macroscopic and microscopic behaviour, Acta Metall. 32 (1984) 961–975. doi:10.1016/0001-6160(84)90034-8.

[149] G.E. Dieter, D.J. Bacon, Mechanical metallurgy, McGraw-hill New York, 1986.